TIME-LAPSE SEISMIC MONITORING OF SUBSURFACE FLUID FLOW

A Dissertation

by

SUNG H. YUH

Submitted to the Office of Graduate Studies of
Texas A&M University
in partial fulfillment of the requirements for the degree of

DOCTOR OF PHILOSOPHY

May 2003

Major Subject: Geophysics

TIME-LAPSE SEISMIC MONITORING OF SUBSURFACE FLUID FLOW

A Dissertation

by

SUNG H. YUH

Submitted to Texas A&M University
in partial fulfillment of the requirements
for the degree of

DOCTOR OF PHILOSOPHY

Approved as to style and content by:

Richard L. Gibson, Jr. (Chair of Committee)	Joel S. Watkins (Member)
Mark E. Everett (Member)	Akhil Datta-Gupta (Member)
Raytcho Lazarov (Member)	Andrew Hajash, Jr. (Head of Department)

May 2003

Major Subject: Geophysics

ABSTRACT

Time-lapse Seismic Monitoring Of
Subsurface Fluid Flow. (May 2003)
Sung H. Yuh, B.S., Korea University, Korea;
M.S., Texas A&M University
Chair of Advisory Committee: Dr. Richard L. Gibson, Jr.

Time-lapse seismic monitoring repeats 3D seismic imaging over a reservoir to map fluid movements in a reservoir. During hydrocarbon production, the fluid saturation, pressure, and temperature of a reservoir change, thereby altering the acoustic properties of the reservoir. Time-lapse seismic analysis can illuminate these dynamic changes of reservoir properties, and therefore has strong potential for improving reservoir management. However, the response of a reservoir depends on many parameters and can be difficult to understand and predict.

Numerical modeling results integrating streamline fluid flow simulation, rock physics, and ray-Born seismic modeling address some of these problems. Calculations show that the sensitivity of amplitude changes to porosity depends on the type of sediment comprising the reservoir. For consolidated rock, high-porosity models show larger amplitude changes than low porosity models. However, in an unconsolidated formation, there is less consistent correlation between amplitude and porosity. The rapid time-lapse modeling schemes also allow statistical analysis of the uncertainty in seismic response associated with poorly known values of reservoir parameters such as permeability and dry bulk modulus. Results show that for permeability, the maximum uncertainties in time-lapse seismic signals occur at the water front, where saturation is most variable. For the dry bulk-modulus, the uncertainty is greatest near the injection well, where the maximum saturation changes occur.

Time-lapse seismic methods can also be applied to monitor CO_2 sequestration. Simulations show that since the acoustic properties of CO_2 are very different from those of hydrocarbons and water, it is possible to image CO_2 saturation using seismic monitoring. Furthermore, amplitude changes after supercritical fluid CO_2 injection are larger than liquid CO_2 injection.

Two seismic surveys over Teal South Field, Eugene Island, Gulf of Mexico, were acquired at different times, and the numerical models provide important insights to understand changes in the reservoir. 4D seismic differences after cross-equalization show that amplitude dimming occurs in the northeast and brightening occurs in the southwest part of the field. Our forward model, which integrates production data, petrophysicals, and seismic wave propagation simulation, shows that the amplitude dimming and brightening can be explained by pore pressure drops and gas invasion, respectively.

To My Family

ACKNOWLEDGMENTS

First, I'd like to thank my adviser, Dr. Richard L. Gibson, Jr. for suggesting this problem and for his guidance through this project. He was not only a geophysics professor but also counselor, friend, and mentor for me during my Ph.D. study.

Drs. Akhil Datta-Gupta, Sangheon Lee, and Seongsik Yoon gave me an idea and technical instruction on how fluids flow in a reservoir.

As for my fellow students, all of them helped me to survive in the dark cave in the Halbouty building during my Ph.D. study. Among them, I need to make special mention of Costas Tzimeas. He and I were the first Ph.D. students of Dr. Gibson, and we shared a lot of time in our lab and had valuable discussions about our geophysical problems. Veit Matt helped me to not be lonely by staying in the lab during the day and night. Jin Lee was a Korean friend in our group who shared his cigarettes whenever I was stuck on some problem. I'd like to mention that Hung-Liang Lai, Javier Perez, and Pablo Buenapama made my life very joyful.

Lastly I would like to thank my lovely wife, Jungran, my daughter, Joanne, my parents, and my brother in Korea, for their support and patience during my Ph.D. study.

TABLE OF CONTENTS

Page

ABSTRACT iii

DEDICATION v

ACKNOWLEDGMENTS vi

TABLE OF CONTENTS vii

LIST OF TABLES x

LIST OF FIGURES xi

CHAPTER

I INTRODUCTION 1

II THEORIES 5

- 2.1 Overview 5
- 2.2 Introduction 5
- 2.3 Rock physics 6
  - 2.3.1 The Gassmann equation 6
  - 2.3.2 Unconsolidated rock model 8
  - 2.3.3 Consolidated rock model 9
- 2.4 Sequential Gaussian simulation 11
- 2.5 Cloud transform 13
- 2.6 Streamline-based 3D reservoir simulation 17
- 2.7 Ray-Born seismic modeling 20
- 2.8 Integration of time-lapse seismic monitoring theories . . 21
- 2.9 Conclusions 21

III SENSITIVITY ANALYSIS OF TIME-LAPSE SEISMIC AMPLITUDE SIGNALS TO CHANGES IN FLUID SATURATION 22

- 3.1 Introduction 22
- 3.2 Pore-space compressibility 24

CHAPTER Page

3.3 Fluid substitution 27
3.4 Examples 29
3.5 Conclusion 32

IV UNCERTAINTY ANALYSIS IN TIME-LAPSE SEISMIC MODELING 34

4.1 Introduction 34
4.2 Analysis of permeability uncertainties 35
4.2.1 Permeability realizations 35
4.2.2 Streamline simulation for fluid flow 38
4.2.3 Rock-physics modeling 41
4.2.4 Seismic modeling 46
4.3 Analysis of dry bulk modulus uncertainties 49
4.4 Conclusions 52

V TIME-LAPSE SEISMIC MONITORING OF CO_2 SEQUESTRATION IN HYDROCARBON RESERVOIRS: MODEL STUDY 54

5.1 Introduction 54
5.2 Fluid properties 56
5.3 Reservoir modeling 57
5.3.1 Porosity and permeability 59
5.3.2 Fluid flow simulations 60
5.3.3 Rock-physics modeling 62
5.3.4 Seismic modeling 68
5.3.5 Time-lapse AVO analysis 69
5.3.6 Uncertainties in time-lapse seismic modeling . . . 72
5.4 Conclusions 74

VI TIME-LAPSE SEISMIC MONITORING OF A 4500 FT RESERVOIR IN EUGENE ISLAND BLOCK 354 FIELD (TEAL SOUTH), THE GULF OF MEXICO 78

6.1 Introduction 78
6.2 Teal South Field 79
6.2.1 4500-ft reservoir geologic setting 79
6.2.2 Production history 79
6.2.3 Seismic data 81
6.2.4 Processing and analysis of time-lapse seismic data 83
6.3 Modeling 83

CHAPTER Page

6.3.1 Rock physics modeling 83
6.3.2 Fluid saturation modeling 85
6.3.3 Gassmann equation 86
6.3.4 Ray-Born seismic modeling 88
6.4 Conclusions 95

VII CONCLUSIONS 96

7.1 Future work 98

REFERENCES 100

VITA 110

LIST OF TABLES

TABLE Page

5.1 Maximum amplitude changes for four different models. The far-offset SCF CO_2 model shows the largest amplitude changes among these models. 69

6.1 Changes in pore pressure and fluid contents over production period. Pressure is measured from shut-in tubing pressure (SITP) and temperature for 1996 is measured from well logs and assumed to be constant. Saturation is computed from production history (Ashbaugh et al., 2000). 81

LIST OF FIGURES

FIGURE Page

2.1 Dry bulk modulus versus porosity for various effective pressure based on equations 2.3 and 2.4 (modified from Dvorkin and Nur (1996)). 10

2.2 Sequential Gaussian simulation. (a) Original data. (b) Choose random node. (c) Compute local probability distribution using simple kriging. (d) Draw a new value from the `lcpd` (modified from Srivastava, 1994). 12

2.3 Cross plot of permeability versus porosity. Core data are obtained from the Gulf Coast Field (modified from Timur, 1968). 13

2.4 Steps in a cloud transform. (a) Cross plot of permeability versus porosity, showing an example of a subgroup of porosity-permeability pairs. (b) Compute local cumulative distribution function within the subgroup. (c) Unconditional probability field having the same variogram models with porosity (modified from Srivastava, 1992) . . 15

2.5 Porosity field is generated using sequential Gaussian simulation. Permeability field is generated using cloud transform based on porosity field on the left side. 16

2.6 Example of (a) bulk and (b) shear moduli versus porosity (Han et al., 1986). Measured samples include building sandstone, tight gas sandstone, Gulf sandstone, and clean sandstone. 18

2.7 Example of streamline simulation. (a) Permeability field. (b) Streamlines. (c) Water saturation. An injector is located on the left side and a producer is located on the right side (modified from Yoon, 2000). 19

FIGURE Page

3.1 Normalized effective bulk modulus versus porosity for various normalized pore space stiffness with saturated pore fluid. The blue, red, and green curves are computed from dry bulk modulus models from Eberhart-Phillips et al. (1989), Dvorkin and Nur (1996), and Gardner and Harris (1968), respectively. Arrows show the example of changes in pore fluids (modified from Mavko and Mukerji (1995)). 25

3.2 Changes in normalized saturated bulk modulus versus porosity when pore fluid is replaced from oil to water. Gassmann equation is applied to compute these curves. Dry bulk modulus in Gassmann equation for each curve is computed from Gardner and Harris (1968) model (dashed curve), Dvorkin and Nur (1996) model (dotted curve), and Eberhart-Phillips et al. (1989) model (solid curve). 29

3.3 (a) Porosity model is created by sequential Gaussian simulation. (b) Changes in saturated bulk modulus by fluid substitution from oil to brine, based on the unconsolidated model (c) Changes in saturated bulk modulus by fluid substitution from oil to brine based on consolidated model. 31

3.4 (a) Porosity model is created by sequential Gaussian simulation. (b) Amplitude changes by fluid substitution from oil to brine based on unconsolidated model (c) Amplitude changes by fluid substitution from oil to brine based on consolidated model. 33

4.1 Permeability versus porosity from core measurements from different oil fields (Timur, 1968) 36

4.2 A porosity map is generated using sequential Gaussian simulation. Two horizontal variogram models with ranges of 600 m and 300 m in orthogonal directions, respectively, are applied, and the principal axes are rotated to a NE-SW direction to simulate the anisotropy effects. White dots represent the injection well at the center and the production wells at four corners. 37

4.3 Cross plot of permeability versus porosity used for cloud transform. . 38

FIGURE Page

4.4 Examples of realizations of cumulative density functions using sequential Gaussian simulation. The same parameters for variogram models and anisotropy effects are applied from porosity model. White dots represent the injection well at the center and the production wells at four corners. 39

4.5 Examples of permeability realizations using cloud transform. White dots represent the injection well at the center and the production wells at four corners. 40

4.6 Examples of water saturation and pore pressure after 9 year water flooding for permeability realization (a) 1,(b) 2,(c) 20, and (d) 22. White dots represent the injection well at the center and the production wells at four corners. 42

4.7 (a)Mean and (b)standard deviation of brine saturation, and (c)mean and (d)standard deviation of effective pressure for 27 fluid flow simulations. White dots represent the injection well at the center and the production wells at four corners. 44

4.8 Velocity as a function of effective pressure at different water saturations. Red and blue curves show $S_w = 0.2$ and 0.75, respectively. Porosity is assumed to be 20%. 45

4.9 Synthetic seismograms of (a) before, and (b) after brine injection. (c) Amplitude changes are computed by subtraction of traces (b) from traces (a). The same amplitude-normalization factor is applied to plot (a) before-traces, (b) after-traces, and (c) difference traces are applied to different amplitude scale. 47

4.10 Black dots and error bars represent the average amplitude changes and standard deviations, respectively, computed from 27 permeability realizations. The red curve is the standard deviation with the scale on the right axis. 48

4.11 Cross plot of dry bulk modulus versus porosity computed from P and S wave velocities of water saturated sandstones (Han et al., 1986). 49

4.12 Cross plot of dry bulk modulus versus porosity of sandstone based on equation 2.5. 50

FIGURE Page

4.13 Examples of dry-bulk-modulus realizations using the cloud transform. White dots represent the injection well at the center and the production wells at four corners. 51

4.14 Black dots and error bars represent the average amplitude changes and standard deviations, respectively, computed from 27 dry bulk modulus realizations. The red curve is the standard deviation with the scale on the right axis. 52

5.1 CO_2 phase diagram. The critical temperature and critical pressure of CO_2 are 31°C, and 7.4 MPa, respectively. Red and blue bars represent the pressure ranges of liquid and SCF CO_2 in our reservoir simulations, respectively. 56

5.2 (a) Densities and (b) velocities of water, liquid CO_2 at 27°C,and supercritical fluid CO_2 at 77°C as a function of pressure. 58

5.3 Porosity map generated by sequential Gaussian simulation. 59

5.4 Cross plot of permeability to porosity. This is the synthetic example based on the core measurements in the published data. 60

5.5 Permeability generated by cloud transform based on porosity in Figure 5.3. 61

5.6 Fluid simulation results. (a) Saturation and (b) pore pressure of liquid CO_2 model after 180 day injection. (c) Saturation and (d) pore pressure of SCF CO_2 model after 90-day injection. 63

5.7 Cross plots of (a) dry bulk and (b) shear moduli to porosity. These are the synthetic examples based on core measurements in published papers. Mean curves of these scatters are computed from the equations in Dvorkin and Nur (1996). 64

5.8 (a) P-wave velocity and (b) acoustic impedance of a reservoir versus CO_2 saturation for liquid and SCF models based on Gassmann equation. Porosity, bulk and shear moduli, pore pressure, and fluid properties are assumed to be constant to drive these curves. . . 65

FIGURE Page

5.9 (a) P-wave velocity and (b) acoustic impedance of the reservoir versus effective pressure for different pore fluids. CO_2 curves assumed to be 80% CO_2 - or water-saturated. 67

5.10 Seismic amplitudes (a) before liquid CO_2 injection, (b) after liquid CO_2 injection, (c) before SCF CO_2 injection, and (d) after SCF CO_2 injection. 70

5.11 Time-lapse amplitudes for (a) the liquid CO_2 model, and (b) the SCF CO_2 model. 71

5.12 Cross plot of intercept, A, and gradient, B, for time-lapse AVO responses in (a) liquid and (b) SCF CO_2 models. Color scale represents CO_2 saturation. SCF CO_2 model shows a little larger time-lapse AVO responses compared to those in liquid CO_2 model. . 73

5.13 Examples of dry bulk modulus realizations using cloud transform . . 75

5.14 (a) Porosity of resevoir at $X = 0.7$ km. (b) The solid curve and error bars represent the average dry bulk modulus and standard deviations, respectively, computed from 30 dry bulk modulus realizations. The red curve is the standard deviation with the scale on the right axis. (c) The solid curve and error bars represent the average amplitude changes and standard deviations, respectively, computed from 30 sesmic simulations. The red curve is the standard deviation with the scale on the right axis. 76

6.1 (a) Location map of Eugene Island in the Gulf of Mexico. (b) Two vintage maps for 3D streamer survey in 1995 (yellow rectangle) and 3D OBC survey in 1997 (orange rectangle) (Straub et al., 2000). 80

6.2 (a) Base map of Eugene Island, block 354 with two-way traveltime of 4500-ft reservoir. (b) Seismic cross-section from A to A’. The green horizon represents 4500-ft reservoir with two normal faults (Straub et al., 2000). 82

6.3 Amplitude difference of 1995 and 1997 surveys (Straub et al., 2000). . 84

6.4 A porosity model generated using ordinary kriging method, based on three known values from porosity logs. 85

FIGURE Page

6.5 (a) Gas, oil, and water saturation in 1996. (b) Gas, oil, and water saturation in 1997. 87

6.6 (a) P-wave velocity, (b) S-wave velocity, (c) bulk density, and (d) acoustic impedance of 1996 reservoir model. 89

6.7 Changes in (a) P-wave velocity, (b) S-wave velocity, (c) bulk density, and (d) acoustic impedance of the reservoir model during production. 90

6.8 Synthetic seismograms for (a) 1996 reservoir model (b) 1997 reservoir model, and (c) difference traces. 92

6.9 (a) Amplitudes computed from the reservoir model. (b) Amplitudes from field seismic data (Straub et al., 2000). 93

6.10 (a) Amplitude changes computed from reservoir model. (b) Amplitude changes computed from actual field data (Straub et al., 2000). 94

CHAPTER I

INTRODUCTION

Many of the hydrocarbon reserves in the world have already been found and are being rapidly depleted, while at the same time, the worldwide demand for hydrocarbons is increasing significantly. To relieve this problem, it is vital to increase the lifetime of reservoirs and the efficiency of recovery. The recovery rates of most reservoirs are typically low, about 30 to 40 %, in part, because we do not understand the complexity of subsurface fluid flow.

3D seismic surveys provide images of subsurface structures that are now essential tools in the exploration for and production of hydrocarbons, and the cost for these surveys is rapidly decreasing. In turn, the repetition of these surveys over a period of time at a single site can monitor drainage pattern of fluid flow in the subsurface effectively. The formations outside the reservoir generally change only slightly during production, but reservoir properties such as pore pressure, pore fluid, and temperature change significantly. The subtraction of two 3D seismic data acquired at different times, the seismic difference image, can indicate the effects of changes of those reservoir properties on seismic data. Such time-lapse (4D) seismic analysis can then be applied to quantify hydrocarbon drainage patterns and to define secondary recovery strategies. The ultimate goal of 4D seismic monitoring is to detect fluid migration in the subsurface, but in practice, there are several difficulties in achieving this task.

Optimal 4D seismic monitoring requires consistent seismic acquisition and processing, so that the seismic difference image can represent reservoir property changes,

---

This dissertation follows the style and format of Geophysics.

not acquisition or processing artifacts. However, if a repeated survey has different acquisition geometry or parameters, the two data sets must be calibrated before computing the seismic difference image. Another problem in 4D seismic monitoring is that these experiments are not always successful for all reservoirs since fluid migration cannot be detected under some reservoir conditions. Furthermore, the signals in the seismic difference image are quite weak compared to the signals in each survey. Thus, if the signal-to-noise ratio is poor, we might not identify the seismic difference caused by the changes in reservoir properties. Even though the seismic difference image is clearly identified and the signal-to-noise ratio is good, we still may not clearly understand which changes in reservoir properties caused these seismic difference. The time-lapse difference image only shows the combined result of all changes in reservoir properties.

The physical basis of time-lapse seismic monitoring for a reservoir is closely linked to rock physics studies (Nur, 1989). Significant research on the seismic properties of rocks was done in the 1960s and 1970s, and this work became the foundation for the development of new concepts for 4D seismic monitoring. Most early studies based on laboratory measurements show that the seismic velocity of porous rocks depends on porosity, lithology, pressure, temperature, density, pore geometry, and fluid properties (e.g. Gassmann (1951); Toksöz et al. (1976)). The changes in reservoir properties during production include pore pressure, temperature, and pore fluids. Reservoir pore pressure declines near producing wells as fluids are extracted and increases as gas or fluids are injected, which changes seismic velocity (Nur and Simmons, 1969; Toksöz et al., 1976). Reservoir temperature during oil production is quite constant, but injection of cold water into a reservoir decreases temperature in the flooded area, which increases seismic velocities (Wang et al., 1986). Jenkins et al. (1997) showed that hot steam injection into an oil reservoir vaporizes pore fluid into steam, which decreases the seismic velocity. Changes in fluid contents during production, such as the substitution of water or gas for oil, change seismic velocities (Gassmann, 1951; Biot, 1956). The acoustic properties and densities of pore fluids depend on the pressure and temperature conditions in the reservoir (Batzle and Wang, 1992). The design of a geological model is an important step in 4D seismic modeling since the simulation results might be quite different depending on the initial geological model. Comprehensive modeling studies integrating production history, petrophysics, and seismic modeling have been developed (Lumley, 1995; Biondo et al., 1998; Jack, 1998; Johnston et al., 1998; Yuh et al., 2000).

The repeatability of a 3D seismic survey is also an important issue in seismic monitoring, since seismic images can be quite different depending on the acquisition method, such as streamer or ocean bottom cable survey, acquisition direction or geometry, and processing steps. Thus, many techniques have been developed to cross-equalize different 3D seismic data sets before computing the difference images (Eastwood et al., 1999; Rickett and Lumley, 2001). Another area of research in 4D seismic monitoring is the separation of the effects of pressure and saturation changes on seismic reflection amplitudes, since final 4D images include both effects (Aly et al., 1999; Landrø, 2001). Since pressure change in a reservoir is quite broad and smooth, it possibly can obscure the fluid drainage path. One of goals of 4D seismic monitoring is to find bypassed hydrocarbon with comparison of forward model results and images from field data; however, there are significant uncertainties in the simplified reservoir models due to heterogeneity of the earth. Thus, uncertainty estimation in 4D modeling is also an important issue (Sengupta and Mavko, 1999; Landrø, 2002; Yuh and Gibson, Jr., 2002). Another difficulty in 4D seismic modeling is that 3D reservoir volume requires expensive numerical computations.

The primary objective of this thesis is to develop new standard modeling techniques for time-lapse seismic monitoring; techniques that are computationally efficient and provide realistic results. Using these techniques, we try to answer several of the questions we outlined above, including: uncertainties in time-lapse modeling due to uncertainties in model paramertes; effects of elastic properties of a reservoir on 4D images; applications of 4D monitoring to envrionmental problem such as CO_2 sequestration; application of 4D seismic modeling to a real field example.

In chapter II, we discuss the theories involved in time-lapse seismic modeling. The relationships among fluid flow, rock physics, and seismic response are described. Also, geostatistical methods are introduced to facilitate modeling heterogeneous reservoirs.

In chapter III, we investigate the sensitivity of time-lapse seismic amplitude to changes in fluid saturation as a function of porosity with two different bulk-modulus models, which are consolidated and unconsolidated reservoir models. We also compare the 4D images computed from two rock physics models.

Chapter IV discusses uncertainty in time-lapse seismic modeling caused by uncertainties in reservoir properties such as dry bulk modulus and permeability. Multiple realizations of permeability and dry bulk modulus models are generated from one porosity model using the cloud-transform technique. Synthetic 2D time-lapse seismic profiles across the reservoir demonstrate variability in the time-lapse signals.

In chapter V, we discuss the application of time-lapse seismic monitoring to CO_2 sequestration in a subsurface reservoir. Using our modeling techniques, we compare the 4D seismic images of CO_2 injection models for two different CO_2 phases, liquid and super critical fluid CO_2 .

In chapter VI, we apply our modeling techniques to a field example. We develop a forward model for the 4500 ft reservoir in the Eugene Island, block 354 field (Teal South), the Gulf of Mexico, based on well logs, production history, a rock physics model, and a seismic model.

CHAPTER II

THEORIES

2.1 Overview

In this chapter, we discuss theoretical results that relate changes in elastic properties, and, therefore, seismic images, to variations in pore fluid contents and rock properties such as porosity. Combining these results provides the basis for the complete procedure for forward modeling of time-lapse seismic monitoring. This includes rock-physics modeling, fluid simulation, and seismic modeling to predict time-lapse seismic responses caused by reservoir property changes.

2.2 Introduction

The ultimate goal of time-lapse seismic monitoring is to detect changes in reservoir properties such as pore fluid contents and pressure during production. An accurate interpretation of the results of time-lapse seismic experiments requires an understanding of basic rock physics relating changes in subsurface fluids to variations in the elastic proprieties of a reservoir. It is also essential to understand which reservoir properties have the most significant influence on the magnitude of time-lapse seismic responses. To address these issues and to provide a basis for subsequent chapters, we summarize the theories involved in time-lapse seismic monitoring in this chapter. First, to consider the fluid effects on the bulk modulus of porous rock, we apply the Gassmann equation (Gassmann, 1951). The assumptions, limitations, and advantages of this Gassmann model are also discussed. The dry bulk modulus of the rock frame in the Gassmann equation is one of major parameters that controls changes in saturated-rock seismic velocities. Thus we propose two general models for the dry bulk modulus representing unconsolidated sands and consolidated sandstones to investigate the sensitivity of amplitude changes to changes in fluid saturation for two broad classes of realistic reservoir materials. (Eberhart-Phillips et al., 1989; Dvorkin and Nur, 1996). Next, to mimic heterogeneous reservoir properties, we applied stochastic methods, a sequential Gaussian simulation and the cloud transform (Srivastava, 1992; Deutsch and Journel, 1998). Fluid flow in a reservoir is simulated using the streamline method, which is an efficient and fast algorithm suitable for stochastic modeling or reservoir characterization studies (King and Datta-Gupta, 1998). The final step is the seismic-wave-propagation modeling, which we performed using the ray-Born method. This method is also a fast method suitable for time-lapse study so that we can test seismic models having different reservoir properties within a reasonable time period (Gibson, Jr. et al., 1993).

2.3 Rock physics

2.3.1 The Gassmann equation

The effects of pore fluids on the elastic properties of the rock frame can be computed using the Gassmann equation (Gassmann, 1951). In the Gassmann model, a rock is assumed to be a porous skeleton that moves together with the pore fluid. In this equation, the fluid-saturated bulk modulus of a rock is expressed as

$$\kappa \;=\; \kappa^* + \frac{\left(1 - \frac{\kappa^*}{\kappa_s}\right)^2}{\phi\left(\frac{1}{\kappa_f} - \frac{1}{\kappa_s}\right) + \frac{1}{\kappa_s}\left(1 - \frac{\kappa^*}{\kappa_s}\right)}, \tag{2.1}$$

where κ^* is dry bulk modulus, κ_s is mineral bulk modulus, κ_f is fluid bulk modulus, and ϕ is porosity.

The derivation of this Gassmann equation assumes that the rock is subject to the following conditions (Gassmann, 1951; Cheng, 1978; Mavko et al., 1998):

- Low frequency, such that induced pore pressure is equilibrated throughout the pore space.
- No fluid enters or leaves the Gassmann model, which means pore volume changes are equal to fluid volume changes under pressure increments.
- The pores are interconnected to each other and pore pressure is communicated throughout the rock volume.
- The theory implicitly assumes that dry- and fluid- saturated shear moduli are same.

Because of the above conditions, the Gassmann equation cannot be applied directly to consider the effects of pressure dependency, pore geometry, or heterogeneous matrix.To overcome some of these limitations, we can apply following solutions:

- If the matrix of rocks is composed of multiple minerals such as quartz and feldspar, we can apply the average moduli to compute effective matrix bulk modulus.
- The Gassmann equation does not consider the dependence of effective bulk modulus on pore geometry, even though this geometry may affect the dry frame bulk modulus. To consider pore geometry, we can apply theoretical models to compute effective dry bulk modulus, κ^*, of different pore geometries (Kuster and Toksöz, 1974; Cheng, 1978).

- To consider pressure dependence, we can apply empirical relations of dry bulk modulus versus pressure (Eberhart-Phillips et al., 1989) or theoretical models (Cheng and Toksöz, 1979; Dvorkin and Nur, 1996).

Furthermore, when the pore fluid is a mixture of two different fluids, Wood's equation can compute the effective modulus:

$$\frac{1}{\kappa_f} = \frac{S_l}{\kappa_{liquid}} + \frac{1 - S_l}{\kappa_{gas}} \tag{2.2}$$

where κ_{liquid} and κ_{gas} are bulk moduli of liquid and gas, respectively, and S_l is liquid saturation.

2.3.2 Unconsolidated rock model

The effective bulk and shear moduli of a random, dense pack of identical spheres are expressed as

$$\begin{aligned} K_{HM} &= \left(\frac{n^2(1-\phi_0)^2 G^2}{18\pi^2(1-\nu)^2} P \right)^{1/3}, \\ G_{HM} &= \frac{5-4\nu}{5(2-\nu)} \left(\frac{3n^2(1-\phi_0)^2 G^2}{2\pi^2(1-\nu)^2} P \right)^{1/3}, \end{aligned} \tag{2.3}$$

where n is average number of contacts per grain, G is grain shear modulus, ϕ_0 is critical porosity, P is effective pressure, and ν is the Poisson's ratio (Mindlin, 1949). This equations can be applied to precompacted granular rocks with the assumption that there is no slip at sphere contact (Mavko et al., 1998). Critical porosity, ϕ_0, is the limit of high porosity, where rock behaves like a suspension beyond this point (Nur et al., 1995).

To generalize the above equation for different porosity values, Dvorkin and Nur (1996) developed the modified Hashin-Shtrikman lower bound (Hashin and Shtrikman, 1963)

$$\begin{aligned}
K_{eff} &= \left(\frac{\phi/\phi_0}{K_{HM} + \frac{4}{3}G_{HM}} + \frac{1-\phi/\phi_0}{K + \frac{4}{3}G_{HM}} \right)^{-1} - \frac{4}{3}G_{HM}, \\
G_{eff} &= \left[\frac{\phi/\phi_0}{G_{HM} + \frac{G_{HM}}{6}\left(\frac{9K_{HM}+8G_{HM}}{K_{HM}+2G_{HM}}\right)} \right. \\
&\qquad \left. + \frac{1-\phi/\phi_0}{G + \frac{G_{HM}}{6}\left(\frac{9K_{HM}+8G_{HM}}{K_{HM}+2G_{HM}}\right)} \right]^{-1} \\
&\qquad - \frac{G_{HM}}{6}\left(\frac{9K_{HM}+8G_{HM}}{K_{HM}+2G_{HM}}\right),
\end{aligned} \tag{2.4}$$

where K is grain bulk modulus and ϕ is porosity. Figure 2.1 is an example of dry bulk modulus versus porosity as a function of pressure, based on equations 2.3 and 2.4, showing typical, nonlinear trends for unconsolidated sands.

Th advantages of the above equations are that the effective moduli are expressed as functions of pressure and porosity, which is quite suitable for rock-physics modeling of time-lapse seismic monitoring. This model also matches well with measured velocities of unconsolidated sands (Blangy et al., 1993).

2.3.3 Consolidated rock model

Effective-medium theories have been studied to estimate elastic properties of composite porous medium. One approach is to use the bounding methods that limit the upper and lower bounds of elastic moduli when properties and volume fractions of each component are known (Reuss, 1929; Hashin and Shtrikman, 1963). Other approaches consider the pore geometry and spatial distributions of the components based on first order scattering theories (Kuster and Toksöz, 1974). Self consistent approximations (Budiansky, 1965) extend Kuster and Toksöz's model to higher concentrations of inclusions by replacing the background medium with the effective medium using a

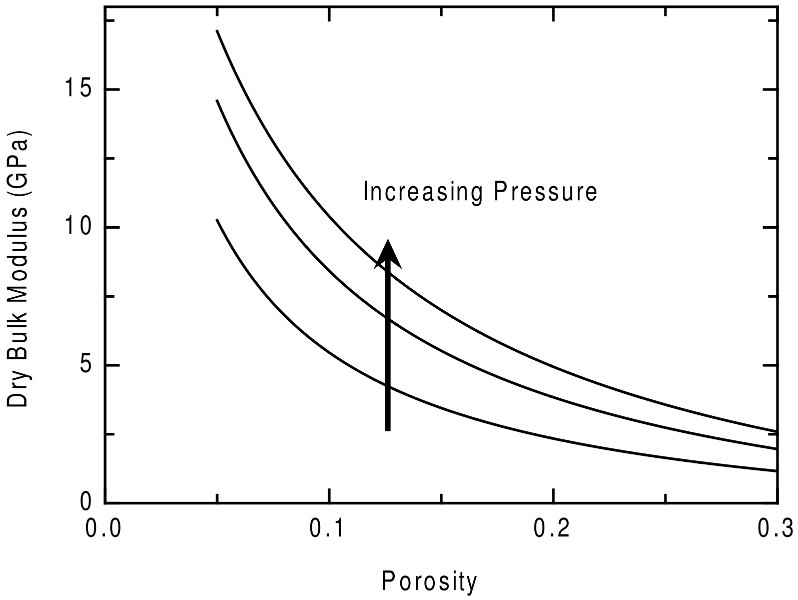

Fig. 2.1. Dry bulk modulus versus porosity for various effective pressure based on equations 2.3 and 2.4 (modified from Dvorkin and Nur (1996)).

recursive method.

In our reservoir modeling for consolidated sandstone, we employ empirical equations of P- and S-wave velocities in terms of porosity, clay content, and effective pressure (Eberhart-Phillips et al., 1989). The advantages of this empirical model are that information about the pore geometry is not required and effects of clay content on velocities can be considered. Han et al. (1986) measured ultrasonic P- and S-wave velocities of water-saturated sandstones over an effective pressure range of 1 to 49 MPa. The confining pressure varied from 1 to 80 MPa with the pore-pressure range of 0 to 40 MPa. The clay content was measured by point counting. Eberhart-Phillips et al. (1989) developed the empirical equations based on Han et al.'s measurements. P- and S-wave velocities can be predicted using (Eberhart-Phillips et al., 1989)

$$\begin{aligned} V_p &= 5.77 - 6.94\phi - 1.73\sqrt{C} + 0.446(P_e - e^{-16.7P_e}) \\ V_s &= 3.70 - 4.94\phi - 1.57\sqrt{C} + 0.361(P_e - e^{-16.7P_e}), \end{aligned} \tag{2.5}$$

where ϕ is porosity, C is clay content, and P_e is effective pressure. Each of the coefficients in these equations was determined by regression. To compute changes in *dry*-frame bulk modulus, κ^*, in time-lapse seismic modeling, we first solved the above equations for water-saturated bulk modulus and shear modulus, and applied the Gassmann equation to compute the dry bulk modulus (Gassmann, 1951). Then, the elastic moduli of the reservoir model can be expressed in terms of porosity and pressure. By using these equations to estimate κ^* at arbitrary values of pressure and porosity, it is straightforward to estimate velocities in saturated rock using the Gassmann equation.

2.4 Sequential Gaussian simulation

The stochastic modeling method has two major advantages in reservoir modeling: First, it can consider heterogeneity of the earth. In most reservoir modeling, the available information is sparse well logs. Traditional method for modeling is homogeneous layer cake stratigraphy, lithologic units that are continuous to next well or pinch out. However, the stochastic technique can generate a realistic level of heterogeneity. Thus it is closer to real earth than traditional, simplified, smooth reservoir model (Srivastava, 1994). Second, the stochastic method can generate multiple equally-probable models that honor all the hard data. Thus, it is quite useful for estimating uncertainties in our reservoir models (Deutsch and Journel, 1994). In our stochastic modeling, we applied sequential simulation, which recursively computes a value at random nodes based on the original data plus previously simulated values (Deutsch and Journel, 1998). Specifically, we applied sequential Gaussian simulation for our porosity modeling which assumes that the probability distribution of the data follows Gaussian distribution. The steps of sequential Gaussian simulation are as follows

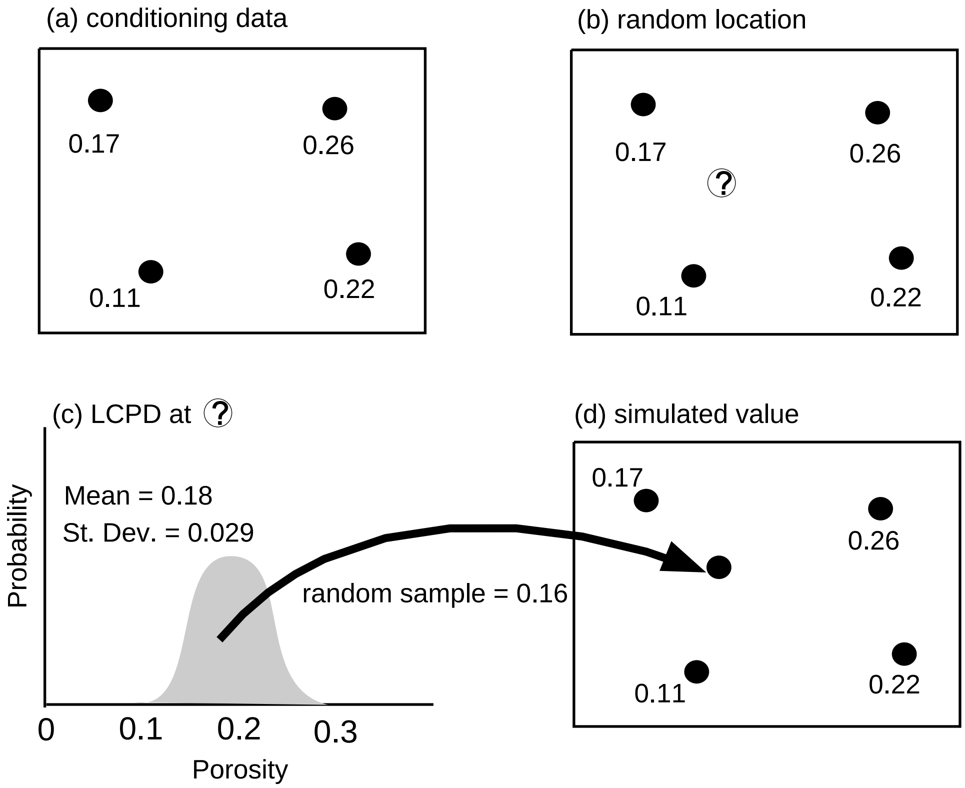
(a) conditioning data
0.17
0.26
0.11
0.22
(b) random location
0.17
?
0.26
0.11
0.22
(c) LCPD at ?
Mean = 0.18
St. Dev. = 0.029
Probability
random sample = 0.16
0
0.1
0.2
0.3
Porosity
(d) simulated value
0.17
0.26
0.11
0.22

Fig. 2.2. Sequential Gaussian simulation. (a) Original data. (b) Choose random node. (c) Compute local probability distribution using simple kriging. (d) Draw a new value from the `lcpd` (modified from Srivastava, 1994).

(Srivastava, 1994; Deutsch and Journel, 1998) (Figure 2.2):

- Determine the node to be simulated at random.
- Determine the local conditional probability distribution (`lcpd`) at that location using a simple kriging method.
- Draw a simulated value from the `lcpd`.
- Add the simulated value to the conditioning data.
- Repeat the above steps until all nodes are simulated.

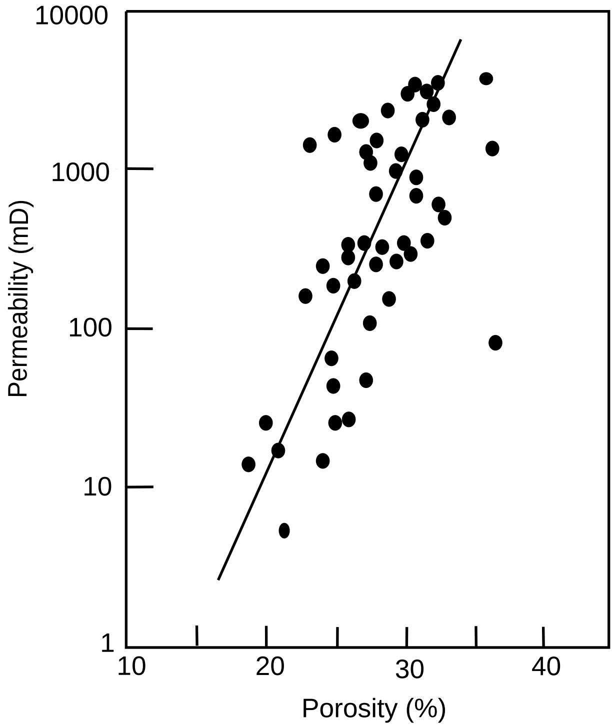

Fig. 2.3. Cross plot of permeability versus porosity. Core data are obtained from the Gulf Coast Field (modified from Timur, 1968).

2.5 Cloud transform

The cloud transform is a probability-field simulation for estimating an unknown reservoir property based on another known property (Srivastava, 1992). For example, it can estimate permeability for a reservoir model based on a known porosity model. The advantages of the cloud-transform approach are that it honors the relationship between properties such as porosity and permeability, and that it preserves the heterogeneity of the property (Aly et al., 1999). It also honors the spatial continuity of the reservoir property (Srivastava, 1992). For example, many laboratory measurements show that the permeability-porosity relationship has a log-linear trend (Figure 2.3) (Timur, 1968), but conventional regression methods estimating a linear function fitting the data can not preserve the variability (the scatter) of the data.

The steps involved in a cloud transform to generate permeability from a porosity map are as follows (Srivastava, 1992; Aly et al., 1999) (Figure 2.4):

- The first step in the cloud transform is to generate a scatter plot of porosity/permeability based on core measurements. In our modeling, we generated a synthetic cross plot using a Gaussian random function and a log-linear function (Figure 2.4a).

- Divide the entire range of porosity into subgroups and compute the local cumulative distribution function of each subgroup (Figure 2.4a and b). If a subgroup is too small, output realization may be too heterogeneous and if it is too large, output realization may be too smooth.

- Simulate an unconditional probability field based on the same variogram models with porosity. In our modeling, we used sequential Gaussian simulation to generate the probability field (Figure 2.4c).

- Pick a cumulative probability value from the unconditional probability field and estimate the permeability value using the CDF curve (Figure 2.4b).

An example of permeability field computed using cloud transform is shown in Figure 2.5. Both fields have similar anisotropic trends in the direction of north-east and south-west. The high-porosity region correlates well with the high-permeability region, but details of both fields are different.

If we repeat the above steps using multiple realizations of unconditional probability fields, we can generate multiple realizations of permeability models that are equally probable. Thus, we can apply this technique to estimate the uncertainty analysis in reservoir properties. For example, dry bulk and shear moduli are inversely proportional to porosity with large scatter, much like porosity/permeability, because

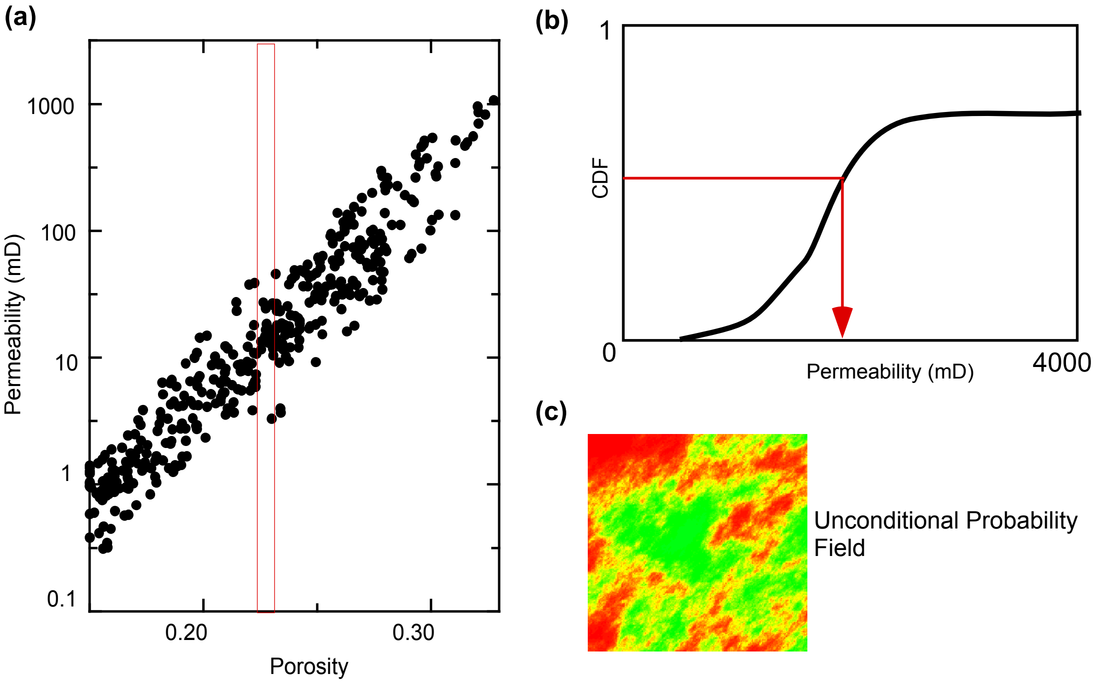

Fig. 2.4. Steps in a cloud transform. (a) Cross plot of permeability versus porosity, showing an example of a subgroup of porosity-permeability pairs. (b) Compute local cumulative distribution function within the subgroup. (c) Unconditional probability field having the same variogram models with porosity (modified from Srivastava, 1992)

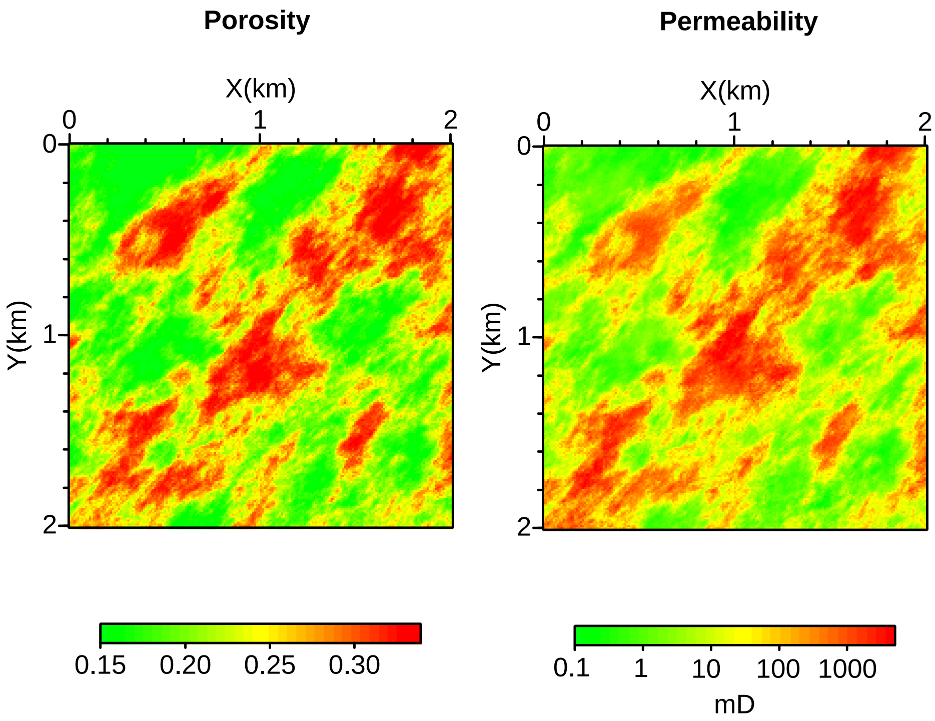

Fig. 2.5. Porosity field is generated using sequential Gaussian simulation. Permeability field is generated using cloud transform based on porosity field on the left side.

of earth heterogeneity (Han et al., 1986) (Figure 2.6). Thus we can also apply the cloud transform technique to simulate multiple realizations of elastic moduli to estimate the uncertainties in time-lapse response.

2.6 Streamline-based 3D reservoir simulation

The streamline method is applied to simulate fluid flow in a reservoir. The advantages of this method compared to conventional, finite-difference schemes are its fast computation speed and relatively small numerical diffusion. Thus this method is quite appropriate for large size, heterogeneous, multiwell, and multiphase simulations (King and Datta-Gupta, 1998; Crane and Blunt, 1999).

The procedure for streamline simulation involves: (1) solving for the pressure field based on petrophysical properties, (2) tracing streamlines based on the velocity field, (3) computing traveltime of tracer along streamlines, (4) transforming coordinates from 3D physical space to 1D traveltime coordinate, (5) Solving 1D saturation equation along the streamlines, (6) updating the pressure field occasionally (Yoon, 2000).

In this study we used the S3D streamline simulator developed at Texas A&M University (Yoon, 2000). The S3D simulator assumes two-phase incompressible flow without considering gravitational effects. Examples of fluid-simulation results using S3D are shown in Figure 2.7. We can notice the high density of streamlines located in the high-permeability zone.

There exists an analogy between the migration of a water front and wave propagation. The streamline time of flight equations have the same form as the eikonal equations in ray theory (Vasco et al., 1999). Ray theory is a high-frequency, asymptotic solution of the wave equation, which assumes that the medium properties vary

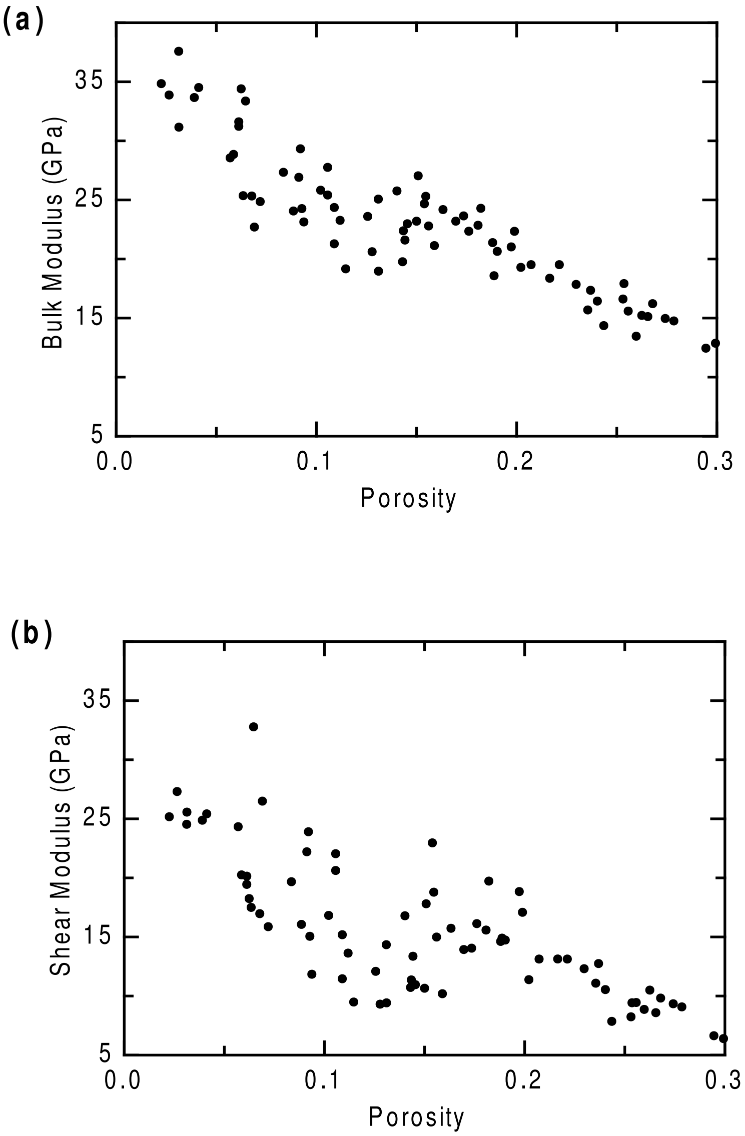

Fig. 2.6. Example of (a) bulk and (b) shear moduli versus porosity (Han et al., 1986). Measured samples include building sandstone, tight gas sandstone, Gulf sandstone, and clean sandstone.

(a)

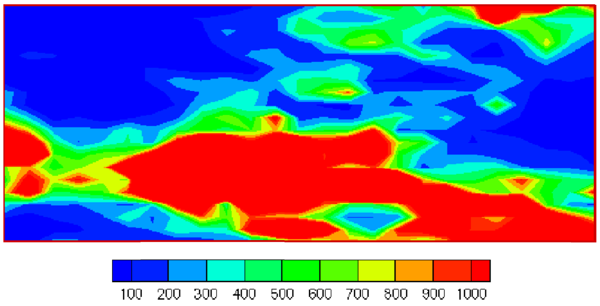

Permeability Field (md)

(b)

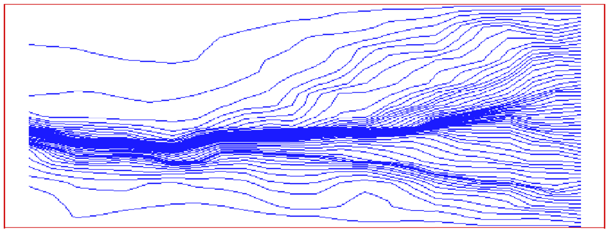

Streamlines

(c)

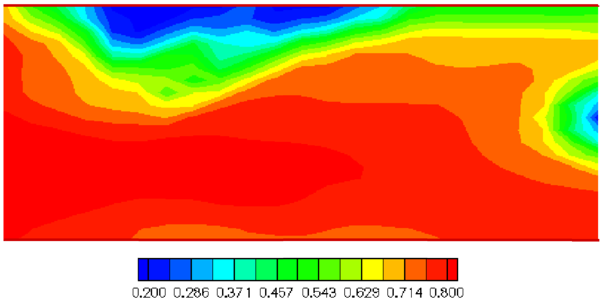

Water Saturation Distribution

Fig. 2.7. Example of streamline simulation. (a) Permeability field. (b) Streamlines. (c) Water saturation. An injector is located on the left side and a producer is located on the right side (modified from Yoon, 2000).

smoothly (Červený, 2001). Likewise, the streamline simulation assumes velocity field changes smoothly, even though this can be overcome by updating the streamlines.

2.7 Ray-Born seismic modeling

Synthetic seismograms for use in modeling the time-lapse seismic image of a reservoir are computed using ray-Born algorithm (Beydoun and Mendes, 1989; Gibson, Jr. and Ben-Menahem, 1991; Gibson, Jr. et al., 1993). This method is a hybrid method combining ray theory and the Born approximation. The Born approximation is a linear approximation for the scattered wavefield generated by localized perturbations of elastic properties and densities in a given background medium (Miles, 1960; Hudson and Heritage, 1981; Wu and Aki, 1985; Gibson, Jr. and Ben-Menahem, 1991). The scattered displacements in heterogeneous and anisotropic media can be expressed in terms of the Green's tensor and displacements in the background medium (Gibson, Jr. and Ben-Menahem, 1991). To compute the Green's tensors in the background medium, dynamic raytracing with paraxial approximation is applied, assuming a smooth background medium (Gibson, Jr. et al., 1993; Červený, 2001). The perturbed region is discretized and an individual cell acts as secondary source. Perturbations of the density and elastic constants act as a single force source and moment tensor, respectively (Wu and Aki, 1985). The scattered wavefield is computed by summing the contribution of each scattering element. The conditions in ray-Born methods are that the background is a smoothly varying medium to which we apply the ray tracing to compute the Green's tensor; and that perturbations to the elastic constants and density should be relatively weak to validate the first-order Born approximation. Also, the perturbed region must be small since the wave propagation only occurs in the background (Beydoun and Tarantola, 1988; Gibson, Jr. et al., 2000).

2.8 Integration of time-lapse seismic monitoring theories

Modeling of time-lapse seismic monitoring is the integration of the theories described in the previous sections. The first step in our modeling starts with creating a heterogeneous porosity field using sequential Gaussian simulation and well logs. Then, the permeability field is computed using the cloud transform based on the porosity field. Based on permeability and porosity, we perform streamline fluid simulation to compute fluid saturation and pore-pressure distribution over a certain time period. The next step is rock-physics modeling. Based on theoretical rock-physics models or empirical equations of seismic velocities, we can derive the elastic moduli in terms of porosity and pressure. The final step of time-lapse seismic modeling is computing synthetic seismograms for different times using ray-Born seismic modeling.

2.9 Conclusions

We have discussed theories in rock physics for fluid substitution and elastic properties. Based on these theories we have linked the fluid flow in a reservoir to time-lapse seismic responses. We have also showed the stochastic modeling methods to consider the heterogeneity of the earth and uncertainty analysis in time-lapse seismic monitoring.

CHAPTER III

SENSITIVITY ANALYSIS OF TIME-LAPSE SEISMIC AMPLITUDE SIGNALS TO CHANGES IN FLUID SATURATION

3.1 Introduction

Time-lapse seismic monitoring is a repeated application of 3D seismic surveys over a period of time to estimate changes in reservoir properties such as fluid contents and pore pressure during production. However, this technique is not always successful because of unfavorable reservoir conditions or changing survey procedures, even though processing methods often assume perfect seismic repeatability (Lumley et al., 1997). Thus it is important to understand which physical conditions of a reservoir control the time-lapse seismic response to determine when the method is likely to be successful prior to expending the effort to acquire data.

Lumley et al. (1997) developed a set of criteria to quantify success rate of 4D seismic projects. The major petrophysical properties affecting 4D images are effective pressure, dry bulk modulus, porosity, fluid saturation change, and fluid properties. For example, if the rock frame is quite soft, as would be the case for unconsolidated sands, the saturated bulk modulus is quite sensitive to fluid compressibility. However, since reservoir parameters are also related to each other, it is difficult to interpret final results of time-lapse seismic data quantitatively (Wang, 1997).

We have tested a number of different 4D seismic models having a variety of reservoir properties using our fast modeling techniques and have found some results of 4D seismic images cannot be explained by these results of previously published papers. High porosity rock is believed to be more favorable to 4D seismic than low porosity rocks, since a larger amount of fluid is replaced for high porosity rock than low porosity rock (Lumley et al., 1997). This in turn causes greater changes in elastic properties. However, our modeling results are not fully consistent with this explanation. When we model the heterogeneous reservoir having elastic moduli for unconsolidated rock, the amplitude changes after fluid substitution show that high porosity region shows smaller amplitude changes than lower porosity region. This means that there is no unique rule for the relation between amplitude change in time-lapse seismic monitoring and rock porosity, even though most sedimentary rocks show lower velocity at higher porosities and higher velocity at lower porosities. Thus we need to understand the effects of porosity and elastic properties of a reservoir on time-lapse amplitude. To solve this problem, we used Mavko and Mukerji (1995)'s method to explain the sensitivity of bulk modulus to changes in fluid saturation, which is basically a graphical interpretation of Gassmann equation. In this method they derived another expression of Gassmann equation using pore-space compressibility and they found that increasing pore-space compressibility increases the sensitivity of bulk modulus to changes in pore fluids at constant porosity (Mavko and Mukerji, 1995).

In this chapter, we expand their analysis further to understand the sensitivity of bulk modulus to changes in pore fluid as a function of porosity for two different reservoir models, corresponding to consolidated and unconsolidated formations. In the first part, we summarize the definition of pore-space compressibility and present graphical results to facilitate an analysis of the Gassmann equation. Then, we apply this method to two reservoir models.

3.2 Pore-space compressibility

Pore-space compressibility is the rock-physics parameter defined by the ratio of change in pore volume to pressure variation in a porous medium. This property directly links pore fluid changes to effective bulk moduli, so it helps to understand the Gassmann equation and amplitude changes in time-lapse seismic monitoring. The compressibility of the dry rock frame at constant pore pressure can be expressed as (Walsh, 1965; Zimmerman, 1991)

$$\frac{1}{K_d} = \frac{1}{K_0} + \frac{\phi}{K_\phi}, \tag{3.1}$$

where K_0 is mineral bulk modulus, K_ϕ^{-1} is effective dry rock pore-space compressibility, and ϕ is porosity. K_ϕ^{-1} is defined as

$$\frac{1}{K_\phi} = \frac{1}{\nu_p} \frac{\partial \nu_p}{\partial \sigma}\bigg|_p, \tag{3.2}$$

where ν_p is pore volume, σ is external hydrostatic stress, and p is pore pressure. Note that K_ϕ^{-1} is not fluid compressibility. In equation 3.1, increasing the pore-space compressibility, K_ϕ^{-1}, decreases the rock frame dry bulk modulus, K_d, which causes a decrease in seismic velocity. The saturated rock compressibility, K_s^{-1}, can be expressed as (Mavko and Mukerji, 1995)

$$\frac{1}{K_s} = \frac{1}{K_0} + \frac{\phi}{\widetilde{K}_\phi}, \tag{3.3}$$

where

$$\widetilde{K}_\phi = K_\phi + \frac{K_0 K_f}{K_0 - K_f}, \tag{3.4}$$

where K_f is fluid bulk modulus and K_ϕ is the dry pore space stiffness in equation 3.1. The above equations assume there is no fluid-induced pressure gradient, which is the same as the low frequency assumption in the Gassmann equation. The difference between equation 3.1 and 3.3 is that the term $\widetilde{K}_\phi$ in equation 3.3 includes the fluid

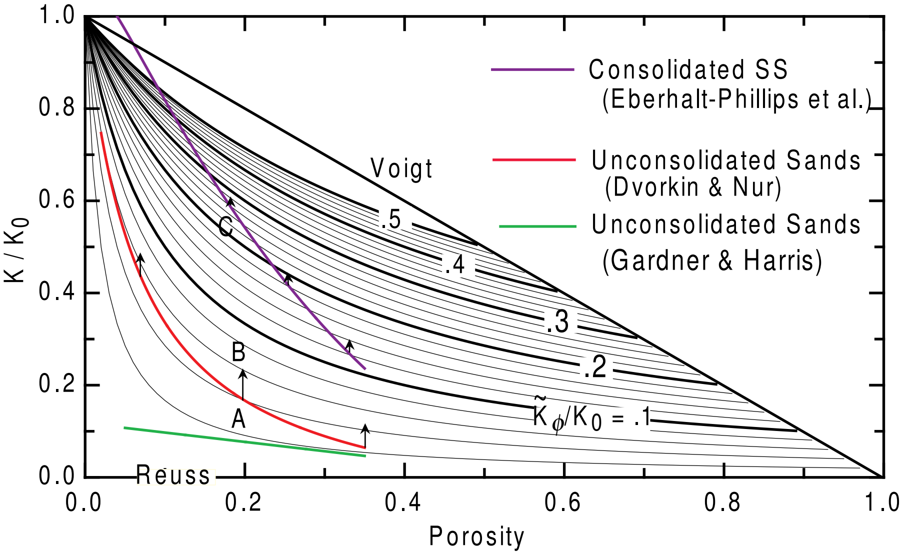

Fig. 3.1. Normalized effective bulk modulus versus porosity for various normalized pore space stiffness with saturated pore fluid. The blue, red, and green curves are computed from dry bulk modulus models from Eberhart-Phillips et al. (1989), Dvorkin and Nur (1996), and Gardner and Harris (1968), respectively. Arrows show the example of changes in pore fluids (modified from Mavko and Mukerji (1995)).

term

$$F = (K_0 K_f)/(K_0 - K_f). \tag{3.5}$$

Values of the normalized saturated bulk modulus, K_s/K_0, computed as a function of porosity using equation 3.3, are shown for various values of $\widetilde{K}_\phi/K_0$ in Figure 3.1. In Figure 3.1, each curve corresponds to a single value of saturated pore-space compressibility, thus displaying changes in rock properties for a particular pore fluid, if the grain and pore space moduli are held constant. Thus, if $K_f = 0$, the vertical axis in Figure 3.1 represents the normalized dry bulk modulus, and if $K_f \neq 0$, it represents the normalized saturated bulk modulus. These contours fall between the Voigt and Reuss upper and lower bounds if the K value used in the ratio K/K_0 (the value on the vertical axis) represents dry-rock bulk modulus (Mavko et al., 1998). The value of $\widetilde{K}_\phi$ depends on the pore space, fluid and solid grain moduli, so to better compare the predicted variations in properties to real media, we superimposed the values computed using three different dry bulk modulus models on the normalized pore-space compressibility contours. The blue curve in Figure 3.1 is an empirical model of dry bulk modulus obtained from ultrasonic velocities of a variety of water saturated, consolidated sandstones (Eberhart-Phillips et al., 1989). The red curve in Figure 3.1 shows the dry bulk modulus values computed from a model based on Hertz-Mindlin contact theory with the modified Hashin-Shtrikman lower bound (Dvorkin and Nur, 1996), representing unconsolidated sands. The green curve in Figure 3.1 is empirical model of dry bulk modulus obtained from P- and S- wave velocities of freshly packed sands (Gardner and Harris, 1968). In the consolidated model, the bulk modulus shows a relatively high, steep gradient and almost linear trend with respect to porosity. In contrast, the unconsolidated model (Dvorkin and Nur, 1996) shows relatively smaller values and a nonlinear trend with respect to porosity. These characteristics are typical for most unconsolidated sands and consolidated sandstones (Blangy et al., 1993). Both reservoir models, the red and blue curves in Figure 3.1, cross contours of constant $\widetilde{K}_\phi$, which means that the pore-space compressibility typically decreases (softer rock) with increasing porosity. The Gardner and Harris (1968) results, based on comparatively old measurements, display different trend than Hertz-Mindlin model prediction, with a gradual, linear reduction in K/K_0 with porosity. Though different from the larger number of measurements presented by Blangy et al. (1993), the values still emphasize the different behavior of unconsolidated sands.

3.3 Fluid substitution

The Gassmann equation predicts that the bulk modulus is a function of changes in fluid saturation via changes in the fluid modulus K_f (Gassmann, 1951):

$$K = K^* + \frac{\left(1 - \frac{K^*}{K_s}\right)^2}{\phi\left(\frac{1}{K_f} - \frac{1}{K_s}\right) + \frac{1}{K_s}\left(1 - \frac{K^*}{K_s}\right)}, \tag{3.6}$$

where κ^* is dry bulk modulus, κ_s is mineral bulk modulus, κ_f is fluid bulk modulus, and ϕ is porosity. The above equation can also be derived from equations 3.1, 3.3, and 3.4 by eliminating the K_ϕ term. Thus, the effect of fluids on the effective bulk modulus can be estimated from both equations. Mavko and Mukerji (1995) described a graphical technique to measure changes in effective bulk modulus by changes in fluid saturation using the following steps (Figure 3.1):

1. Point A in Figure 3.1 is the known-saturated bulk modulus with fluid 1. Read the value of pore-space compressibility on the contour corresponding to point A.

2. Compute the fluid term, F, in equation 3.5 for both the original fluid 1 and the new fluid 2, and then compute the changes in the fluid term by subtracting F_{fluid1} from F_{fluid2}.

3. From the original point A of the saturated bulk modulus with fluid 1, move vertically up or down a number of contours corresponding to ΔF computed in the previous step, and then read the new saturated bulk modulus on the left axis (e.g., move up from point A to B in Figure 3.1).

This graphical technique assumes no dry bulk modulus change during fluid substitution, or, in other words, no pressure change. This method can be applied to any kind of fluid substitution such as from oil to water or even from dry to any fluid. In Figure 3.1, at a fixed porosity value, a contour interval of $\widetilde{K}_\phi/K_0$ is wider for low bulk modulus (point A) and tighter for high bulk modulus (point C). In other words, the sensitivity of bulk modulus to changes in fluid modulus is larger at point A than at point B with the same amount of change in fluid modulus.

Sensitivities of bulk modulus to changes in fluid saturation for consolidated (Eberhart-Phillips et al., 1989) and unconsolidated (Dvorkin and Nur, 1996; Gardner and Harris, 1968) reservoir models are computed in Figure 3.2 using Gassmann equation. The vertical axis in Figure 3.2 represents changes in normalized, effective bulk modulus, $\Delta K/K_0$, when pore fluid is replaced from oil to water. Thus, these curves represent the sensitivity of bulk modulus to changes in fluid saturation as a function of porosity. The bulk moduli of oil and brine are assumed to be 1.8 and 3.9 GPa, respectively. One of the unconsolidated models, the dashed curve in Figure 3.2, shows an almost linear relationship between porosity and change in bulk modulus for porosiy > 0.08. The other unconsolidated model, the doted curve in Figure 3.2, shows that changes in bulk modulus, $\Delta K/K_0$, increase with increasing porosity up to porosity values of about 0.14, and decrease with increasing porosity up to a porosity of 0.4. Thus second model is probably more realistic, as it displays behavior similar to a larger number of measurements (Blangy et al., 1993). Thus there is no direct correlation between sensitivity of bulk modulus to changes in fluid saturation and porosity. However, the consolidated model, solid curve in Figure 3.2, shows that the sensitivity of bulk modulus to changes in fluid saturation increases constantly with increasing porosity. Another observation is that the unconsolidated rock models shows much higher $\Delta K/K_0$ than the consolidated rock model over the entire porosity range, which is quite obvious since softer rock is more sensitive to the changes in fluid saturation.

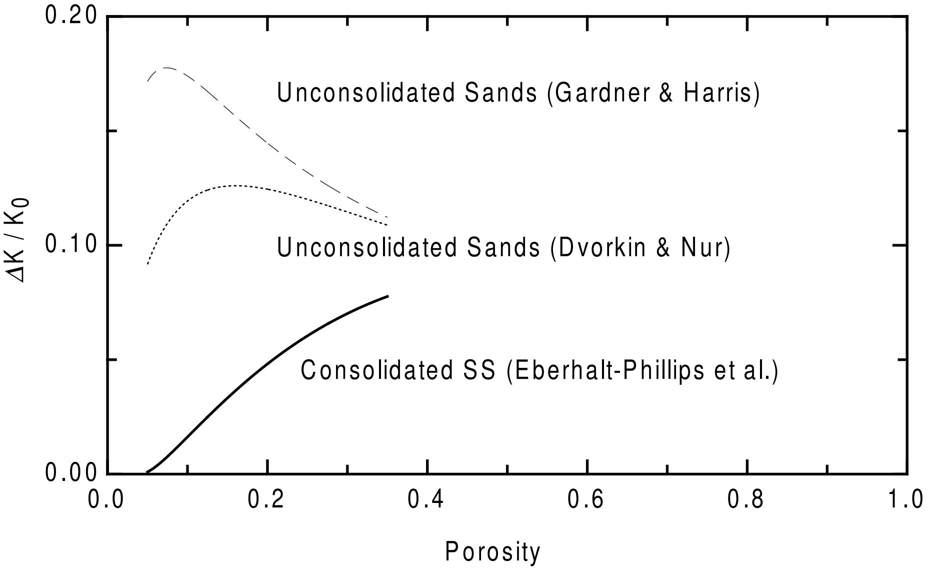

Fig. 3.2. Changes in normalized saturated bulk modulus versus porosity when pore fluid is replaced from oil to water. Gassmann equation is applied to compute these curves. Dry bulk modulus in Gassmann equation for each curve is computed from Gardner and Harris (1968) model (dashed curve), Dvorkin and Nur (1996) model (dotted curve), and Eberhart-Phillips et al. (1989) model (solid curve).

3.4 Examples

We tested two time-lapse seismic models based on the models of unconsolidated and consolidated formations (Dvorkin and Nur model, and Eberhalt-Phillips et al. model, respectively) to test the sensitivity of 4D amplitude to changes in fluid saturation.

Our reservoir model has a horizontal reservoir layer, and the overburden layer has homogeneous velocity and density. The model dimensions are 2000 x 2000 x 10 m and it is discretized to a block with size of 10 x 10 x 10 m. A heterogeneous porosity model is created using sequential Gaussian simulation (Deutsch and Journel, 1998). The porosity ranges from 0.05 to 0.3 (Figure 3.3a). We assumed the reservoir is initially saturated with 100% oil. To estimate only the effects of fluid substitution on the 4D seismic image, we assumed the pore fluid is replaced by 100% brine and no pressure changes. To apply fluid substitution calculations, the Gassmann equation is applied (equation 3.6). Two models for dry bulk modulus, K^*, in equation 3.6, are consolidated sandstone (Eberhart-Phillips et al., 1989) and unconsolidated sands (Dvorkin and Nur, 1996). The changes in saturated bulk modulus after fluid substitution for both models are computed by subtracting the oil-saturated bulk modulus from brine-saturated bulk modulus (Figure 3.3b and c). In Figure 3.3b and c, the unconsolidated model shows greater changes in saturated bulk modulus with an average of 4 GPa than changes in the consolidated model with an average of 1.9 GPa, since again soft rock is more sensitive to changes in fluid saturation. The highest porosity region circled in Figure 3.3a shows the maximum change in saturated bulk modulus for the consolidated model (Figure 3.3c) but not for the unconsolidated model (Figure 3.3b). This is because in the consolidated model, bulk modulus has greater sensitivity to changes in pore fluids at higher porosities, but the unconsolidated model doesn't show consistent trends (Figure 3.2).

Elastic moduli computed from the above reservoir models are utilized in the seismic modeling. Synthetic seismograms are computed using the ray-Born algorithm to model the time-lapse seismic image of the reservoir (Beydoun and Mendes, 1989; Gibson, Jr. et al., 1993). This method was developed to estimate the wave fields scattered by the small perturbation in properties of an elastic medium. In our seismic models, we simulated zero offset sources and receivers with 20 m spacing. Thus there are 101 by 101 sources and receivers covering the reservoir. After computing the synthetic seismograms, a conventional phase-shift migration is applied.

Figure 3.4b and c show amplitude changes from the consolidated and unconsolidated models, respectively. These results are quite consistent with the bulk modulus changes in Figure 3.3. The consolidated model (Figure 3.4c) shows a stronger correlation with porosity (Figure 3.4a) than the unconsolidated model (Figure 3.4b). The average amplitude changes for the unconsolidated model is about 18%, which is three

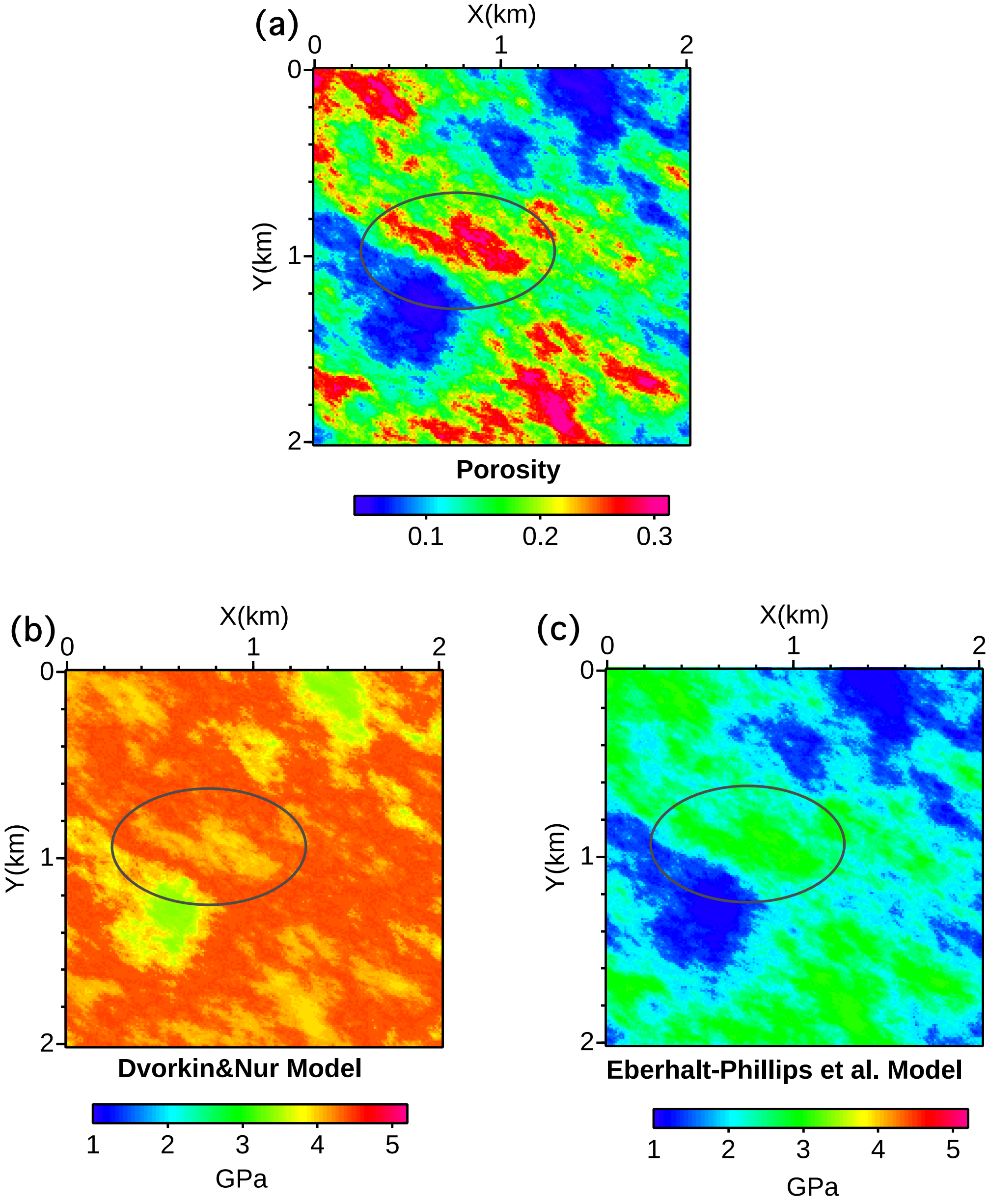

Fig. 3.3. (a) Porosity model is created by sequential Gaussian simulation. (b) Changes in saturated bulk modulus by fluid substitution from oil to brine, based on the unconsolidated model (c) Changes in saturated bulk modulus by fluid substitution from oil to brine based on consolidated model.

times larger than the consolidated model.

3.5 Conclusion

In this chapter, we analyzed the sensitivity of effective bulk modulus to changes in fluid saturation for different reservoir models. The consolidated reservoir model shows that high porosity shows high sensitivity of bulk modulus to changes in pore fluids, but the unconsolidated reservoir model shows little relation between porosity and sensitivity of bulk modulus to changes in pore fluids. Thus we should be more cautious when we try to relate 4D seismic response and porosity for the unconsolidated sand reservoir.

Overall 4D seismic responses are larger for the unconsolidated reservoir model than for the consolidated model, since soft rock is more sensitive to changes in fluid saturation.

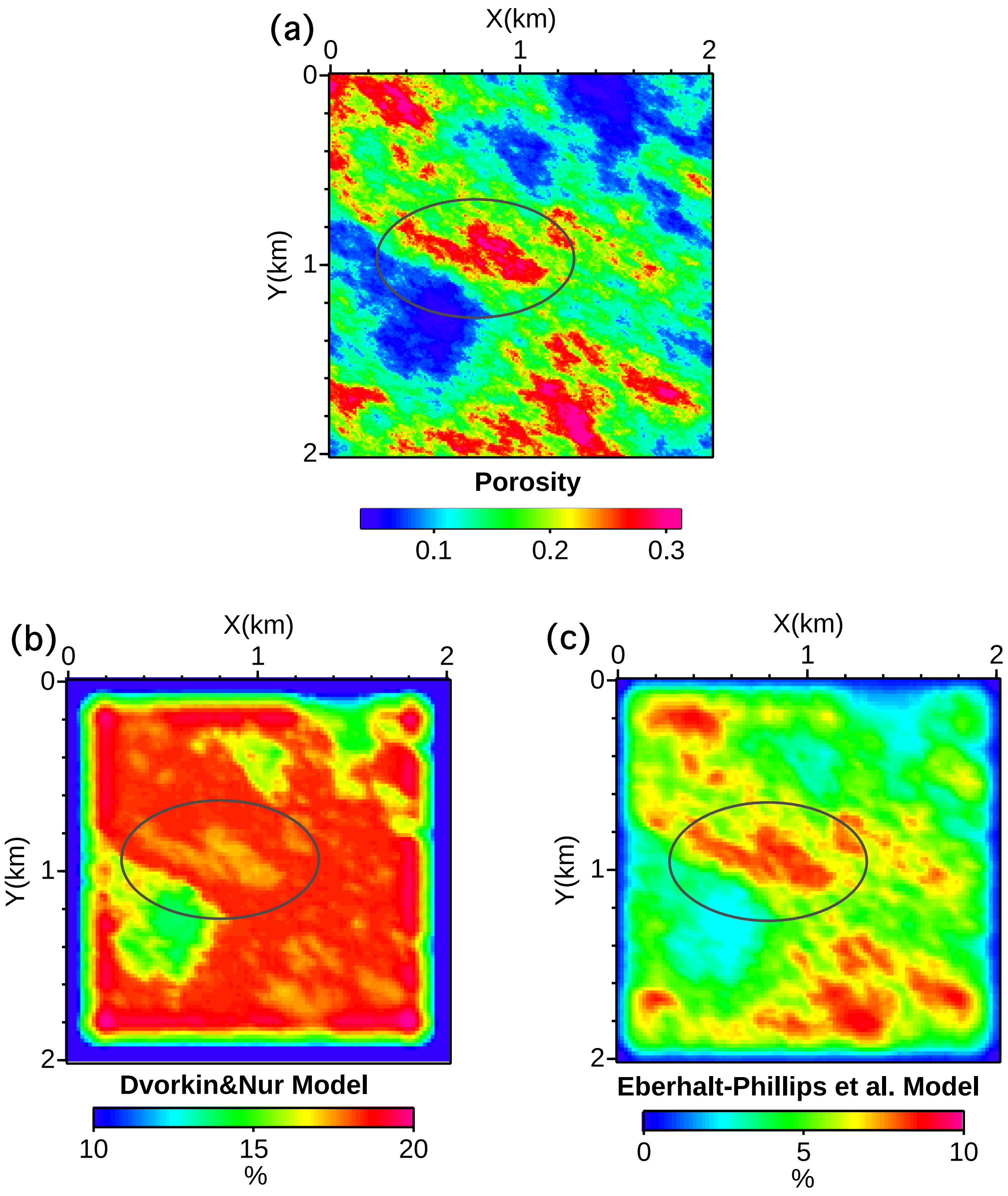

Fig. 3.4. (a) Porosity model is created by sequential Gaussian simulation. (b) Amplitude changes by fluid substitution from oil to brine based on unconsolidated model (c) Amplitude changes by fluid substitution from oil to brine based on consolidated model.

CHAPTER IV

UNCERTAINTY ANALYSIS IN TIME-LAPSE SEISMIC MODELING

4.1 Introduction

Time-lapse seismic monitoring repeats 3D seismic surveys in a particular location to estimate the changes in reservoir properties during production. The general goal is often to map the changes in reservoir fluid or pore pressure to locate bypassed oil in selecting infill drilling locations. However, 4D seismic images depend on many reservoir properties such as the elastic moduli of rock, fluid properties, and porosity, although most of these can only be measured from well logs or core measurements. Thus, there is significant, poorly constrained, spatial variability in property values between wells, and this causes uncertainties in the final 4D seismic image. Previous work has measured these uncertainties in several ways. For example, Lankston (1998) computed the possible range of reflection coefficient change using the Monte Carlo simulation method. He defined the range of each reservoir parameter and determined the value for each parameter randomly from related equations. The parameters he tested are oil gravity, GOR, water saturation, and porosity. Lumley and Behrens (1998) showed examples of different 4D seismic images with multiple realizations of rock properties. In this chapter, we extended these results to quantify directly the uncertainties in 4D seismic images associated with permeability, the major property that controls fluid flow, and the dry bulk modulus of a reservoir using stochastic modeling.

To do so, we generated 27 equiprobable realizations of permeability based on one porosity model using cloud transforms and sequential Gaussian simulation (SGS) methods (Aly et al., 1999). Then we applied a streamline fluid-flow simulator for the 27 permeability models, providing the fluid saturations and pressure distributions. Based on these results, we designed a rock-physics model and computed 2D synthetic seismograms for the 3D flat reservoir model using a ray-Born technique (Beydoun and Mendes, 1989; Gibson, Jr. et al., 1993). Finally, we generated 27 realizations of dry bulk modulus and then computed the synthetic seismogram to estimate the uncertainties in time-lapse seismic amplitude.

4.2 Analysis of permeability uncertainties

4.2.1 Permeability realizations

Many laboratory measurements show that the permeability-porosity relationship is nearly a log-linear trend, although with much scatter (Nelson, 1994) (Figure 4.1). The slope, intercept, and degree of scatter in Figure 4.1 depend on grain size, sorting, diagenetic history, and compaction history (Nelson, 1994; Berg, 1970). We applied cloud transforms to generate multiple realizations of a permeability model based on one reference porosity model. The cloud transform utilizes a probability-field simulation to estimate unknown reservoir property based on the known property (Srivastava, 1992; Aly et al., 1999). Our porosity model was generated using sequential Gaussian simulation. (Figure 4.2). Two horizontal variogram models with ranges of 600 m and 300 m, respectively, in orthogonal directions are applied to the sequential Gaussian simulation. The principal axes are rotated to a NE-SW direction to simulate the effects of statistical anisotropy. Porosity ranges from 0.15 to 0.33, with mean value of 0.23. The geometry of the model is 2000 x 2000 x 10 m, and it is discretized with 10 x 10 x 10 m blocks. It is a horizontally flat reservoir model. The depth of the reservoir model is 2 km. The 27 realizations of permeability models are generated using

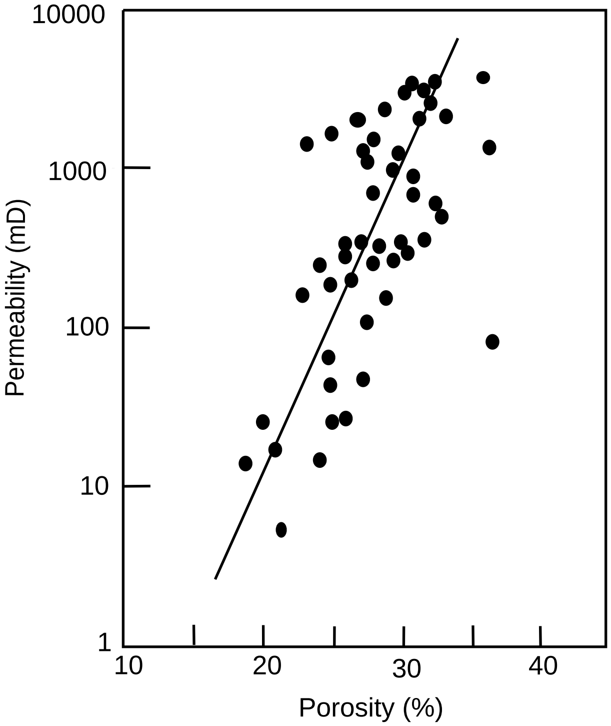

Fig. 4.1. Permeability versus porosity from core measurements from different oil fields (Timur, 1968)

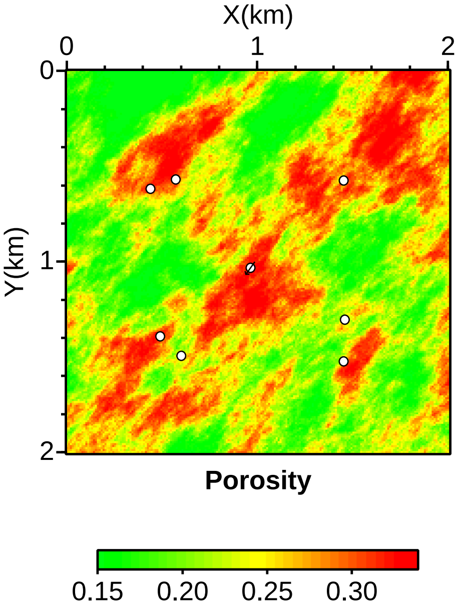

Fig. 4.2. A porosity map is generated using sequential Gaussian simulation. Two horizontal variogram models with ranges of 600 m and 300 m in orthogonal directions, respectively, are applied, and the principal axes are rotated to a NE-SW direction to simulate the anisotropy effects. White dots represent the injection well at the center and the production wells at four corners.

the cloud transform (Srivastava, 1992; Aly et al., 1999). The permeability-porosity model used in the cloud transform is illustrated in Figure 4.3, which shows a sample realization of permeability values as a function of porosity. The log-linear equation used for this model is

$$\log \kappa \;=\; 16.865\phi - 2.693, \tag{4.1}$$

where κ and ϕ are permeability and porosity, respectively. The coefficients in this equation are typical values for the poorly consolidated and high porosity sandstones in the Gulf of Mexico (Timur, 1968). Some examples of unconditional cumulative distribution functions (CDF) used for the unconditional probability field in the cloud transform are shown in Figure 4.4 (see details in chapter 2.5). These CDF models have the same variogram models and anisotropy parameters used in the porosity

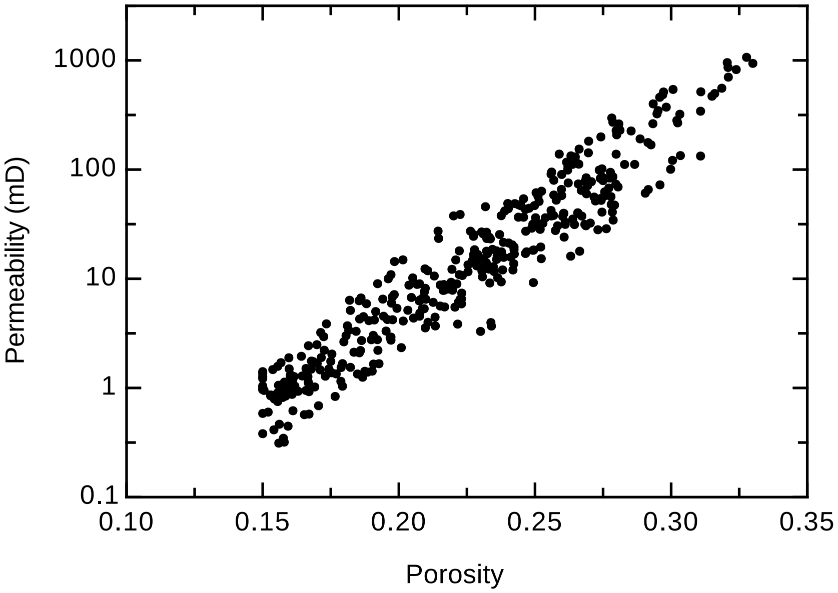

Fig. 4.3. Cross plot of permeability versus porosity used for cloud transform.

map in Figure 4.2. The permeability realizations in Figure 4.5 are equally probable models, even though they do not have the same permeability values. Permeability ranges from 0.1 to 4000 mD, with a mean value of 150 mD.

4.2.2 Streamline simulation for fluid flow

For the fluid-flow simulation, we used a streamline simulator, which provides very rapid modeling of large-scale, 3D reservoirs (King and Datta-Gupta, 1998). This method is an approximate solution analogous to ray theory in wave propagation, since the transport equation can be expressed in the form of the eikonal equation (Vasco et al., 1999). The reservoir model is assumed to be initially saturated with 80% light oil and 20% brine. Brine was injected at the center of the model, and the 7 production wells located around the injection well are marked with dots in Figs. 4.6 and 4.7(b). Water flooding was simulated for 9-years for each of the 27 permeability models using the streamline flow simulator. The injection rate was constant at 800 STB/day, and

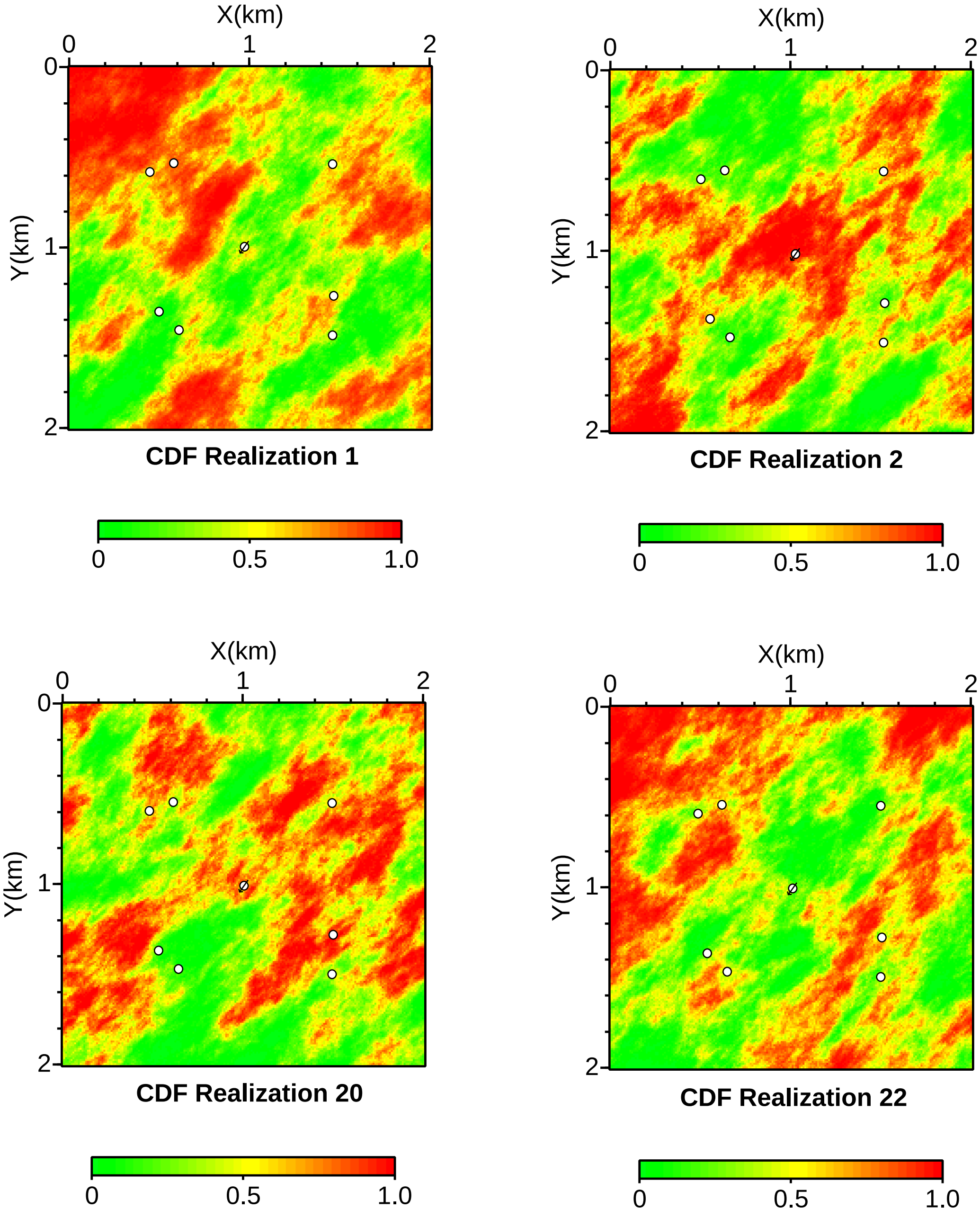

Fig. 4.4. Examples of realizations of cumulative density functions using sequential Gaussian simulation. The same parameters for variogram models and anisotropy effects are applied from porosity model. White dots represent the injection well at the center and the production wells at four corners.

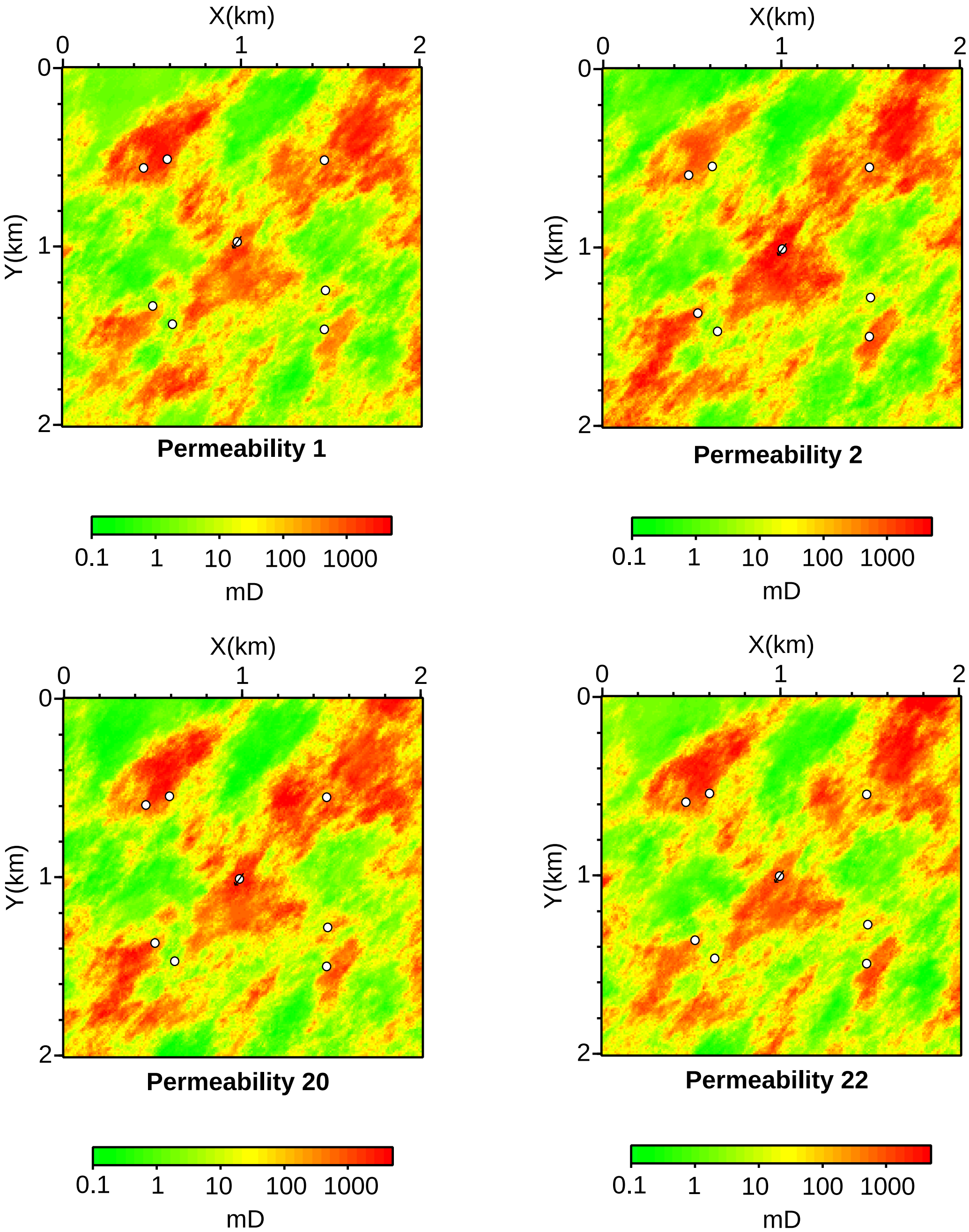

Fig. 4.5. Examples of permeability realizations using cloud transform. White dots represent the injection well at the center and the production wells at four corners.

production wells were pressure-constrained to 3000 psi.

Fluid simulation results are shown in Figure 4.6. Permeability was the only different parameter in all 27 models. Water breakthrough occurred at the upper-left production wells only for model 1 and 22 in Figure 4.6a and d. Maximum pore pressures for permeability model 2 and 22 are also different, 26 and 31 MPa, respectively, because we simulated a constant injection rate rather than constant pressure at the injection well (Figure 4.6b and d). The mean and standard deviation of brine saturation and effective pressure from the 27 fluid-flow simulations are shown in Figure 4.7. The brine-swept region in Figure 4.7a shows a NE-SW trend since the high porosity region is aligned in this direction. The high variance of brine saturation occurs at the brine front, which is the boundary between brine and oil, but the region close to the injection well shows approximately zero variance. Thus, we can expect a high uncertainty of 4D response around the brine front region (Figure 4.7b). The average minimum effective pressure is about 17 MPa at the center of the reservoir in Figure 4.7c. The variance of effective pressure in Figure 4.7d is maximum at the injection well because the constant injection rate produces different pore pressures in the injection region depending on the permeability.

4.2.3 Rock-physics modeling

In addition to these 27 results of the fluid-flow simulations, we also generated several realizations of important rock properties. The Gassmann equation then allowed us to consider the resulting effects of fluids on the elastic property of the reservoir (Gassmann, 1951). The dry bulk and shear moduli were computed, based on empirical relations predicting elastic properties of consolidated sandstone formations (Eberhart-Phillips et al., 1989). The fluid properties are also computed from empirical equations (Batzle and Wang, 1992).

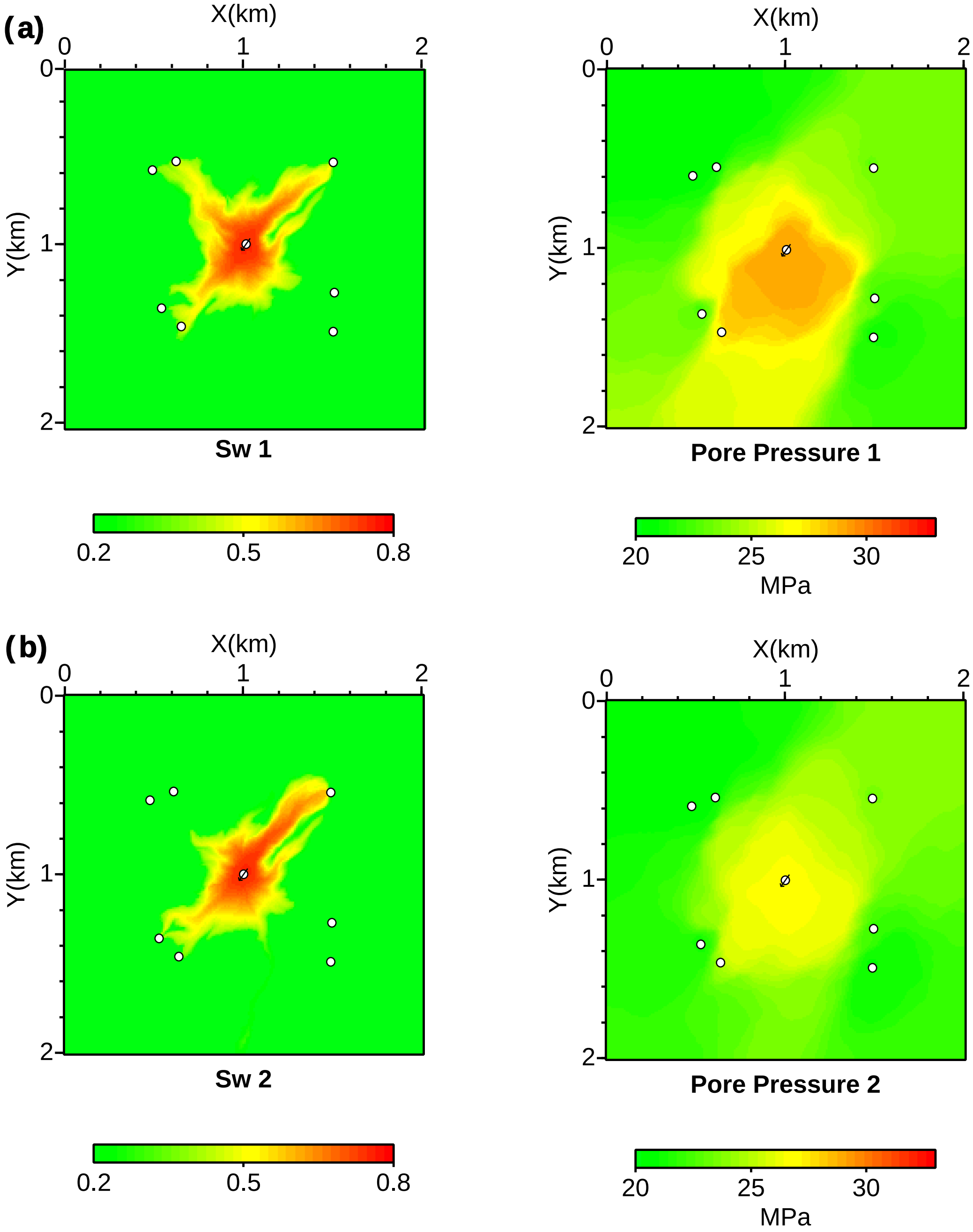

Fig. 4.6. Examples of water saturation and pore pressure after 9 year water flooding for permeability realization (a) 1,(b) 2,(c) 20, and (d) 22. White dots represent the injection well at the center and the production wells at four corners.

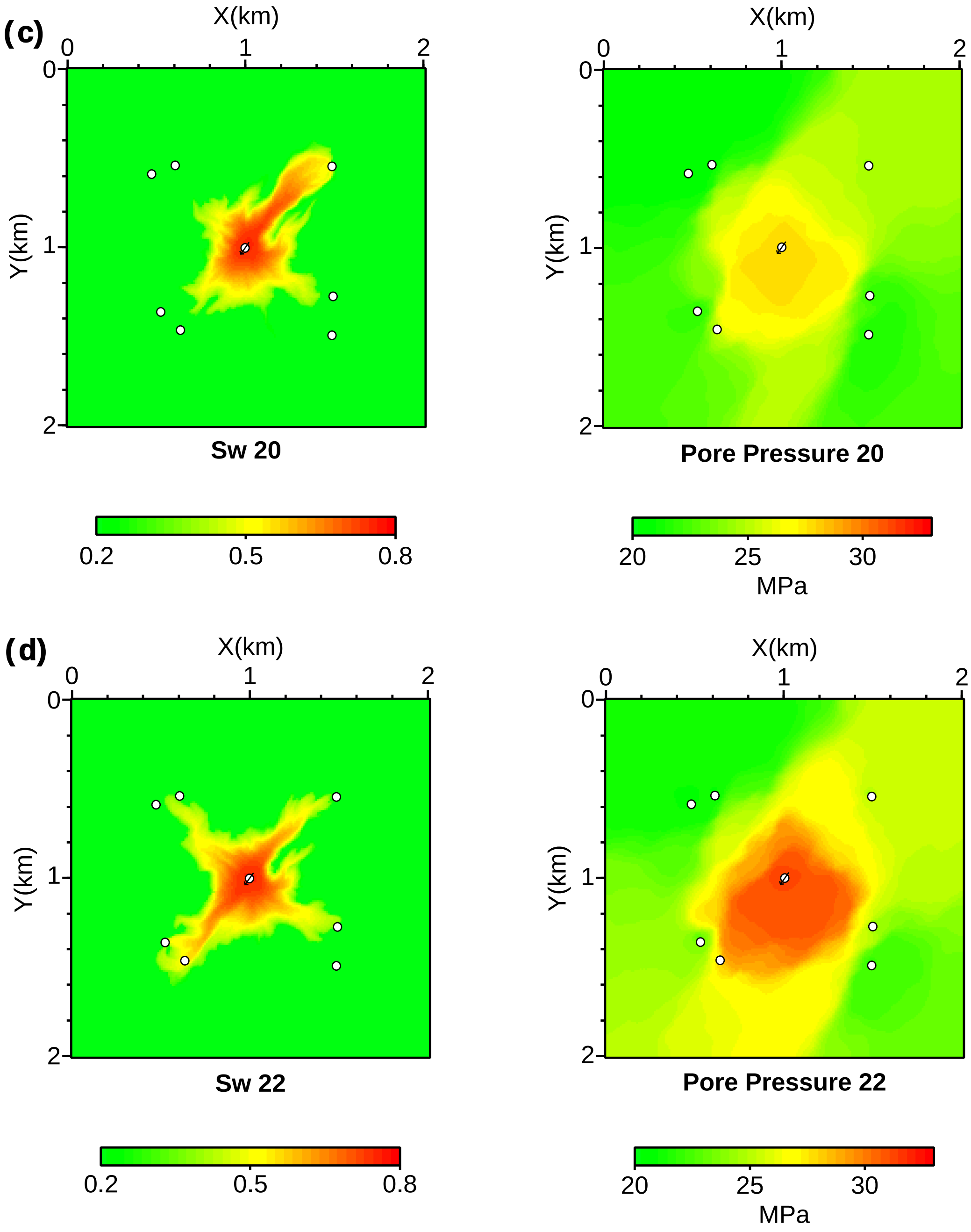
(c)
X(km)
0
1
2
Y(km)
0
1
2
Sw 20
0.2
0.5
0.8
X(km)
0
1
2
Y(km)
0
1
2
Pore Pressure 20
20
25
30
MPa
(d)
X(km)
0
1
2
Y(km)
0
1
2
Sw 22
0.2
0.5
0.8
X(km)
0
1
2
Y(km)
0
1
2
Pore Pressure 22
20
25
30
MPa

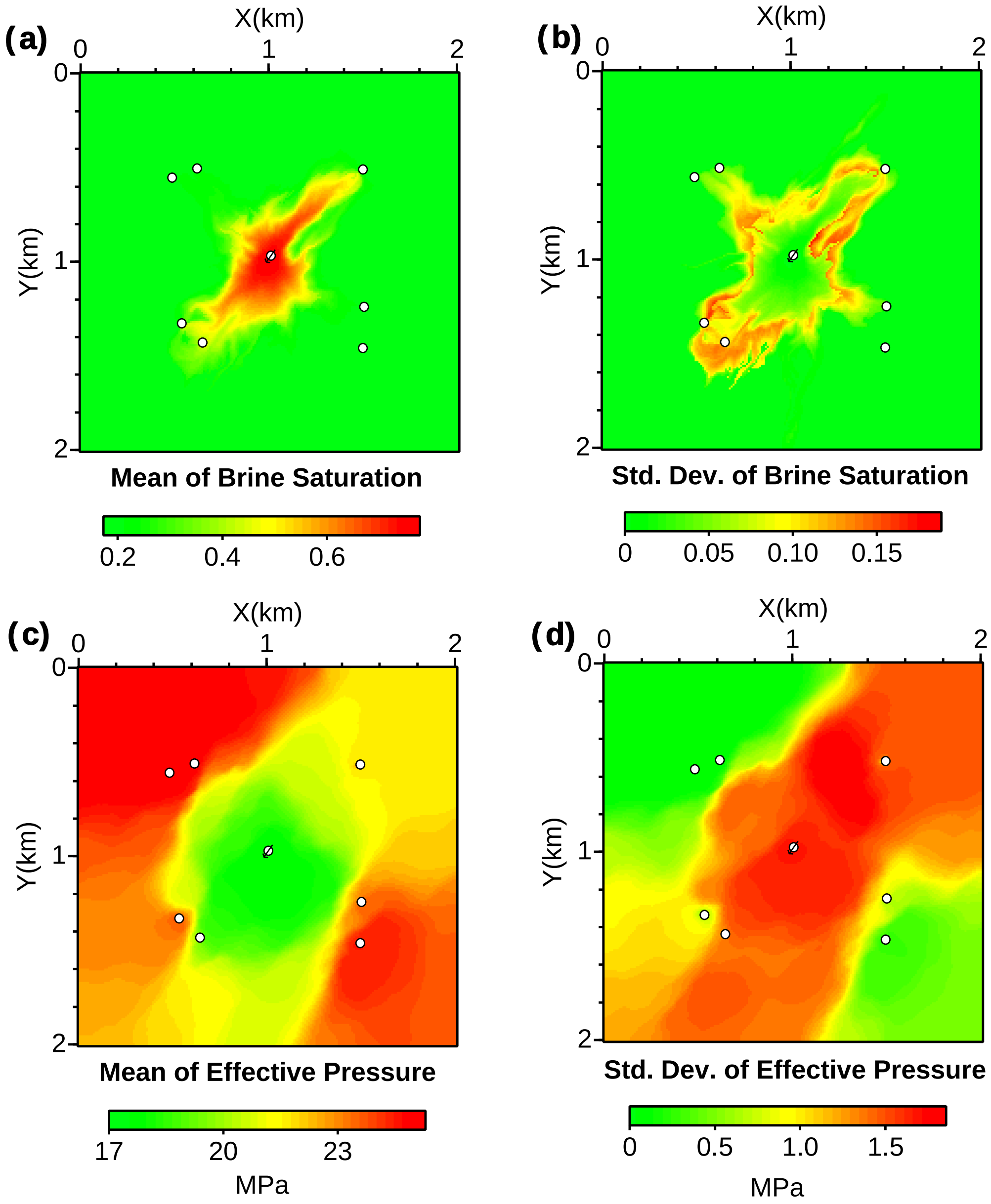

Fig. 4.7. (a)Mean and (b)standard deviation of brine saturation, and (c)mean and (d)standard deviation of effective pressure for 27 fluid flow simulations. White dots represent the injection well at the center and the production wells at four corners.

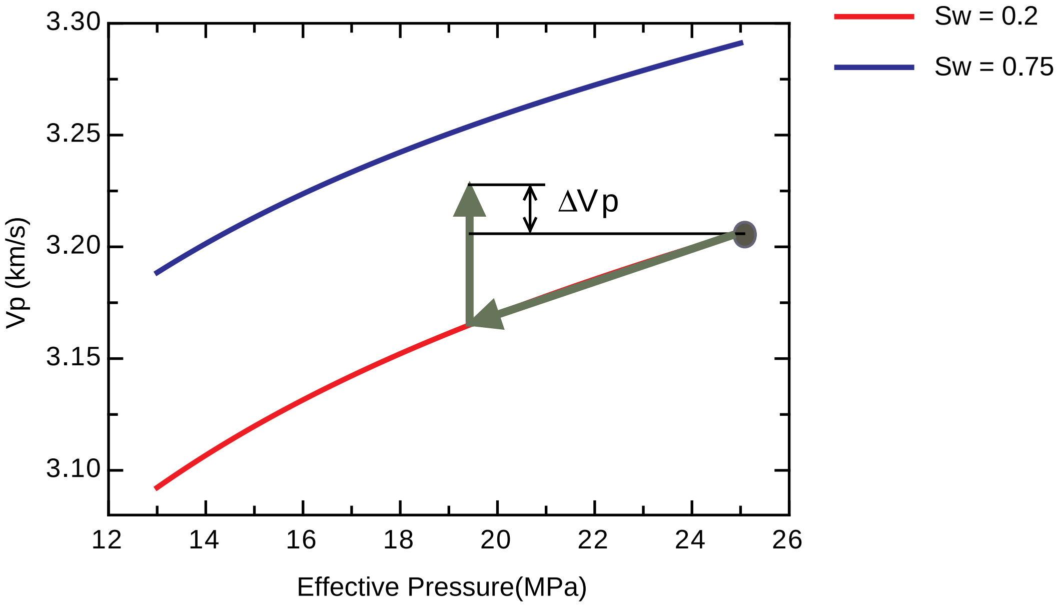

Fig. 4.8. Velocity as a function of effective pressure at different water saturations. Red and blue curves show $S_w = 0.2$ and 0.75, respectively. Porosity is assumed to be 20%.

In the water-flood simulation, the effective pressure decreases because of the brine injection, and fluid modulus and fluid density increase because of the substitution of brine for light oil. To illustrate the expected behavior, the P-wave velocity was computed as a function of effective pressure for 20% and 75% brine-saturation cases in Figure 4.8. Porosity is assumed to be 0.2. The arrows in Figure 4.8 show one possible scenario of water flooding. The initial V_p at 25 MPa and 20% brine saturation begins to decrease as effective pressure decreases, but it also increases as brine replaces oil. Both processes are combined, and either effect might be greater than the other one depending on the reservoir location and the actual pressure and saturation conditions. The ΔV_p in Figure 4.8 represents the final velocity change after water flooding. Thus, if the pressure effect is dominant in some region, the velocity decreases after brine injection, and if the saturation effect is dominant, the velocity increases after water brine injection.

4.2.4 Seismic modeling

The elastic properties of the reservoir model computed in the previous section provide the basis for seismic modeling using a ray-Born technique to model the time-lapse seismic image of the reservoir. This method estimates the wave fields scattered by small perturbations in properties of an elastic medium (Beydoun and Mendes, 1989; Gibson, Jr. et al., 1993).

Our model includes a horizontal reservoir layer with a homogeneous overburden of velocity and density ($V_p = 2.11$ km/s, $V_s = 1.05$ km/s, density $= 1.8$ g/cm^3). It is located at the depth of 2 km. The synthetic seismogram were computed along a 2D seismic profile over the reservoir at $Y = 0.8$ km. The seismic models simulated a zero offset array with 20 m source/receiver spacing, and we applied a phase shift migration to these data. Example synthetic seismograms before and after water flooding and changes in amplitudes are plotted in Figure 4.9. The same amplitude normalization factor is applied to plot in Figure 4.9a and b so that amplitudes can be directly compared, but Figure 4.9c is normalized by a different scale. It is hard to see the difference in amplitudes in Figure 4.9a and b. However, by subtracting one image from the other, we can see the changes in seismic amplitude in Figure 4.9c. To determine the amplitude change after water flooding, we picked the amplitude at 1.89 s, which is the time for minimum amplitude in the before- and after-traces (Figure 4.9). The polarities of seismic traces in Figure 4.9c change from positive to negative and again to positive. This is caused by the competing effects of pressure and fluid substitution on seismic impedance explained in the previous section.

The average and standard deviation of amplitude changes for all 27 permeability models are shown in Figure 4.10. In our particular reservoir models, the negative amplitude changes indicate a seismic impedance increase. This occurs when satura-

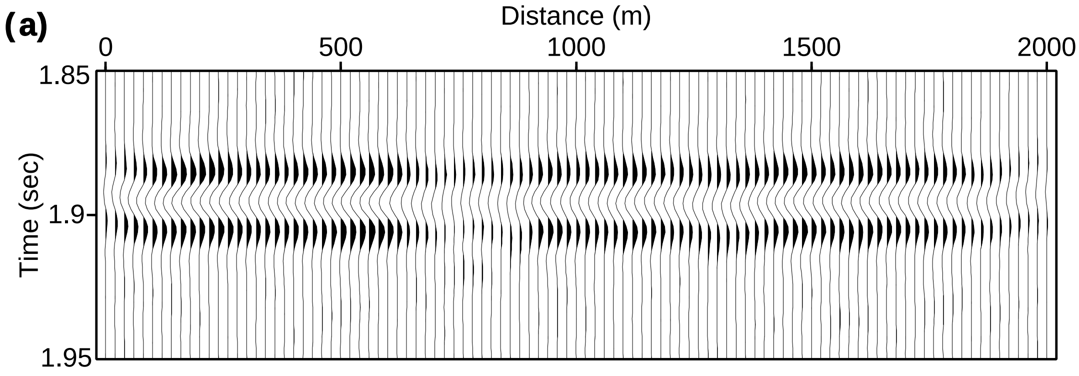

before brine injection

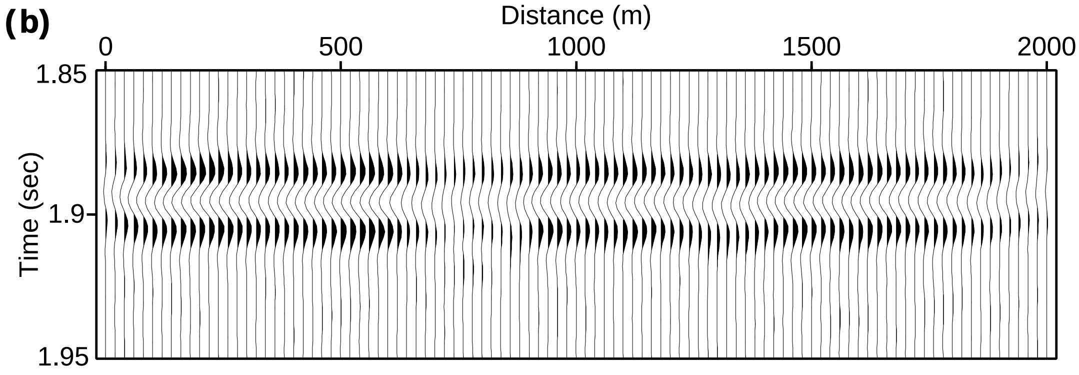

after brine injection

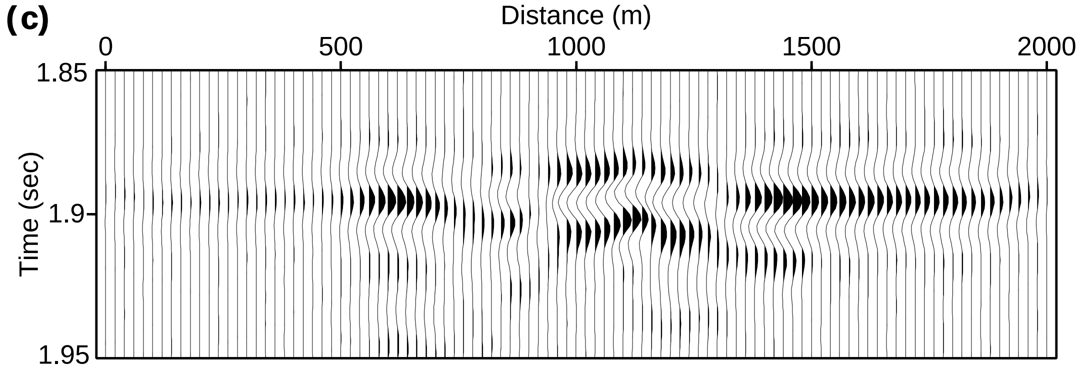

time-lapse amplitude

Fig. 4.9. Synthetic seismograms of (a) before, and (b) after brine injection. (c) Amplitude changes are computed by subtraction of traces (b) from traces (a). The same amplitude-normalization factor is applied to plot (a) before-traces, (b) after-traces, and (c) difference traces are applied to different amplitude scale.

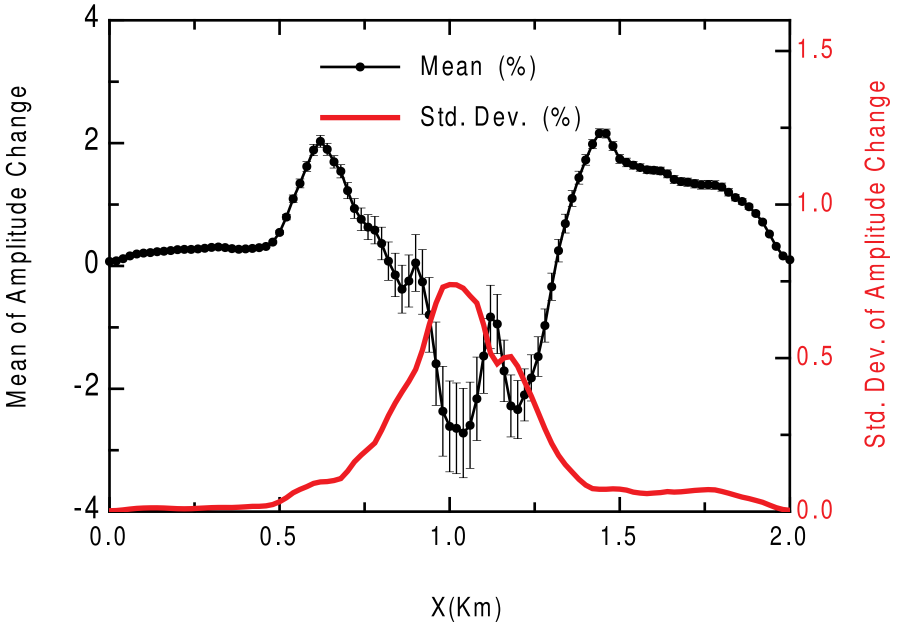

Fig. 4.10. Black dots and error bars represent the average amplitude changes and standard deviations, respectively, computed from 27 permeability realizations. The red curve is the standard deviation with the scale on the right axis.

tion effects are dominant, and positive amplitude changes mean the pressure effects are dominant (Figure 4.10). Fluid simulation results for brine saturation and pressure are shown in Figure 4.6 and 4.7. The average amplitude changes (black dots in Figure 4.10) are negative at the center region, and positive outside of brine-saturated region where pressure effects are dominant. For $X \geq 1.4$ km in Figure 4.10, the amplitude changes are constantly positive since there are only pressure effects in this region. The red curve and error bars in Figure 4.10 represent the standard deviations in seismic amplitude change from the 27 models, which therefore measure the uncertainty in amplitude change. The maximum uncertainties in amplitude change occur around $X = 0.75$ and 1.25 km, which are the edges of the brine-saturated region (Figure 4.10). This is because the uncertainties in brine saturation are maximum at the edge of the brine saturated region and the uncertainties in pore pressure are relatively constant over the saturated region as shown in Figure 4.7.

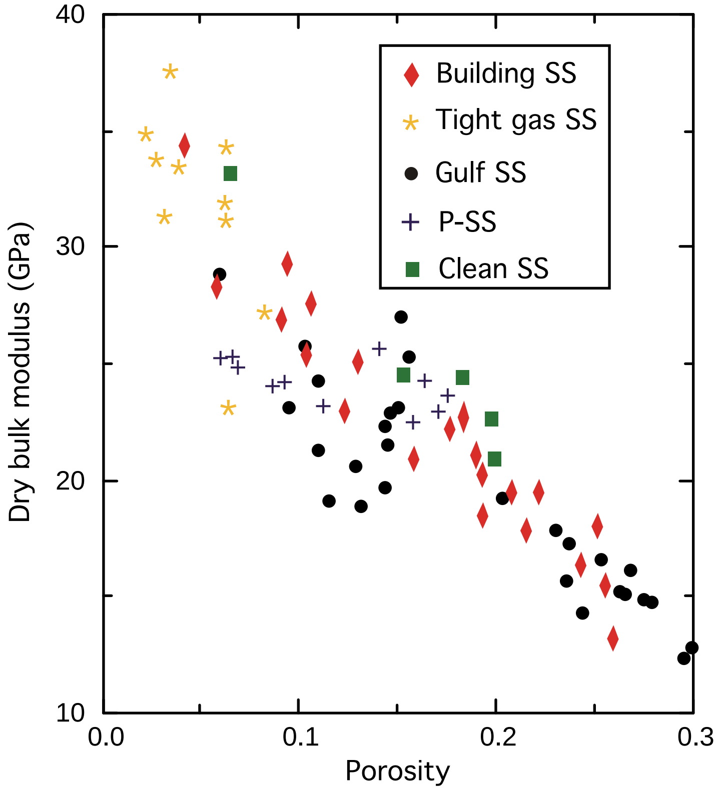

Fig. 4.11. Cross plot of dry bulk modulus versus porosity computed from P and S wave velocities of water saturated sandstones (Han et al., 1986).

4.3 Analysis of dry bulk modulus uncertainties

Relations between the dry bulk modulus and porosity in sandstone typically display large scatter, much like the log permeability-porosity data (Han et al., 1986) (Figure 4.11). We generated model results for dry bulk modulus versus porosity, using empirical relations for consolidated sandstone formations (Eberhart-Phillips et al., 1989) (Figure 4.12). We applied the cloud transform technique to generate 27 dry-bulk-modulus models based on the same cumulative distribution functions used in the permeability models. Figure 4.13 shows examples of realizations of dry bulk modulus fields. The average water saturation and pore pressure results from the fluid simulations obtained during permeability stochastic modeling are applied to compute the

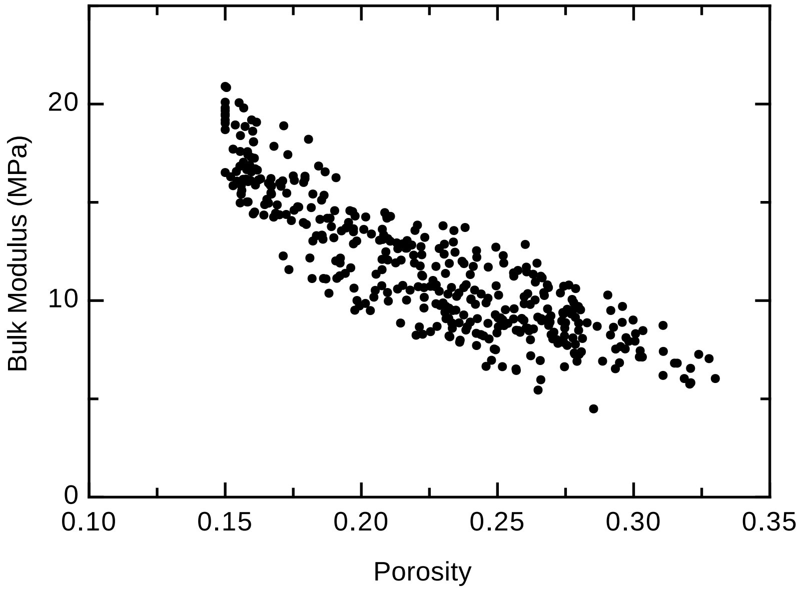

Fig. 4.12. Cross plot of dry bulk modulus versus porosity of sandstone based on equation 2.5.

Gassmann equation.

We computed the synthetic seismograms along the $Y = 0.8$ km line for before and after water flooding based on 27 dry bulk modulus models. This is the same geometry as was used for the permeability tests, so results can be compared directly. The average amplitude changes are almost same as those in Figure 4.10, but the uncertainties in amplitude change are maximum at the center of the model ($X =$ 1 km) (Figure 4.14). The red curve and error bars in Figure 4.14 represent the uncertainties in amplitude change associated with uncertainties in dry bulk modulus. The red curve in Figure 4.14 is well correlated with water saturation (Figure 4.7a) even though the same brine saturation is applied to compute the Gassmann equation for the 27 dry-bulk-modulus models. For example, the standard deviations in the pressure-change-only region ($X > 1.4$ km) are less than 0.1%, but those in the water-saturated region (0.6 km$< X <$1.4 km) are maximum of 0.7% (Figure 4.14). This is because the sensitivity of saturated bulk modulus in fluid substitution strongly

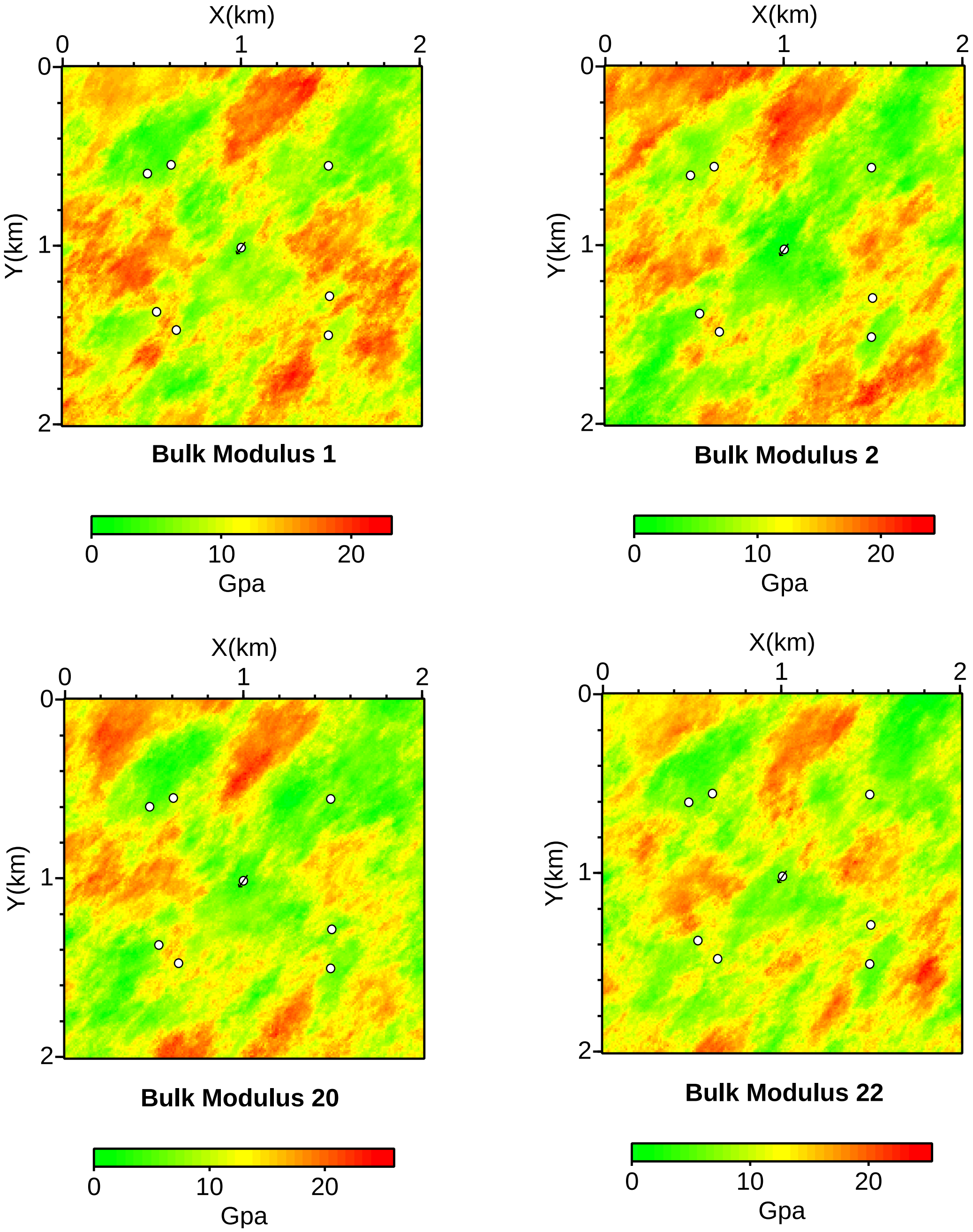

Fig. 4.13. Examples of dry-bulk-modulus realizations using the cloud transform. White dots represent the injection well at the center and the production wells at four corners.

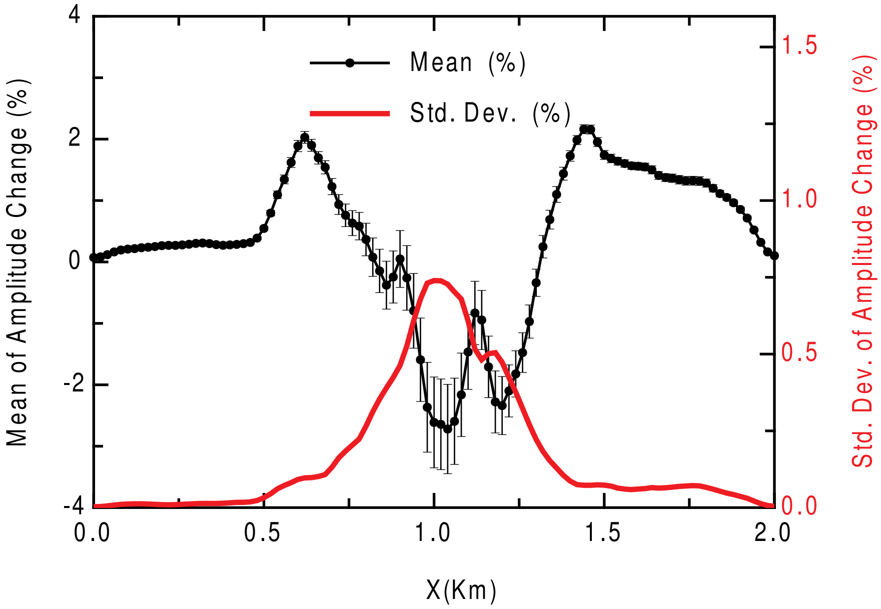

Fig. 4.14. Black dots and error bars represent the average amplitude changes and standard deviations, respectively, computed from 27 dry bulk modulus realizations. The red curve is the standard deviation with the scale on the right axis.

depends on the dry bulk modulus (Lumley et al., 1997). For example, a rock with low dry bulk modulus shows large change in saturated bulk modulus but the rock with high dry bulk modulus shows relatively small changes in saturated bulk modulus (see Figure 3.1 and 3.2 in chapter III). Thus, in Figure 4.14, different dry-bulk-modulus models cause different amounts of change in saturated bulk modulus, which means large uncertainty in amplitude changes at the water-saturated center region. However, the different pressure changes for different dry-bulk-modulus models cause almost-same amount of change in the saturated bulk modulus ($X > 1.4$ km).

4.4 Conclusions

We have applied stochastic modeling methods that quantify uncertainty in a time-lapse seismic amplitude changes caused by the uncertainties in permeability and dry bulk modulus.

The uncertainty associated with poorly constrained permeability values is greatest near the edges of the water flood, where saturation is changing most rapidly. The variability in time-lapse signal is much less in the center of the model, which is always almost completely water flooded, and in the distal regions, which are less affected by the flooding. In contrast, the uncertainty in dry bulk modulus causes more variability in seismic signals near the water injection well, which is where the saturation change is consistently large. At the same time, the uncertainty caused by the bulk modulus is less than that associated with the permeability field, suggesting that accurate models of the drained modulus are less important for accurate interpretation and modeling of time-lapse seismic data.

CHAPTER V

TIME-LAPSE SEISMIC MONITORING OF CO_2 SEQUESTRATION IN HYDROCARBON RESERVOIRS: MODEL STUDY

5.1 Introduction

Emissions of CO_2 , a greenhouse gas, from combustion of fossil fuels are about 27 billion tone per year worldwide (DOE, 1999). Many technologies have been developed to reduce CO_2 in the atmosphere, such as injecting CO_2 into deep coal seems, deep ocean, or geologic formations (Gale et al., 2001; Gentzis, 2000; Haugan and Drange, 1992). One of the promising solutions for this problem is to sequestrate CO_2 in underground rock formations (Beecy and Kuuskraa, 2001). For example, the first large-scale CO_2 sequestration project has been conducted at the Sleipner field in the northern North Sea since 1996 at annual rates of about 1 million tons CO_2 (Gale et al., 2001).

CO_2 can be accumulated in the subsurface in a gas, liquid, or supercritical fluid state, depending on the pressure and temperature in the aquifer. Also, it is possible for the accumulated CO_2 to migrate to other traps because of the heterogeneity of the rock formation. It is important to monitor the saturation of CO_2 and identify the phase of CO_2 during the injection process in order to manage the injection.

Time-lapse seismic surveys have been applied successfully to monitoring fluid changes in hydrocarbon reservoirs during oil production (e.g. Lumley et al., 1999; Jack, 1998). The elastic properties of reservoir formations are directly affected by the fluid changes, since the bulk density and the bulk modulus of rock change when the pore fluid is replaced. Although CO_2 sequestration itself is a relative new application, seismic experiments conducted during CO_2 flood operations designed to enhance hydrocarbon production from many reservoirs have shown clearly that CO_2 injection considerably changes the P- and S-wave velocities of the reservoir (Holtz et al., 2001; Wang et al., 1998; Hadlow, 1992). The seismic monitoring of Sleipner field also shows a large increase in reflectivity and a large traveltime-delay caused by CO_2 injection (Eiken et al., 2000).

Measurements of the physical properties such as compressibility and density of carbon dioxide suggest that different phases of CO_2 should have distinctly different effects on seismic wavefields reflected from formations in which the waste material is sequestered. This, together with the previous experiments for CO_2 injection, suggests that time-lapse seismic monitoring should be effective. Therefore the goal of this chapter is to utilize numerical modeling of both fluid simulation of carbon dioxide sequestration and seismic-wave propagation in a representative model of a sequestration site to quantify the difference in seismic reflections from different CO_2 phase cases that might be observed in realistic applications.

In this chapter, we compare the physical properties of different pore fluids and phases. Then, we outline the rock-physics model we use to quantify the expected changes in seismic velocities for different phases of CO_2 and the results of reservoir fluid-flow simulation for both CO_2 injection models. Finally, we present examples for a laterally heterogeneous, stochastic reservoir model to evaluate the feasibility of time-lapse seismic monitoring of CO_2 sequestration. The ray-Born method is applied to computation of the 3D synthetic seismograms (Beydoun and Mendes, 1989; Gibson, Jr. et al., 1993).

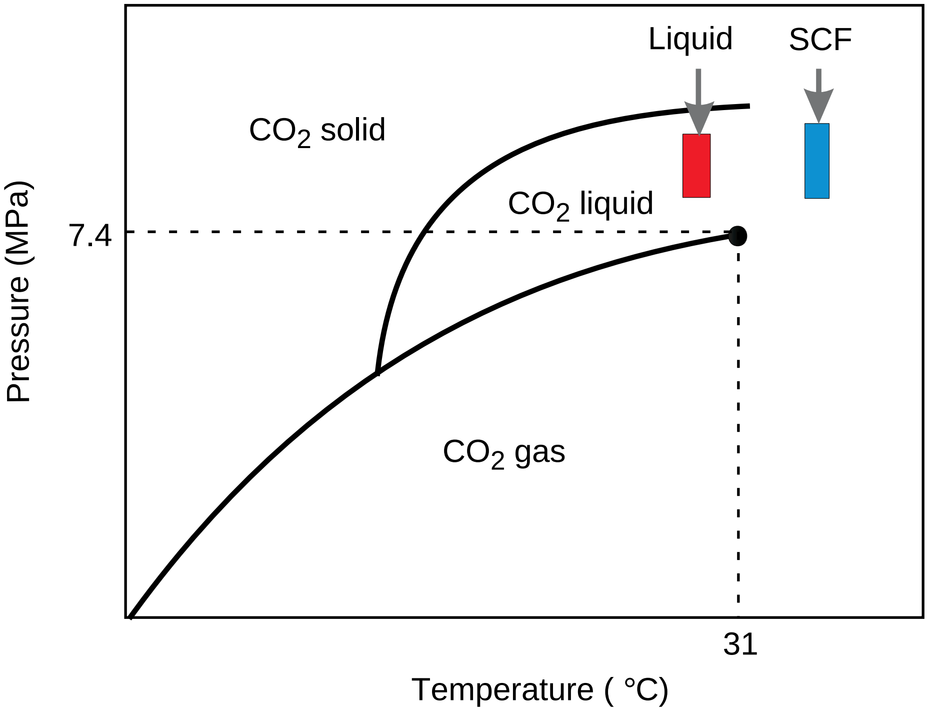

Fig. 5.1. CO_2 phase diagram. The critical temperature and critical pressure of CO_2 are 31°C, and 7.4 MPa, respectively. Red and blue bars represent the pressure ranges of liquid and SCF CO_2 in our reservoir simulations, respectively.

5.2 Fluid properties

Our model simulates the injection of CO_2 into a water-saturated reservoir. CO_2 can exist in three separate phases; gaseous CO_2 liquid CO_2 or supercritical fluid (SCF) CO_2 depending on pore pressures and temperatures in the reservoir. The critical temperature and critical pressure of CO_2 are 31°C and 7.4 MPa, respectively. Above the critical temperature and critical pressure, there is no distinction among solid, liquid, and gas, which is the state of the SCF (Figure 5.1). In this study, we tested two different reservoir models. The temperature of the first model is 27°C, which is below the critical temperature, and the second model is 77°C, which is above the critical temperature. The initial pore pressure for both models is 8 MPa, above the critical pressure, and it is increased up to 11.5 MPa for the liquid CO_2 model and

13.3 MPa for the SCF CO_2 model, based on fluid flow simulations (Figure 5.1). Thus the CO_2 phase of the first model is liquid and the second model is SCF. Figure 5.2 shows the density and velocity of liquid and SCF CO_2 versus pressure at temperature of 27°C and 77°C, respectively (Kennedy, 1954; Vargaftik, 1975). The density and velocity of water as a function of pressure and temperature in Figure 5.2 are computed based on empirical equations (Batzle and Wang, 1992). Since the properties of water vary only slightly over this temperature range, we show only the density and velocity at the lower temperature value in this figure.

In Figure 5.2, the density of liquid CO_2 at 12 MPa is 78% of the water density, but the velocity of liquid CO_2 is only 29% of the water value, which means that the compressibility of CO_2 is quite large compared to water. In contrast, the density and velocity of SCF CO_2 are 36% and 16% of water at 13 MPa. The velocity of liquid CO_2 increases with increasing pressure, but those of SCF CO_2 are only a weak function of pressure (Figure 5.2b). The velocities of both liquid and SCF CO_2 are still much lower than those of water and oil under a broad range of conditions. Thus, based on the velocity and density contrasts between water and the different phases of CO_2 in Figure 5.2, we can expect larger changes in seismic response after CO_2 injection for SCF CO_2 than for liquid CO_2 .

5.3 Reservoir modeling

Because the density and velocities in the various phases of carbon dioxide are very different from those of water, substitution of water in the pore space of a reservoir rock with CO_2 will likely be easily detectable. However, in complex, heterogeneous formations, it is possible that the effects of fluid changes could be obscured by other wave-propagation phenomena. Our numerical modeling tests are designed to test how

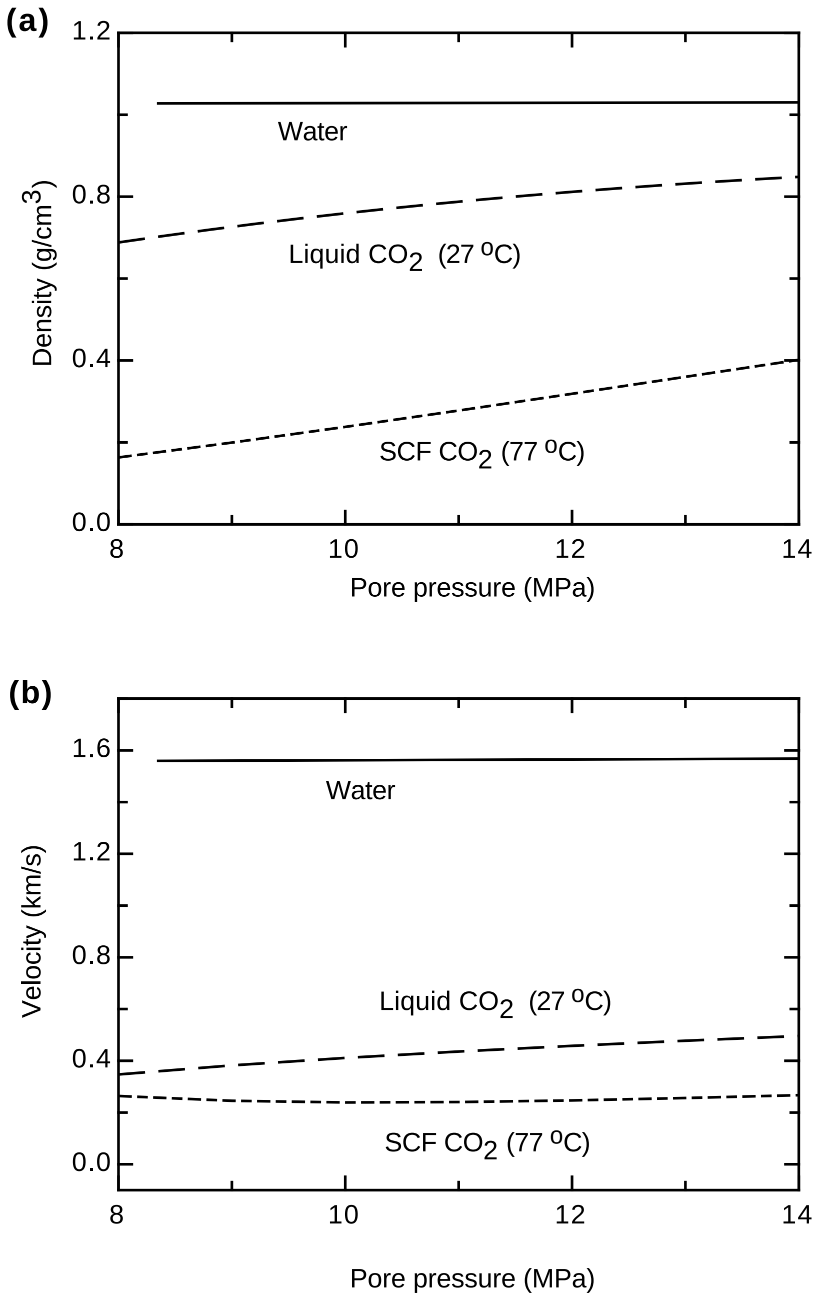

Fig. 5.2. (a) Densities and (b) velocities of water, liquid CO$_2$ at 27°C,and supercritical fluid CO$_2$ at 77°C as a function of pressure.

.

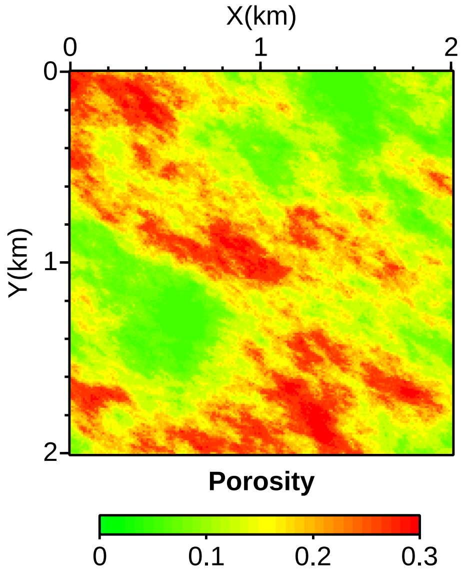

Fig. 5.3. Porosity map generated by sequential Gaussian simulation.

strong the effects of the fluid changes are likely to be.

5.3.1 Porosity and permeability

The conceptual earth model that we consider is based on a porosity map that was generated using sequential Gaussian simulation (Figure 5.3) (Deutsch and Journel, 1998). We applied two different semivariogram models in two orthogonal directions to simulate a spatially anisotropic distribution of porosity. The porosity range is from 5 to 30%. A cloud-transform technique was used to generate the permeability field (Srivastava, 1992; Aly et al., 1999). The cloud transform is one of probability field simulation to estimate an unknown reservoir property, based on the known property (Srivastava, 1992; Aly et al., 1999). Advantages of the cloud transform are that it honors the relationship between properties such as porosity/permeability and preserves the heterogeneity of the property such as scatters (Aly et al., 1999) (Figure 5.4).

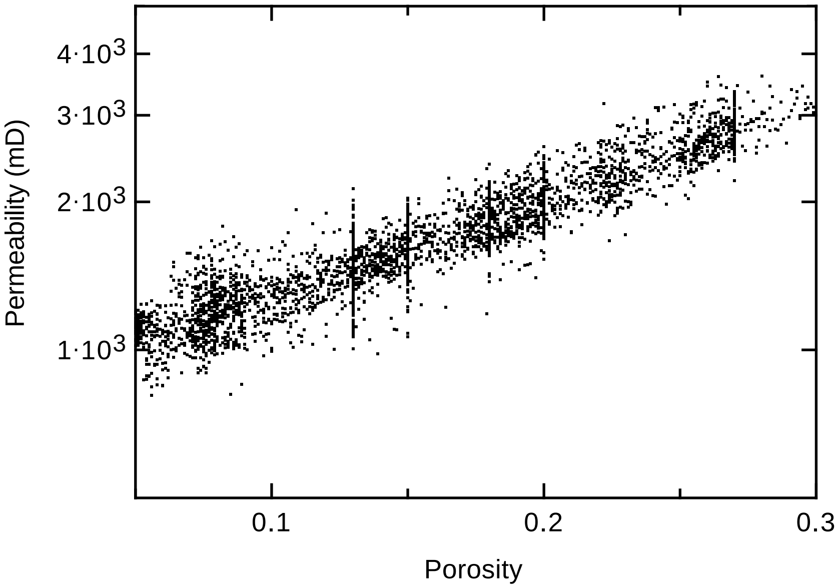

Fig. 5.4. Cross plot of permeability to porosity. This is the synthetic example based on the core measurements in the published data.

Therefore, the permeability values are spatially correlated with porosity, but there is no one specific value of permeability that is mapped to the porosity (Figure 5.5). The permeability model ranges from 700 to 3900 mD, which are relatively high values since we assumed the reservoir consists of unconsolidated sands. The reservoir depth is assumed to be 884 m, and the confining pressure for the formation was estimated from the hydrostatic pressure for this depth.

5.3.2 Fluid flow simulations

The movement of carbon dioxide in this model reservoir formation was performed using the ECLIPSE reservoir simulator that considers the chemical reactions in reservoir fluids at reservoir conditions but doesn't consider fluid-rock reactions. We considered two scenarios, one with liquid CO_2 and one with SCF CO_2 , in order to compare the effects of the two different states on the time-lapse seismic response. Reservoir temperatures for liquid CO_2 and SCF CO_2 models are 27°C and 77°C, respectively,

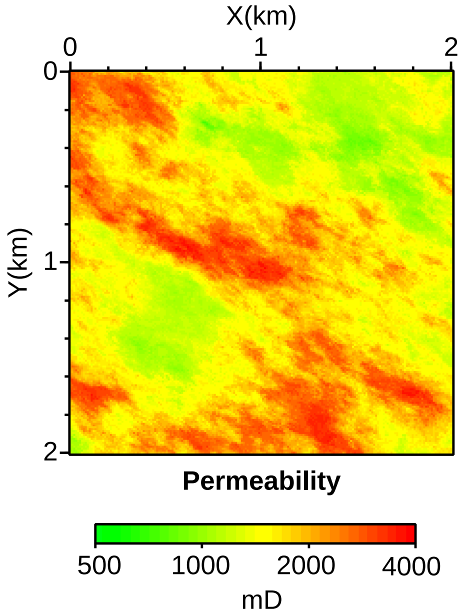

Fig. 5.5. Permeability generated by cloud transform based on porosity in Figure 5.3.

and these values are assumed to be constant during injection for both models. The reservoir model was also assumed to be 100% water-saturated initially, and the CO_2 was injected at the center. In the ECLIPSE simulation we chose the compositional model to consider the reaction among fluids. The reservoir model consists of one layer with 200 by 200 grid blocks. A grid block size is 10 m by 10 m. The saturation and pore pressure for liquid and SCF CO_2 are shown in Figure 5.6 for a time point of 180 and 90 days after the initiation of injection, respectively. The maximum pore pressure for SCF CO_2 is higher than for liquid CO_2 , even though the liquid CO_2 model has twice the injection time and both have the same injection rate (Figure 5.6b and d). This is because volumetric expansion of SCF CO_2 is larger than that of liquid CO_2 . The SCF CO_2 moves more rapidly through the formation, since the viscosity of SCF CO_2 is much lower than that of liquid CO_2 (Figure 5.6a and c). Thus, SCF CO_2 occupies a similar area of the model in only half of the injection period of liquid

CO_2 . The seismic modeling experiments will help to demonstrate whether or not we can distinguish seismically between these two cases in order to make better in situ condition inference.

5.3.3 Rock-physics modeling

Seismic simulations require a quantitative estimate of the effects of pore fluids on the elastic properties of a porous rock, which we obtain from the Gassmann (1951) equation (2.1). The fluid bulk modulus in the Gassmann equation is computed using Wood's (1955) average equation and the empirical equations (Kennedy, 1954; Vargaftik, 1975; Batzle and Wang, 1992). CO_2 saturation is computed from fluid simulation.

In our modeling, we assumed that the reservoir rock is unconsolidated sand, and we applied the modified contact theory to model the dry bulk and shear moduli as functions of pressure and porosity (Dvorkin and Nur, 1996) (Figure 5.7).

Another factor we considered in our modeling is heterogeneity of rock properties. Much published data shows that the relation between elastic moduli of porous rock and porosity displays tremendous scatter (e.g., Han et al., 1986). Thus, the cloud-transform technique is applied to simulate the scattered dry bulk and shear moduli as functions of porosity (Srivastava, 1992; Aly et al., 1999) (Figure 5.7).

Once we obtain the dry bulk modulus values, we can apply Gassmann's equation to any kind of pore fluids such as gas, CO_2 oil, or water. For example, Figure 5.8a shows P-wave velocities of unconsolidated sands as a function of CO_2 saturation at constant pressure. The velocity of liquid-CO_2 model decreases continuously as the CO_2 saturation increases. This trend is similar to that of the velocity changes in the oil-water reservoir. The velocities of the SCF CO_2 model drop rapidly at low CO_2 saturation and then start to increase slightly. This trend is similar to that of

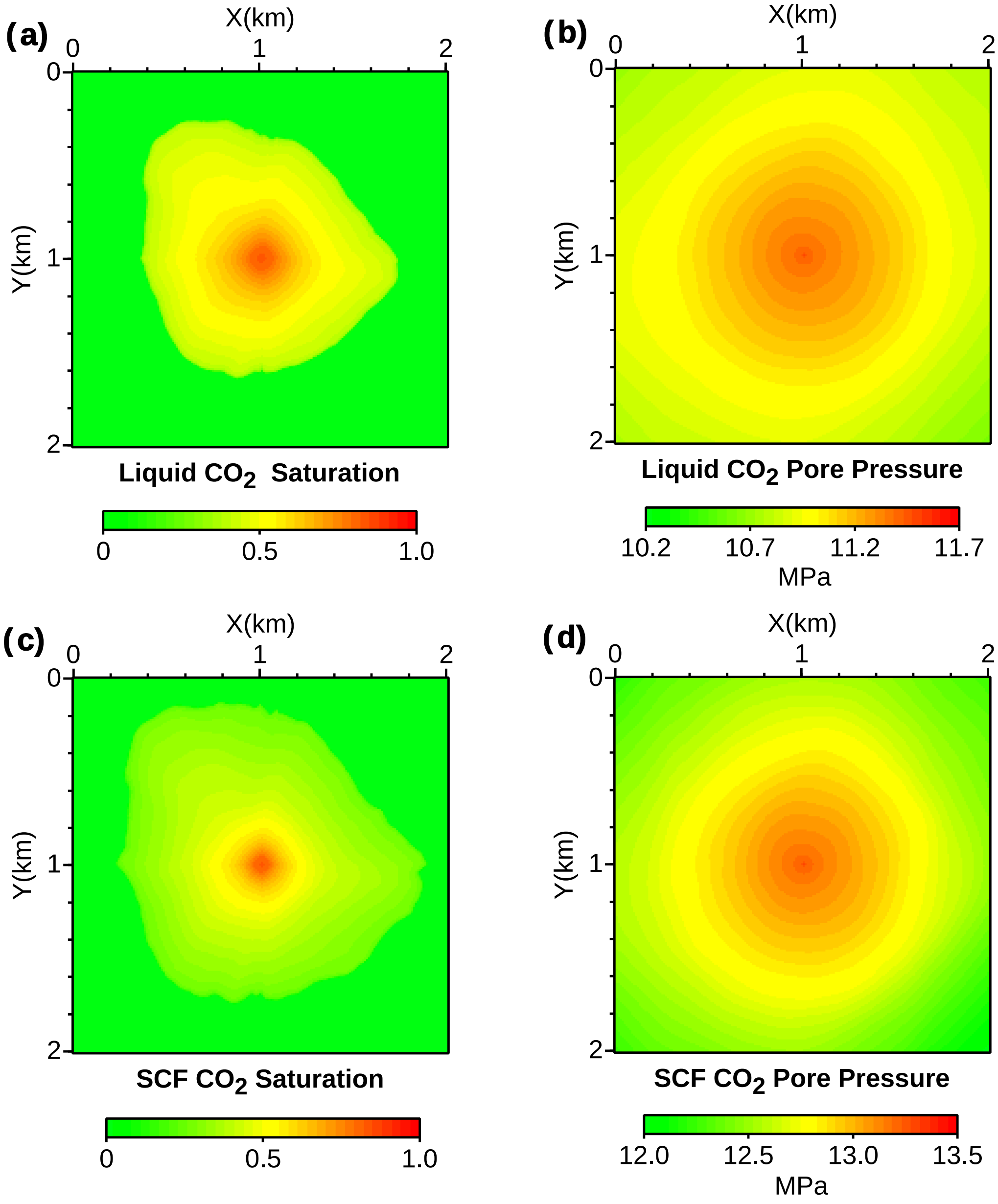

Fig. 5.6. Fluid simulation results. (a) Saturation and (b) pore pressure of liquid CO_2 model after 180 day injection. (c) Saturation and (d) pore pressure of SCF CO_2 model after 90-day injection.

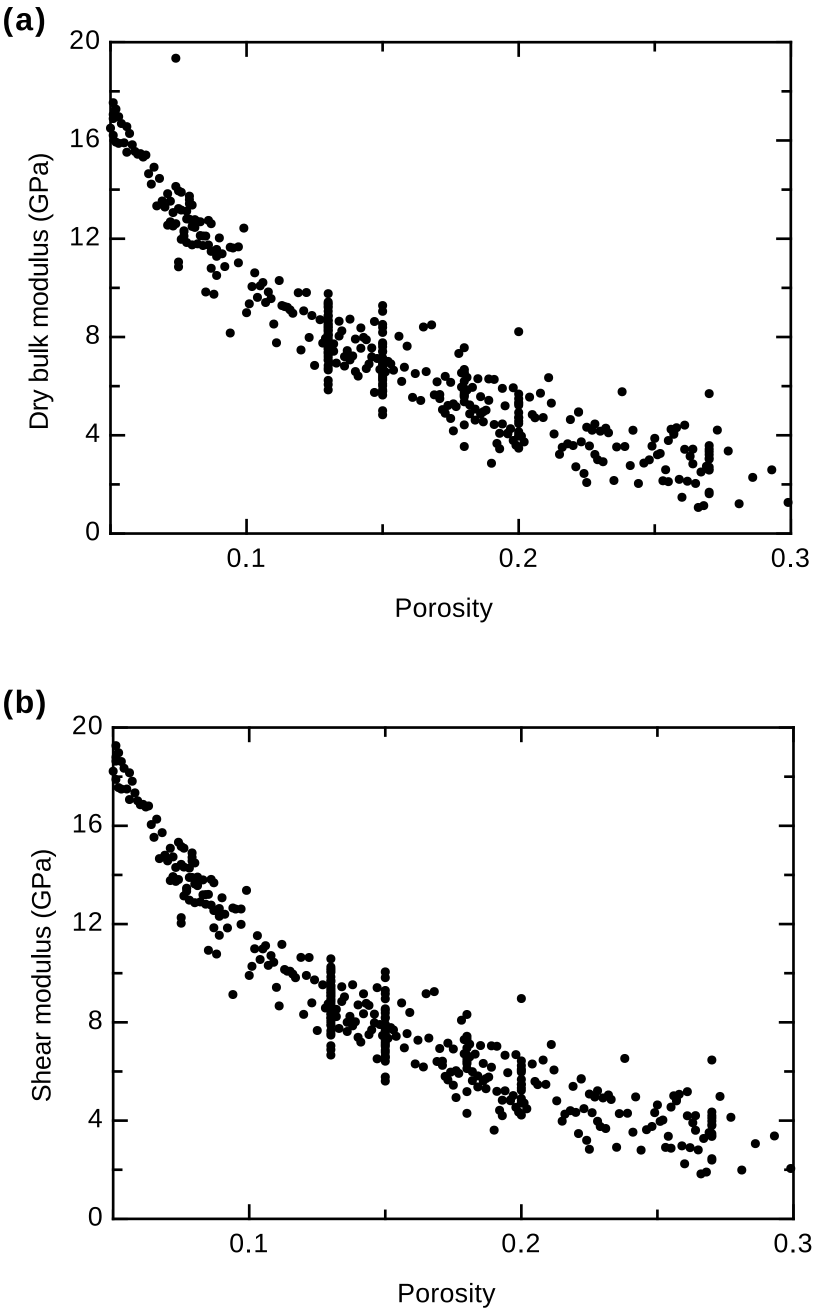

Fig. 5.7. Cross plots of (a) dry bulk and (b) shear moduli to porosity. These are the synthetic examples based on core measurements in published papers. Mean curves of these scatters are computed from the equations in Dvorkin and Nur (1996).

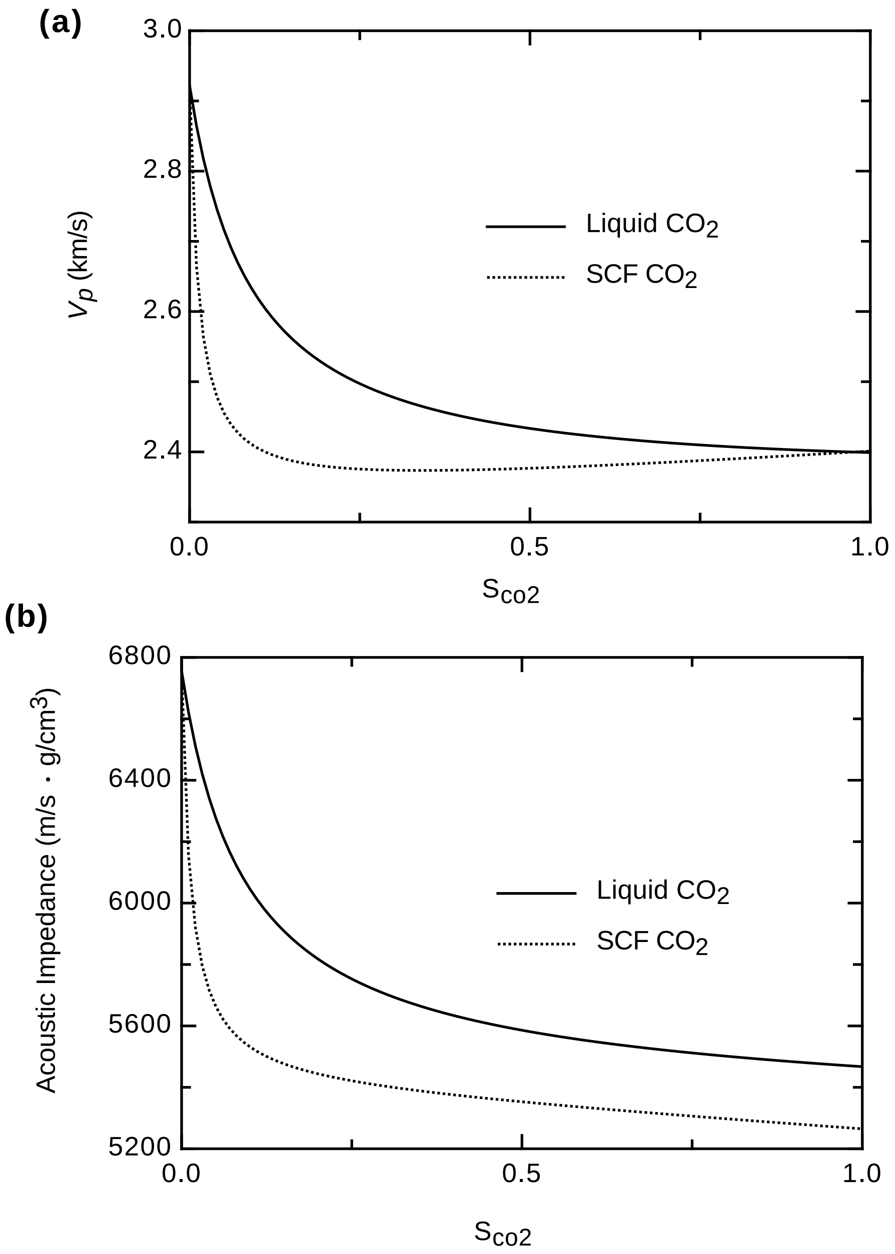

Fig. 5.8. (a) *P*-wave velocity and (b) acoustic impedance of a reservoir versus CO_2 saturation for liquid and SCF models based on Gassmann equation. Porosity, bulk and shear moduli, pore pressure, and fluid properties are assumed to be constant to drive these curves.

the gas-water reservoir. If the CO_2 saturation increases from 0 to 80%, velocities decrease 17 and 18% for the liquid and SCF CO_2 models, respectively. Acoustic impedance as a function of CO_2 saturation is computed in Figure 5.8b. Even though the reservoir velocities of the liquid and the SCF CO_2 models are close to each other over 80% CO_2 saturation, the acoustic impedance for SCF CO_2 is lower than that of liquid CO_2 due to its low density (Figure 5.2). We assumed that porosity, dry bulk modulus, and pressure were constant in Figure 5.8. Decreases of effective pressure resulting from CO_2 injection are another factor that decreases the velocity of the reservoir. We computed the velocity as a function of effective pressure with different fluid saturations in Figure 5.9a. Initial effective pressure is 12 MPa, which decreases to 8 MPa and 7 MPa for liquid and SCF CO_2 models, respectively. The velocity decreases caused by these pressure drops are 5% and 8% for liquid and SCF CO_2 respectively. Acoustic impedance as a function of effective pressure for three different fluid models are computed in Figure 5.9b. The SCF CO_2 model shows larger impedance contrast with water saturation than liquid CO_2 model over the entire pressure range, which means we can expect larger amplitude changes in the SCF CO_2 model. Each curve in Figure 5.9 is computed with the assumption of 80% water or CO_2 saturation and constant porosity. The bulk density of the reservoir is computed using

$$\rho_{bulk} = (1-\phi)\rho_{matrix} + \phi(\rho_{CO2}S_{CO2} + \rho_{water}(1-S_{CO2})) \tag{5.1}$$

where ρ_{bulk} is reservoir bulk density, ρ_{matrix} is rock matrix density, ρ_{CO2} is CO_2 density, ρ_{water} is water density, and S_{CO2} is CO_2 saturation. The fluid densities in equation (5.1) are computed from the ECLIPSE simulation.

Based on the above rock-physics properties and fluid simulation results, we computed synthetic seismograms using the ray-Born technique to model the time-lapse seismic image of the reservoir. This method estimates the wave fields scattered by

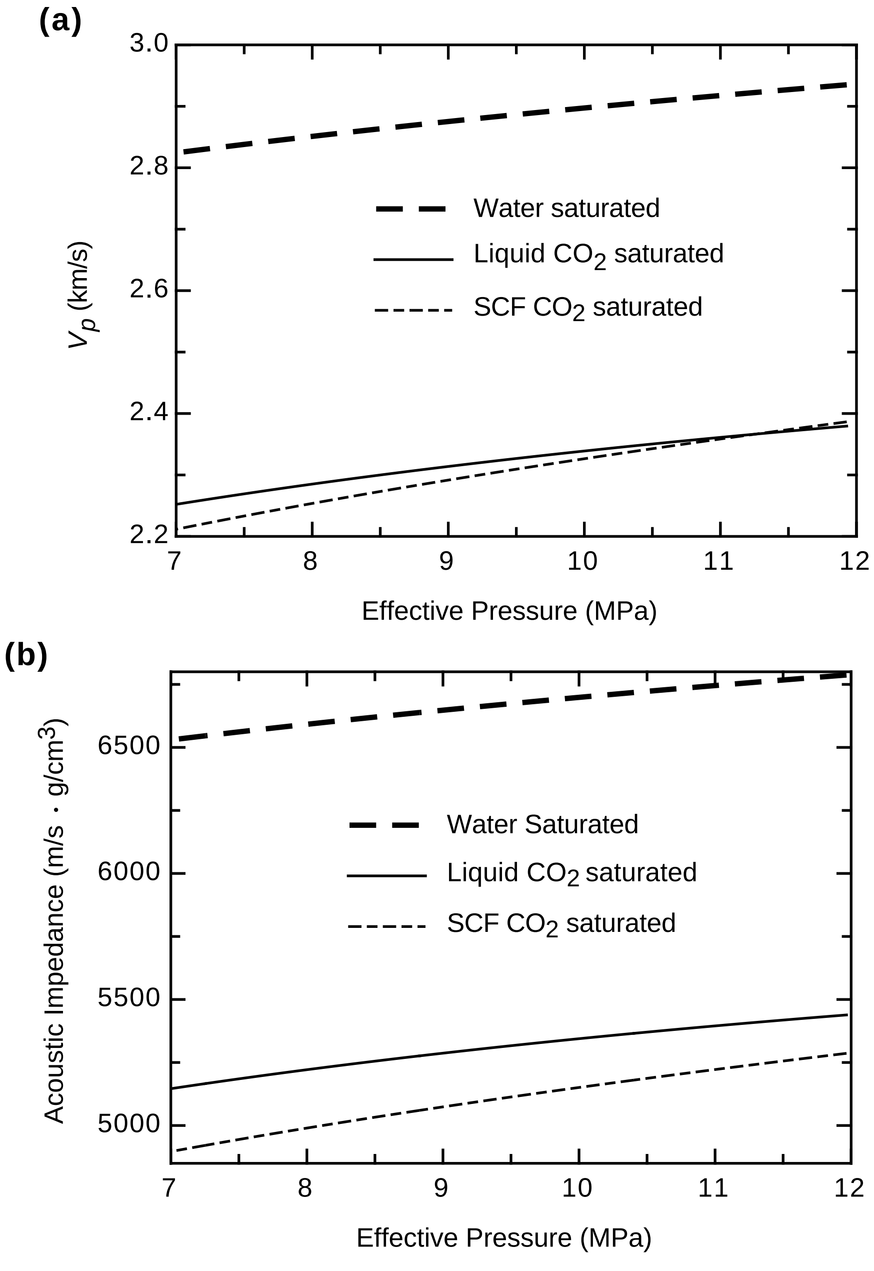

Fig. 5.9. (a) *P*-wave velocity and (b) acoustic impedance of the reservoir versus effective pressure for different pore fluids. CO_2 curves assumed to be 80% CO_2 - or water-saturated.

the small perturbations in properties of an elastic medium (Beydoun and Mendes, 1989; Gibson, Jr. et al., 1993).

5.3.4 Seismic modeling

We complete our model definition by assuming that the reservoir formation is overlain by a homogeneous overburden with velocities $V_p = 4.6$ km/s, $V_s = 2.4$ km/s and density $\rho = 2.6$ g/cm^3. The reservoir, which is 2000 × 2000 × 10 m, is discretized to 10 ×10 ×10 m blocks. The depth of reservoir is 884 m. We examined the effect of the CO_2 on the seismic response by computing zero-offset and far-offset seismograms, to which we applied a phase-shift migration. The seismic arrays are 101 × 101 source-geophones with 20 m spacing. The far-offset seismic arrays have 1 km source-geophone offset corresponding to a 30° incident angle.

The seismic amplitudes of the zero-offset models computed for before and after CO_2 injection are shown in Figure 5.10. The amplitudes after liquid CO_2 injection increased a little was compared to one for the before-injection model (Figure 5.10a and b). For the SCF CO_2 model, the CO_2 saturated zone after the injection can be identified more clearly in Figure 5.10d. Time-lapse amplitudes of both models are computed by subtracting the seismic image for before CO_2 injection from one for after CO_2 injection (Figure 5.11). The four time-lapse amplitudes in Figure 5.11 are normalized by individual scalar values computed from the average amplitude of the before-injection model of each case. The maximum amplitude change for each model is listed in Table 5.1. The time-lapse amplitudes for far-offset models are larger than for the zero-offset model, which means that it can be detected more easily in real field examples (Figure 5.11 and Table 5.1). Furthermore, the amplitude change is larger for the SCF CO_2 than for the liquid phase. This difference can be explained easily; it is a consequence of the different properties of the two CO_2 phases (Figure 5.2).

Specifically, the contrast between the density and compressibility of SCF CO_2 and the corresponding properties of water is larger than for liquid CO_2 . As the CO_2 replaces the water, the SCF phase will, in general, produce a larger change in the acoustic impedance of the formation than will liquid carbon dioxide (Figure 5.8b). In Figure 5.11d, the ampliutde changes within a saturated zone are different, depending on the location. This is due to the heterogeneity of reservoir properities such as porosity and bulk modulus.

Table 5.1. Maximum amplitude changes for four different models. The far-offset SCF CO_2 model shows the largest amplitude changes among these models.

Model	Maximum Amplitude Change (%)
Liquid CO_2 Zero Offset	32
Liquid CO_2 Far Offset	41
SCF CO_2 Zero Offset	43
SCF CO_2 Far Offset	54

5.3.5 Time-lapse AVO analysis

AVO response has been applied successfully to estimate reservoir rock properties (Castagna et al., 1993) and to detect hydrocarbons (Smith and Gidlow, 1987). This techinique is also being applied to time-lapse seismic monitoring to detect the changes of reservoir properties (Tura and Lumley, 1999; Foster and Keys, 1999; Ross, 2000). Standard AVO analysis uses an approximate form of the Zoeppritz reflection coefficient equations for small incident angle:

$$R(\theta) \approx A + B \sin^2 \theta, \tag{5.2}$$

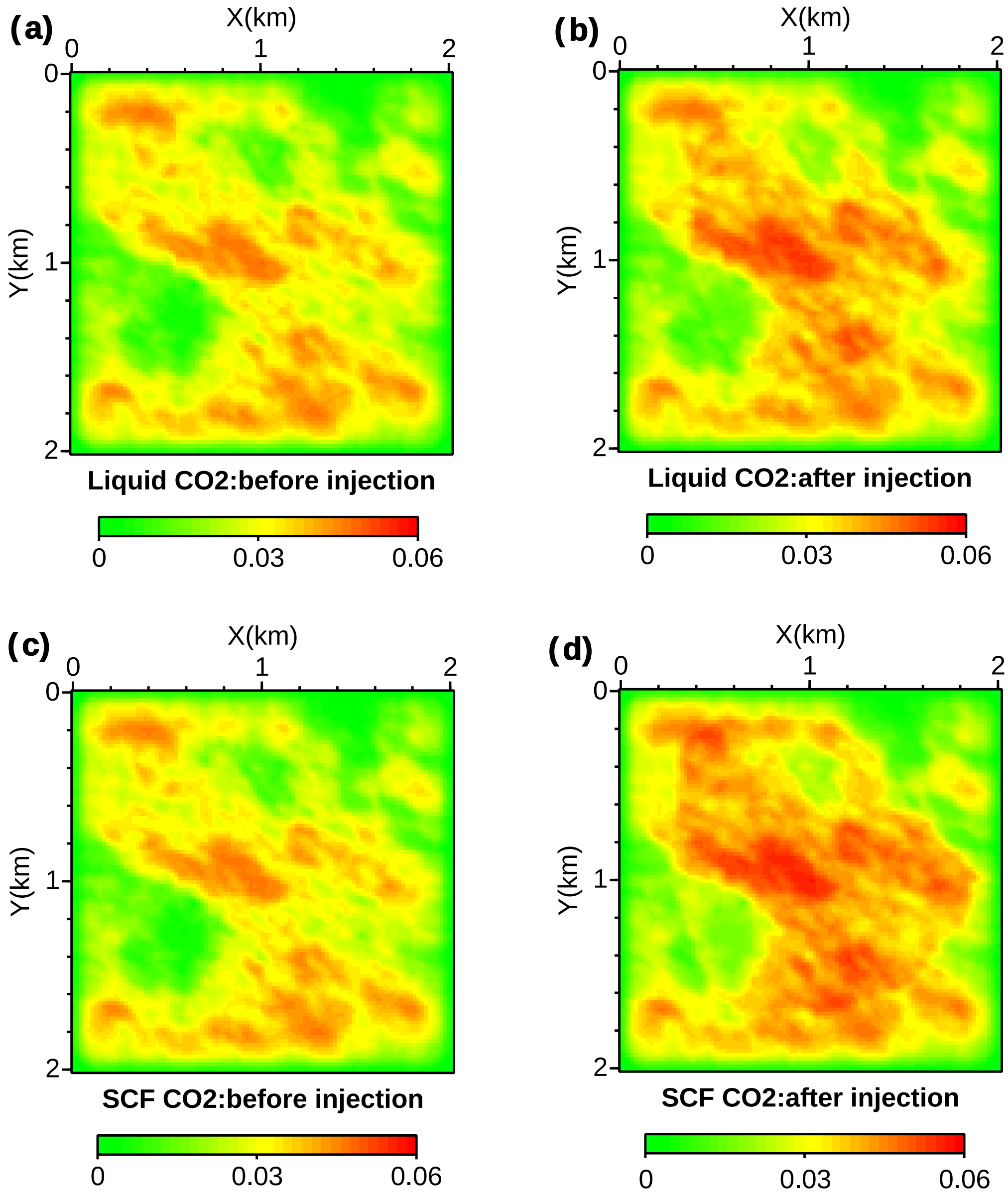

Fig. 5.10. Seismic amplitudes (a) before liquid CO_2 injection, (b) after liquid CO_2 injection, (c) before SCF CO_2 injection, and (d) after SCF CO_2 injection.

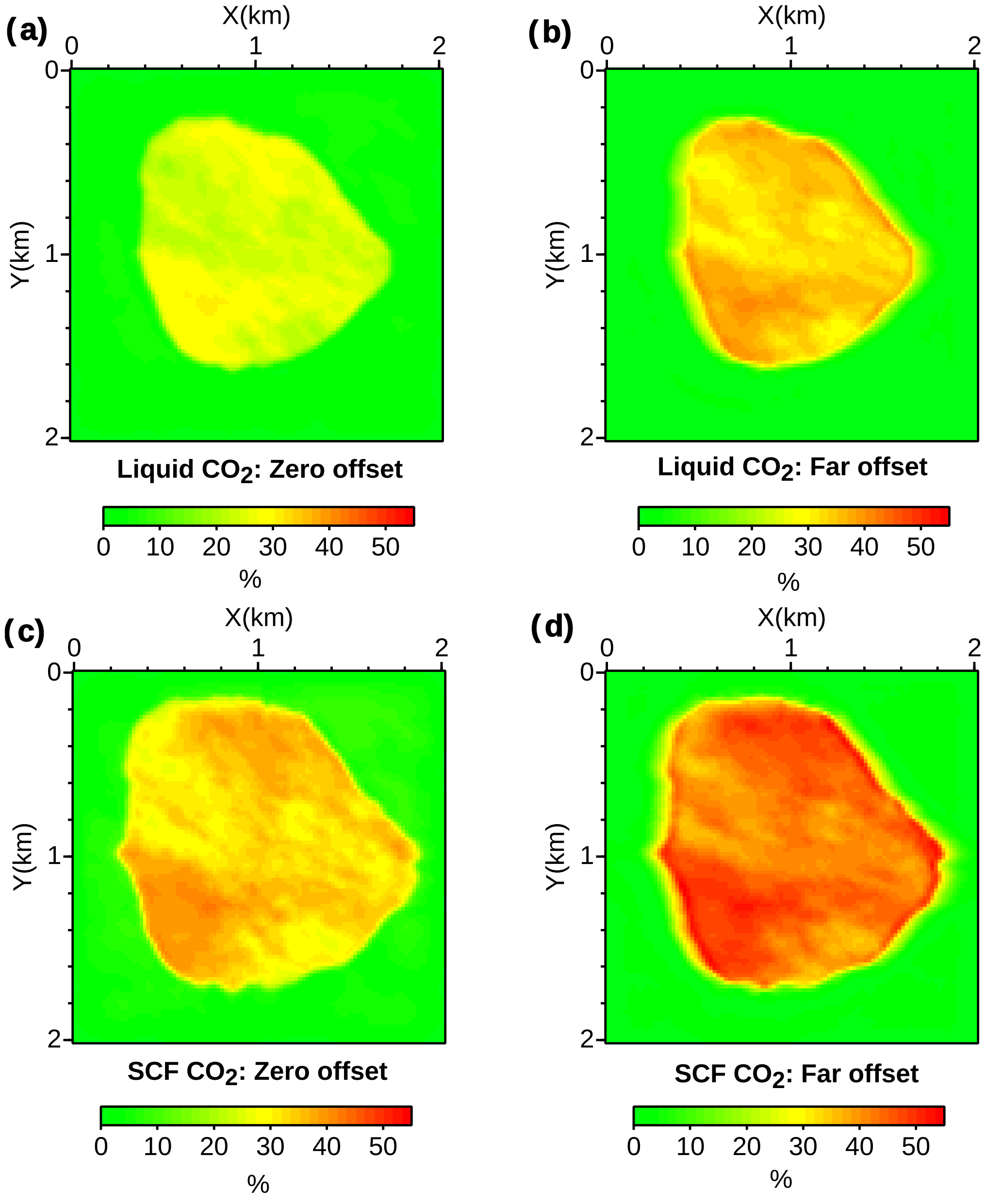

Fig. 5.11. Time-lapse amplitudes for (a) the liquid CO_2 model, and (b) the SCF CO_2 model.

where θ is the incident angle, A is the intercept at the normal incidence, and B is the gradient of reflection coefficient (Shuey, 1985). We computed the A and B values using the zero- and far- offset data for both before and after injection models. The time-lapse AVO are computed by subtracting A and B for the before-injection model from values for the after-injection model. Figure 5.12 shows the time-lapse AVO of liquid and SCF CO_2 models. The color scale represents the CO_2 saturation. We can divide the scattered values in Figure 5.12 into two groups: red points correspond to less than 10% CO_2 saturation, and green and blue points correspond to more than 50% CO_2 saturation. Time-lapse AVO responses for the SCF CO_2 model show larger changes than ones for liquid CO_2 model. Thus, we can separate AVO responses of liquid CO_2 from SCF CO_2 in favorable conditions, even though they might overlap in conventional cross plots of intercept and gradient.

5.3.6 Uncertainties in time-lapse seismic modeling

One of the reservoir properties sensitive to time-lapse seismic modeling is the dry bulk modulus (Lumley et al., 1997). For example, stiffer rocks are less sensitive to time-lapse seismic modeling, while softer rocks such as unconsolidated rocks shows stronger time-lapse seismic reponse (see Figure 3.1 and 3.2 in chapter III). However, bulk modulus data for reservoirs are only availble from well logs or core measurements, which are quite sparse. Thus, there is generally significant uncertainty in values of dry bulk modulus of the reservoir for time-lapse seismic modeling. Also, the cross plot of dry bulk modulus as a function of porosity has large scatter due to its heterogeneity (Han et al., 1986). Thus, in this section, we generated multiple models of dry bulk modulus of the reserovir using cloud transforms to estimate the uncertainty in time-lapse seismic modeling due to the uncertainty in bulk modulus (Srivastava, 1992; Aly et al., 1999). Figure 5.13 shows examples of realizations of dry bulk modulus fields.

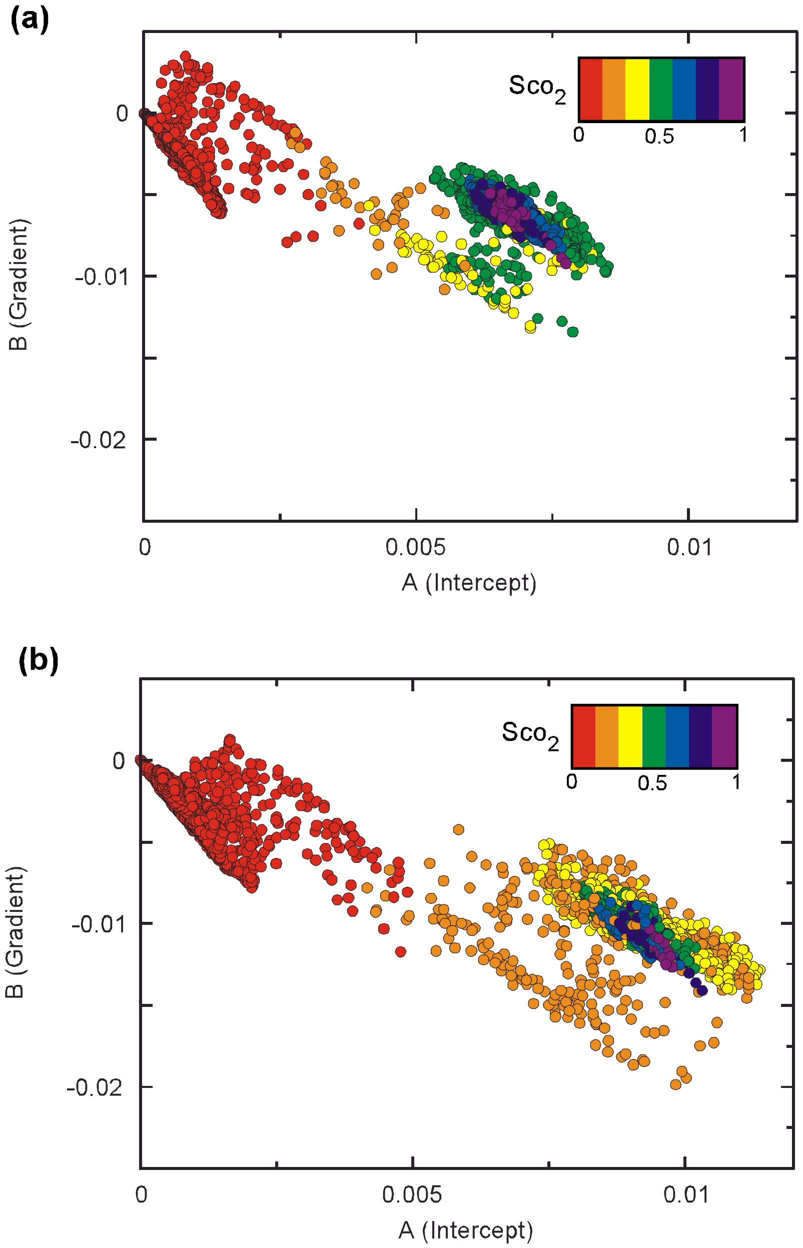

Fig. 5.12. Cross plot of intercept, A, and gradient, B, for time-lapse AVO responses in (a) liquid and (b) SCF CO_2 models. Color scale represents CO_2 saturation. SCF CO_2 model shows a little larger time-lapse AVO responses compared to those in liquid CO_2 model.

The CO_2 saturation and pore pressure from the ECLIPSE simulation of the liquid CO_2 model are applied to compute the Gassmann equation.

We computed the 2D synthetic seismograms along the $X = 0.7$ km line for before and after liquid CO_2 injection based on 30 dry bulk modulus models. To evaluate correlations among porosity, dry bulk modulus, and amplitude changes, we plotted these values along X =0.7 km in Figure 5.14. Average dry bulk modulus of 30 models shows an inverse correlation with porosity in Figure 5.14a and b, which is due to its inverse relationship with porosity (Han et al., 1986) (Figure 5.3). The standard deviation of the 30 dry bulk modulus models does not correlate with porosity, since the cloud transform generates multiple models based on an unconditional probability field (Srivastava, 1992; Aly et al., 1999). The range of dry bulk modulus at X =0.7 km is from 2 to 17 GPa, and the average standard deviation is about 1 GPa in our model (Figure 5.14b). The average amplitude change for the 30 dry bulk modulus models is about 30%, and standard deviation of this is about 1.5% (Figure 5.14c). If the standard deviation of dry bulk modulus models increases by a factor of 5, we might expect standard deviations in amplitude changes roughly 5 times larger, which are about 7%. That is still low compared to a 30% amplitude change. Thus, the effects of the uncertainty in dry bulk modulus on time-lapse seismic modeling is small because the amplitude change due to CO_2 injection is relatively large, as much as 30%.

5.4 Conclusions

We have used numerical modeling to study the seismic response of liquid and supercritical fluid (SCF) CO_2 sequestration in a reservoir. For both models, we computed zero-offset and far-offset seismic modeling before and after CO_2 injection. The liquid

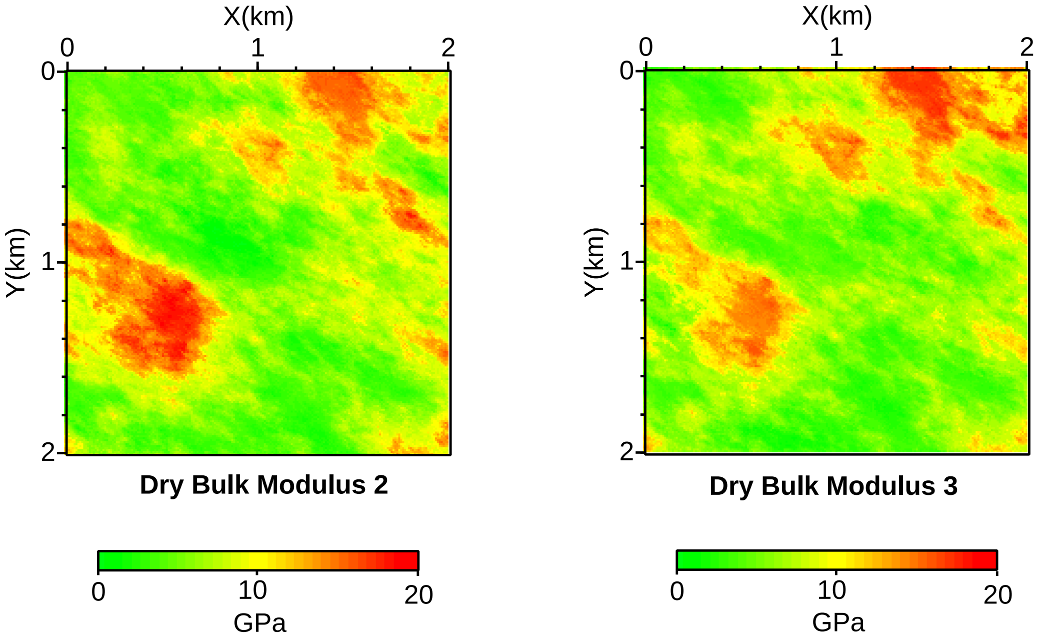
X(km)
0
1
2
Y(km)
0
1
2
0
10
20
GPa
X(km)
0
1
2
Y(km)
0
1
2
0
10
20
GPa

Dry Bulk Modulus 2

Dry Bulk Modulus 3

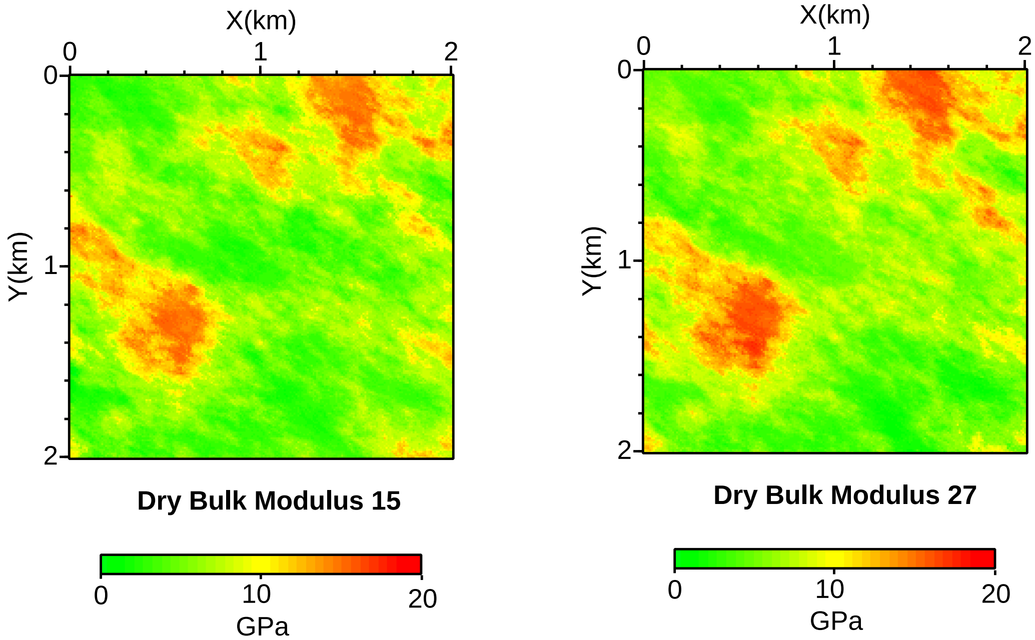
X(km)
0
1
2
Y(km)
0
1
2
0
10
20
GPa
X(km)
0
1
2
Y(km)
0
1
2
0
10
20
GPa

Dry Bulk Modulus 15

Dry Bulk Modulus 27

Fig. 5.13. Examples of dry bulk modulus realizations using cloud transform

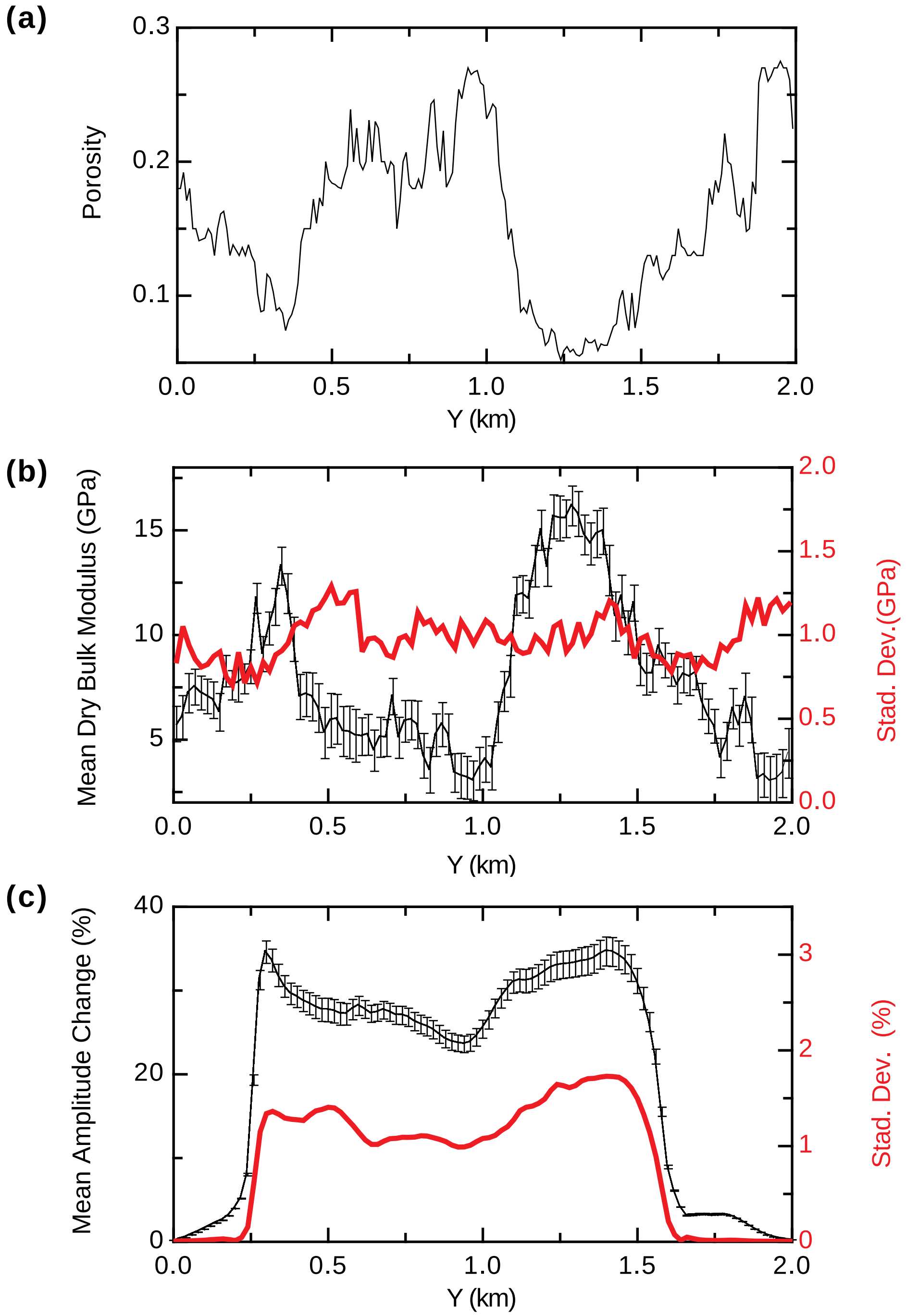

Fig. 5.14. (a) Porosity of resevoir at $X = 0.7$ km. (b) The solid curve and error bars represent the average dry bulk modulus and standard deviations, respectively, computed from 30 dry bulk modulus realizations. The red curve is the standard deviation with the scale on the right axis. (c) The solid curve and error bars represent the average amplitude changes and standard deviations, respectively, computed from 30 sesmic simulations. The red curve is the standard deviation with the scale on the right axis.

and SCF CO_2 model show maximum 32% and 43% amplitude changes, respectively, for zero-offset seismic modeling. Far-offsect seismic modeling shows lager amplitude change than zero-offset model such as 43% and 54% for liquid and SCF CO_2 models, respectively. The time-lapse AVO analysis using zero-offset and far-offset seismic data was computed. The SCF CO_2 model shows larger changes in time-lapse AVO responses in the cross plot of the intercept-gradient than liquid CO_2 model.

The uncertainty analysis of time-lapse seismic monitoring based on 27 different models of dry bulk modulus was evaluated. For about 1 GPa standard deviation of dry bulk modulus causes about 1.5% standard deviation in amplitude change, which is relatively small uncertainty compared to about 30% amplitude change after liquid CO_2 injection. In similiar reservoir conditions with our model, the uncertainty in dry bulk modulus doesn't much affect on the time-laspe seimic modeling.

CHAPTER VI

TIME-LAPSE SEISMIC MONITORING OF A 4500 FT RESERVOIR IN EUGENE ISLAND BLOCK 354 FIELD (TEAL SOUTH), THE GULF OF MEXICO

6.1 Introduction

Time-lapse seismic monitoring has been applied to increase efficiency of hydrocarbon recovery in existing fields (Jack, 1998; Lumley et al., 1999; Shyeh et al., 1999). Primary production of a reservoir will replace hydrocarbon with water or gas cap in a formation, which causes the changes in acoustic impedance of a reservoir (Nur, 1989; Wang et al., 1991). Forward models of time-lapse seismic monitoring based on well logs, production history, and core measurements can help to predict the changes in seismic response during production and to interpret and understand results of field data. Specifically, comparison of the forward model with actual time-lapse seismic data can help to interpret 4D seismic images and find by-passed reservoir sites (Johnston et al., 2002).

Our study area is the Teal South Field (Eugene Island block 354) in the Gulf of Mexico. Energy Research Clearing House (ERCH) organized the consortium for Teal South time-lapse seismic monitoring project. The main goal of this project is to study the feasibility of a permanent reservoir monitoring system using multi-component ocean bottom cable (OBC) (Ebrom et al., 1998). Several academic members in this consortium have contributed to this project. Straub et al. (2000) contributed to cross-equalization of 1995 and 997 seismic data sets, and Ashbaugh et al. (2000) contributed to production history match. Based on these previous studies, in this chapter, we develop a forward model for the 4500-ft sand reservoir by integrating seismic interpretation, well logs, production history, and 4D seismic data.

6.2 Teal South Field

6.2.1 4500-ft reservoir geologic setting

The Teal South Field is located in the Gulf of Mexico, offshore Louisiana, in 85 m of water (Figure 6.1a). It consists of multiple minibasins at depths of 1300 m to 2400 m, and reservoirs are unconsolidated Tertiary sands. The structure of this field is a deep-seated anticlinal ridge terminated by counter-regional growth faults (Andre and Rinehart, 1997). The intersections of north-south growth faults with east-west growth faults create many structural traps (Andre and Rinehart, 1997). The average thickness of the reservoir is about 70 m. Fast drops in production rates and the small size of reservoirs, which might mean fast flow rates and high permeability, are the the reason to be chosen as a test site for time-lapse seismic monitoring. Our target reservoir is the 4500-ft sand, which is bounded by normal faults on the east and the west, and dipping to the north (Figure 6.2a). A seismic cross section with the interpretation of 4500-ft reservoir shows the segment of our target horizon at the center (Figure 6.2b).

6.2.2 Production history

Oil and gas production started on November, 1996, and the second seismic survey was acquired on July, 1997. Thus, in our study we only consider the production data until July, 1997. The production history match is computed based on production rate of oil, gas, and water, and pressure data from well D 10 (Ashbaugh et al., 2000). Pore pressure was initially 19 MPa and declined quickly during the 8-month production

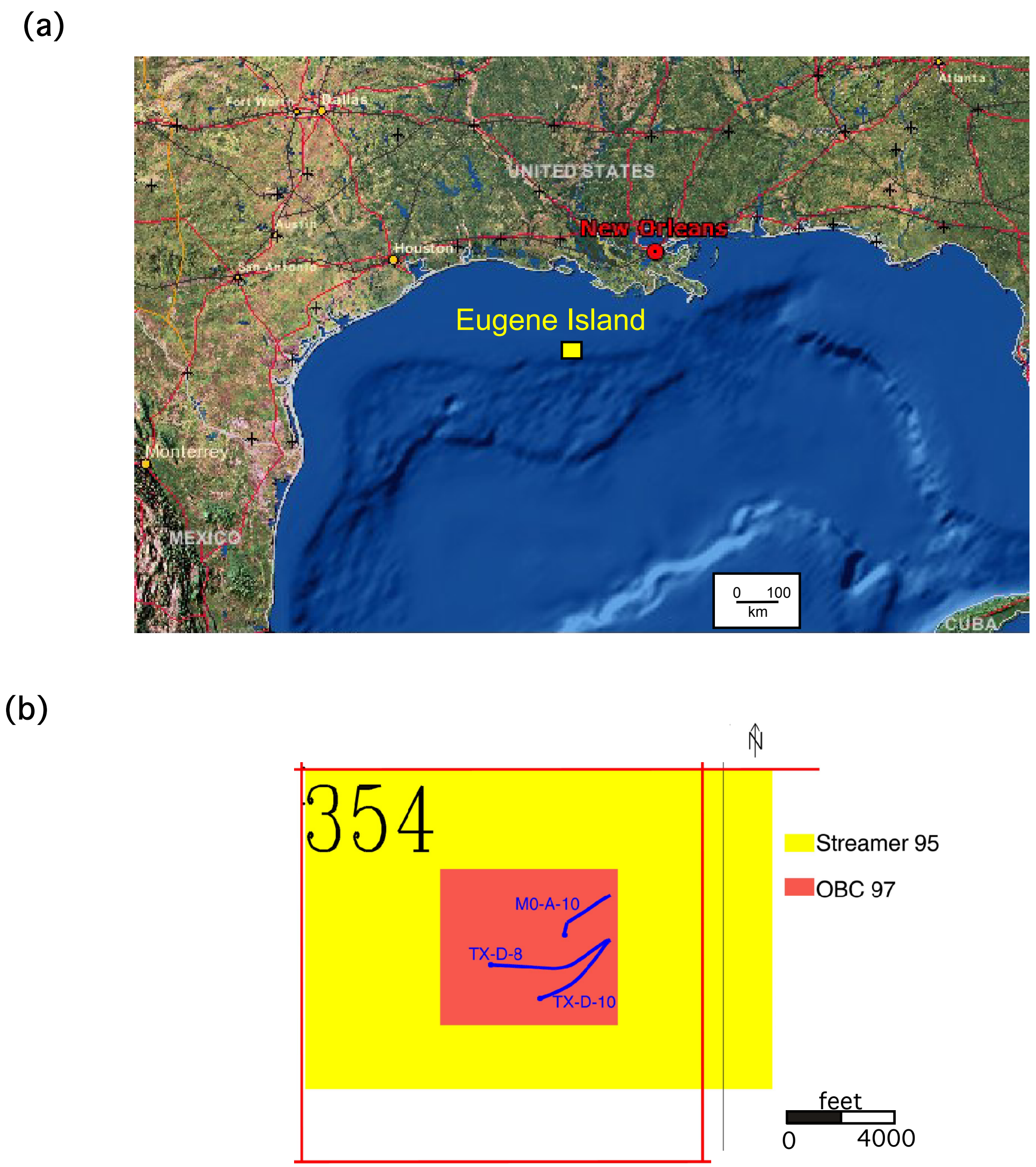
(a)
Atlanta
Fort Worth
Dallas
UNITED STATES
Austin
Houston
New Orleans
San Antonio
Eugene Island
Monterrey
MEXICO
0 100
km
CUBA
(b)
N
354
Streamer 95
OBC 97
M0-A-10
TX-D-8
TX-D-10
feet
0 4000

Fig. 6.1. (a) Location map of Eugene Island in the Gulf of Mexico. (b) Two vintage maps for 3D streamer survey in 1995 (yellow rectangle) and 3D OBC survey in 1997 (orange rectangle) (Straub et al., 2000).

to 13 MPa, which are computed based on shut-in tubing pressure (SITP). Pressure drops caused a gas cap invasion on the top of the 4500-ft sand. Water saturation increased from 22 to 31% during production. Table 6.1 summarizes the changes in reservoir conditions (Ashbaugh et al., 2000). Temperature is 60°C in 1996 and we assumed it wasn't changed during production.

Table 6.1. Changes in pore pressure and fluid contents over production period. Pressure is measured from shut-in tubing pressure (SITP) and temperature for 1996 is measured from well logs and assumed to be constant. Saturation is computed from production history (Ashbaugh et al., 2000).

	1996	1997
Pore Pressure (MPa)	19	13
Temperature (°C)	60	60
S_{water}	0.22	0.31
S_{oil}	0.78	0.67
S_{gas}	0	0.02

6.2.3 Seismic data

The Teal South field has been surveyed more than three times since 1995. The first legacy survey prior to production was done in 1995, and the other two ocean bottom cable (OBC) surveys were performed in 1997 and 1999. Yellow and orange rectangles represent streamer and OBC data, respectively, in the map illustrating these surveys (Figure 6.1b). In this study, we analyze two 3D seismic data sets acquired in 1995 and 1997.

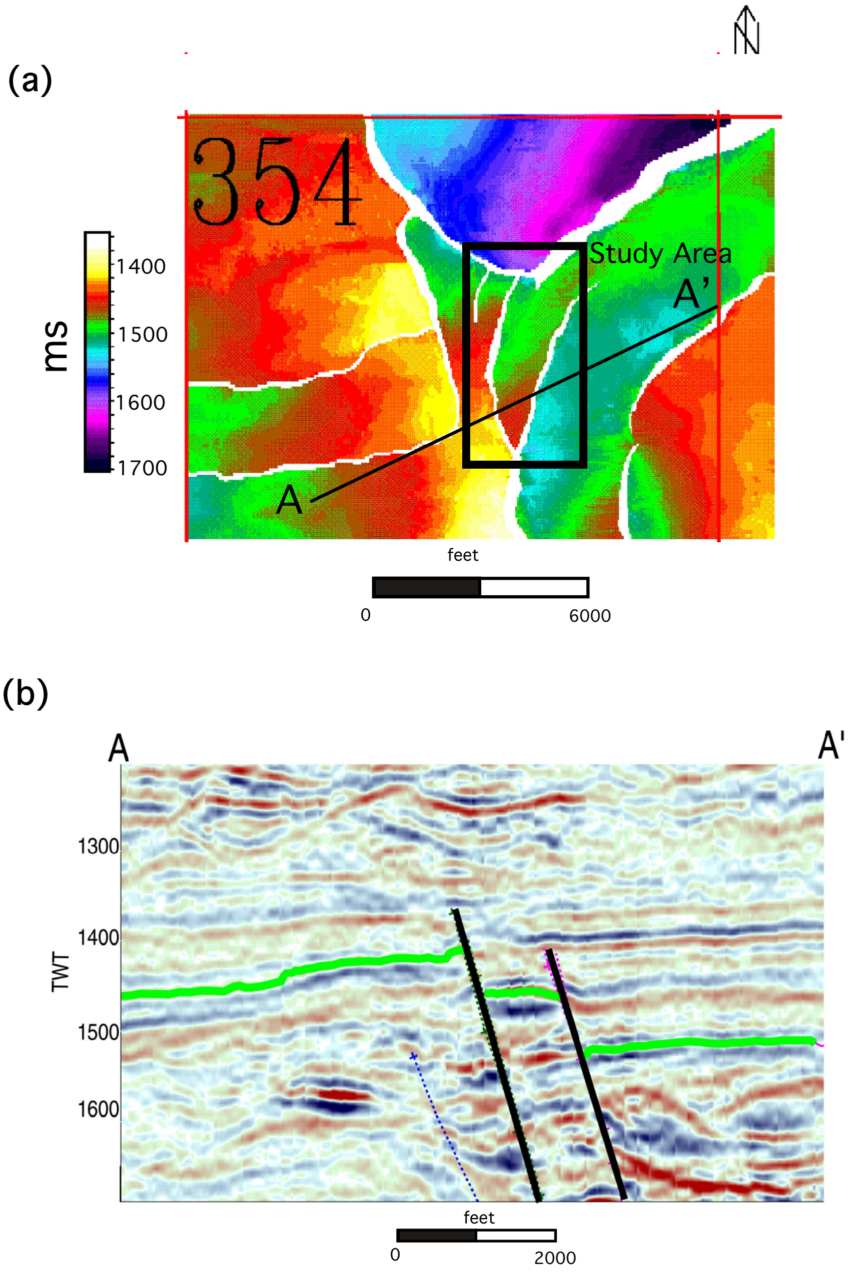
(a)
N
354
Study Area
A'
A
ms
1400
1500
1600
1700
feet
0
6000
(b)
A
A'
1300
1400
1500
1600
TWT
feet
0
2000

Fig. 6.2. (a) Base map of Eugene Island, block 354 with two-way traveltime of 4500-ft reservoir. (b) Seismic cross-section from A to A'. The green horizon represents 4500-ft reservoir with two normal faults (Straub et al., 2000).

6.2.4 Processing and analysis of time-lapse seismic data

Cross equalization for streamer 1995 and OBC 1997 data includes re-binning of OBC 1997 data for trace-to-trace comparison, cross-correlation between bins to estimate time-shift, bandpass filtering for the same frequency contents, and amplitude normalization (Straub et al., 2000). An amplitude-difference image was computed based on cross-equalized data of 1995 and 1997 (Figure 6.3). Amplitude brightening occurs in the southwest region and amplitude dimming occurs in the northeast region (Figure 6.3).

6.3 Modeling

The 3D reservoir model is constructed using on the depth-converted 4500 ft time horizon. Regridding is done for discretized blocks of the model using ordinary kriging. The dimension of the model are 1220 × 530 m, with a thickness of 70 m, and it is discretized into 5 × 5 × 5 m blocks.

6.3.1 Rock physics modeling

A simple porosity model of the reservoir was generated using a conventional kriging method based on three known values from porosity logs (Deutsch and Journel, 1998) (Figure 6.4). The porosity of the resulting 4500 ft reservoir model ranges from 0.26 to 0.34.

Empirical relationships of elastic moduli to porosity and pressure are provided constraints for the rock-physics model. Gardner and Harris (1968) developed the empirical equations based on measurements of dry, freshly packed quartz sand as

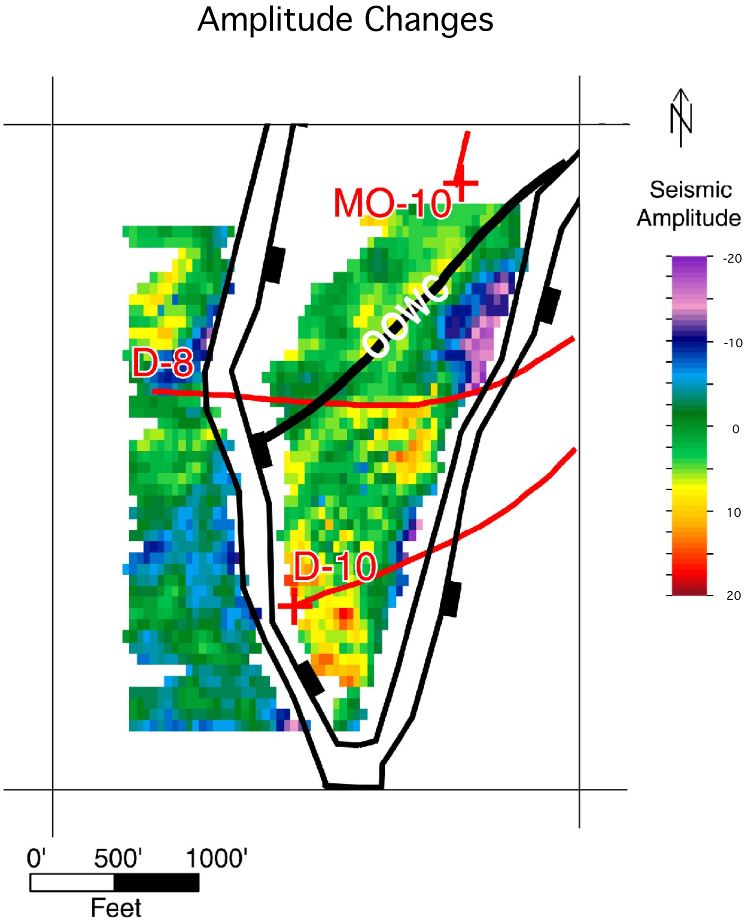
Amplitude Changes
MO-10
OOWC
D-8
D-10
N
Seismic Amplitude
-20
-10
0
10
20
0'
500'
1000'
Feet

Fig. 6.3. Amplitude difference of 1995 and 1997 surveys (Straub et al., 2000).

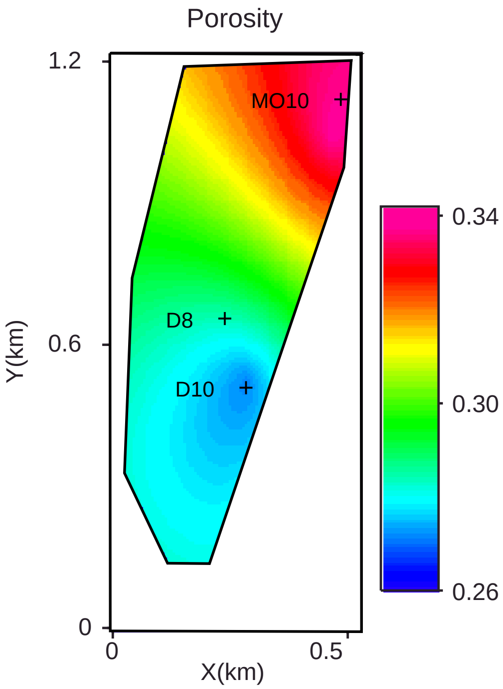

Fig. 6.4. A porosity model generated using ordinary kriging method, based on three known values from porosity logs.

follows:

$$\begin{aligned} \mu &= 0.15(0.58 - \phi)\sqrt{P}, \\ E &= 0.32(0.58 - \phi)\sqrt{P}, \end{aligned} \tag{6.1}$$

where μ is shear modulus, E is Young's modulus, ϕ is porosity, and P is effective pressure in MPa. We modified the coefficients of the above equations to fit our P- and S- wave sonic velocities from well D10 as follows:

$$\begin{aligned} \mu &= 0.145(0.58 - \phi)\sqrt{P}, \\ E &= 0.269(0.58 - \phi)\sqrt{P}. \end{aligned} \tag{6.2}$$

6.3.2 Fluid saturation modeling

Changes in reservoir properties during production between November, 1996 and July, 1997 are estimated based on previously established production history (Table 6.1)

(Ashbaugh et al., 2000). Because we did not have sufficient constraints to perform a full fluid-flow simulation, we assigned values of saturation based on interpretations of the original oil-water contact (OOWC) (Figure 6.5). This allows us to model only the part of the reservoir which may have changed fluid conditions during production. The northern portion of the 4500-ft reservoir, which is above the OOWC, is 100% water-saturated during the production period. We assumed that fluid contents and pressure change only occur in the southern part of the 4500-ft reservoir (Figure 6.5). At initial production in November 1996, the 4500 ft reservoir was saturated with 22% water and 78% oil. By July 1997, a gas cap had been generated and oil saturation was reduced to 67% (Table 6.1). In the seismic data, amplitude dimming was detected in the northeast portion of the 4500-ft reservoir, and amplitude brightening was observed towards the southwest (Figure 6.3). To model these negative and positive amplitude changes, we increased gas saturation by 2% only in the southwest region of the 4500-ft reservoir, with the gas saturation decreasing to 0% towards the northeast.

6.3.3 Gassmann equation

Once we assigned values for the elastic properties and pore fluids of the 4500 ft reservoir, we applied the Gassmann equation to predict changes in elastic properties (Gassmann, 1951). The bulk density was computed using the volume average equation:

$$\rho_{bulk} = (1-\phi)\rho_{matrix} + \phi(\rho_{gas}S_{gas} + \rho_{oil}S_{oil} + \rho_{water}S_{water}), \tag{6.3}$$

where the matrix was assumed to be quartz, the hydrocarbon properties were values provided by Texaco, and water properties were computed from empirical equations (Batzle and Wang, 1992). The bulk modulus of mixed fluids was computed using

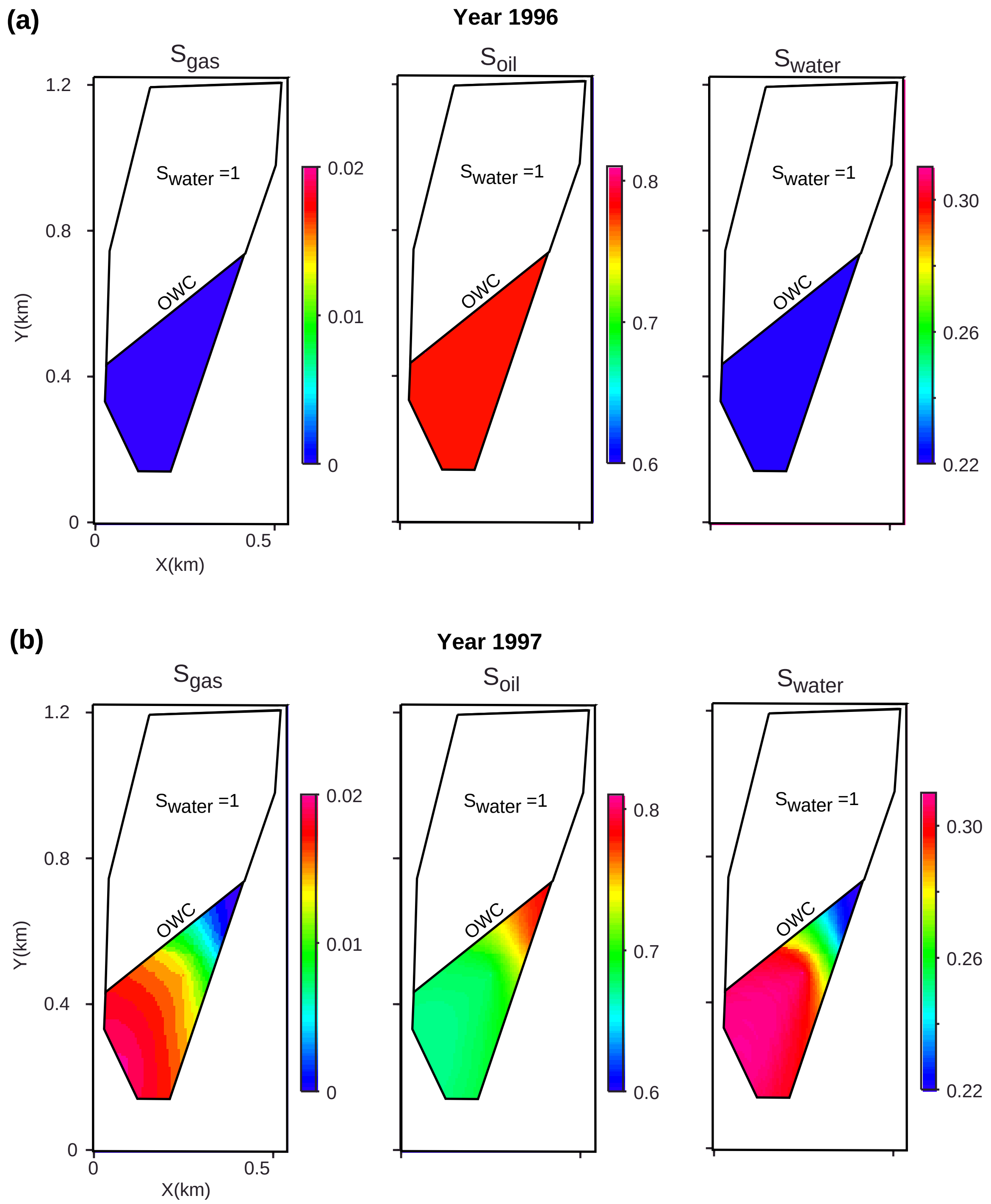

Fig. 6.5. (a) Gas, oil, and water saturation in 1996. (b) Gas, oil, and water saturation in 1997.

Wood's equation:

$$\frac{1}{K_f} = \frac{S_{gas}}{K_{gas}} + \frac{S_{oil}}{K_{oil}} + \frac{S_{water}}{K_{water}}. \tag{6.4}$$

The velocities, densities, and acoustic impedance of the 1996 model are plotted in Figures 6.6. In this model, the reservoir properties of the northern part of 4500-ft reservoir (above the OOWC line) are not homogeneous, even though we assumed homogeneous pore pressure. This is because porosity is not homogeneous in our model (Figure 6.4). V_p drops occur in the southwest region of 4500-ft reservoir due to gas-cap invasion and V_p increases in the northeast region due to the pore pressure drops (Figure 6.7a). V_s changes are due to pore pressure drops (Figure 6.7b). Bulk density increases because water saturation increase (Figure 6.7c). Acoustic impedance increases in the northeast region due to pore-pressure drops and it 1decreases in the southwest region due to gas-cap invasion (Figure 6.7d).

6.3.4 Ray-Born seismic modeling

3D synthetic seismograms for the 1996 and 1997 reservoir models are computed using the ray-Born algorithm (Beydoun and Mendes, 1989; Gibson, Jr. et al., 1993). This method was developed to estimate the wave fields scattered by the small perturbations in properties of an elastic medium. We assumed that the velocities and density of overburden layers are homogeneous. Even though this is not true for earth, it is still acceptable for time-lapse seismic modeling, since during hydrocarbon production the properties and geology of overburden layers are changed little. In our seismic models, we simulated zero-offset sources and receivers with 20-m spacing. There are 112 and 77 sources and receivers in the north-south and east-west directions, respectively, covering the 3D reservoir. After computing the synthetic seismograms, a conventional phase-shift migration is applied.

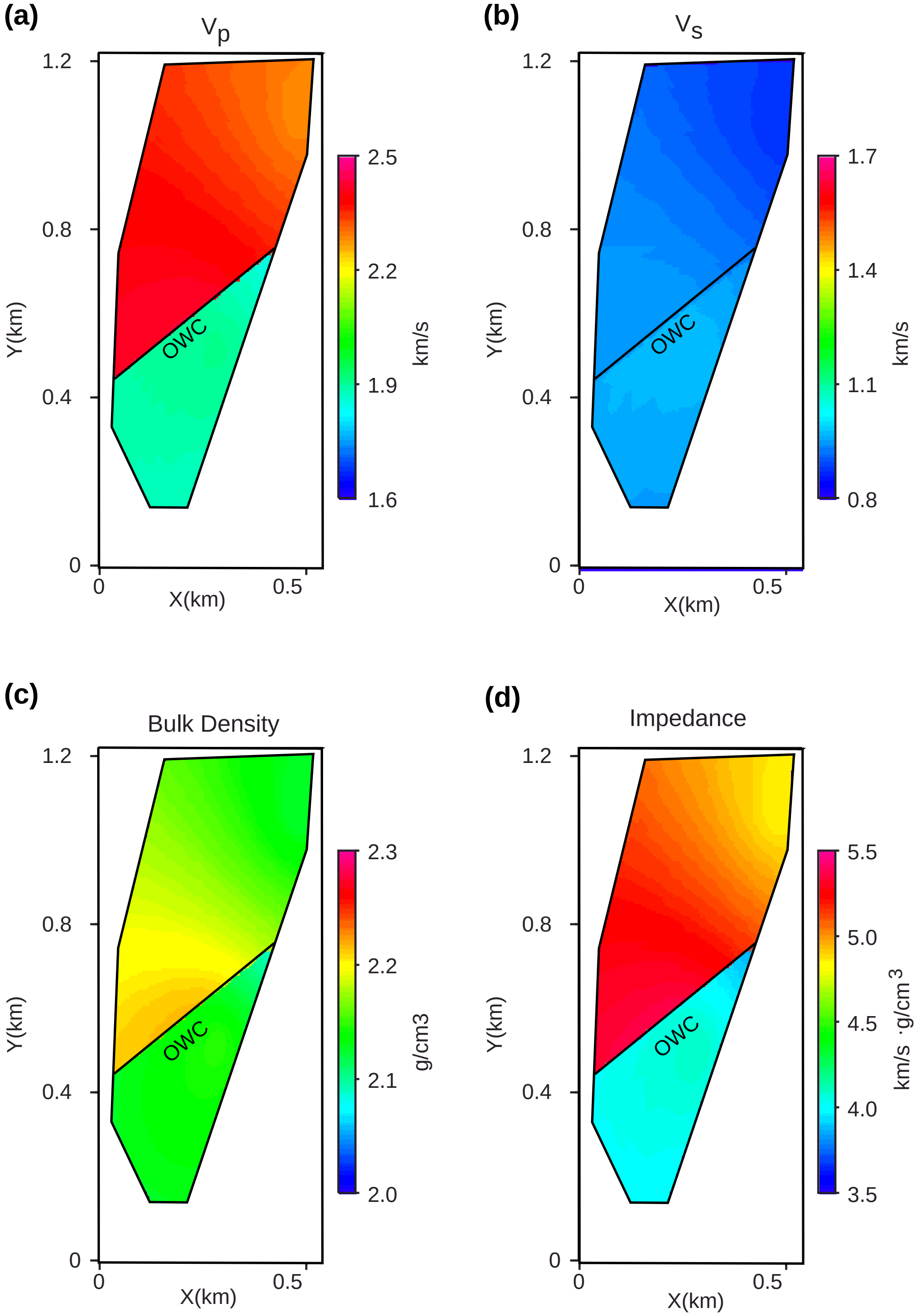

Fig. 6.6. (a) P-wave velocity, (b) S-wave velocity, (c) bulk density, and (d) acoustic impedance of 1996 reservoir model.

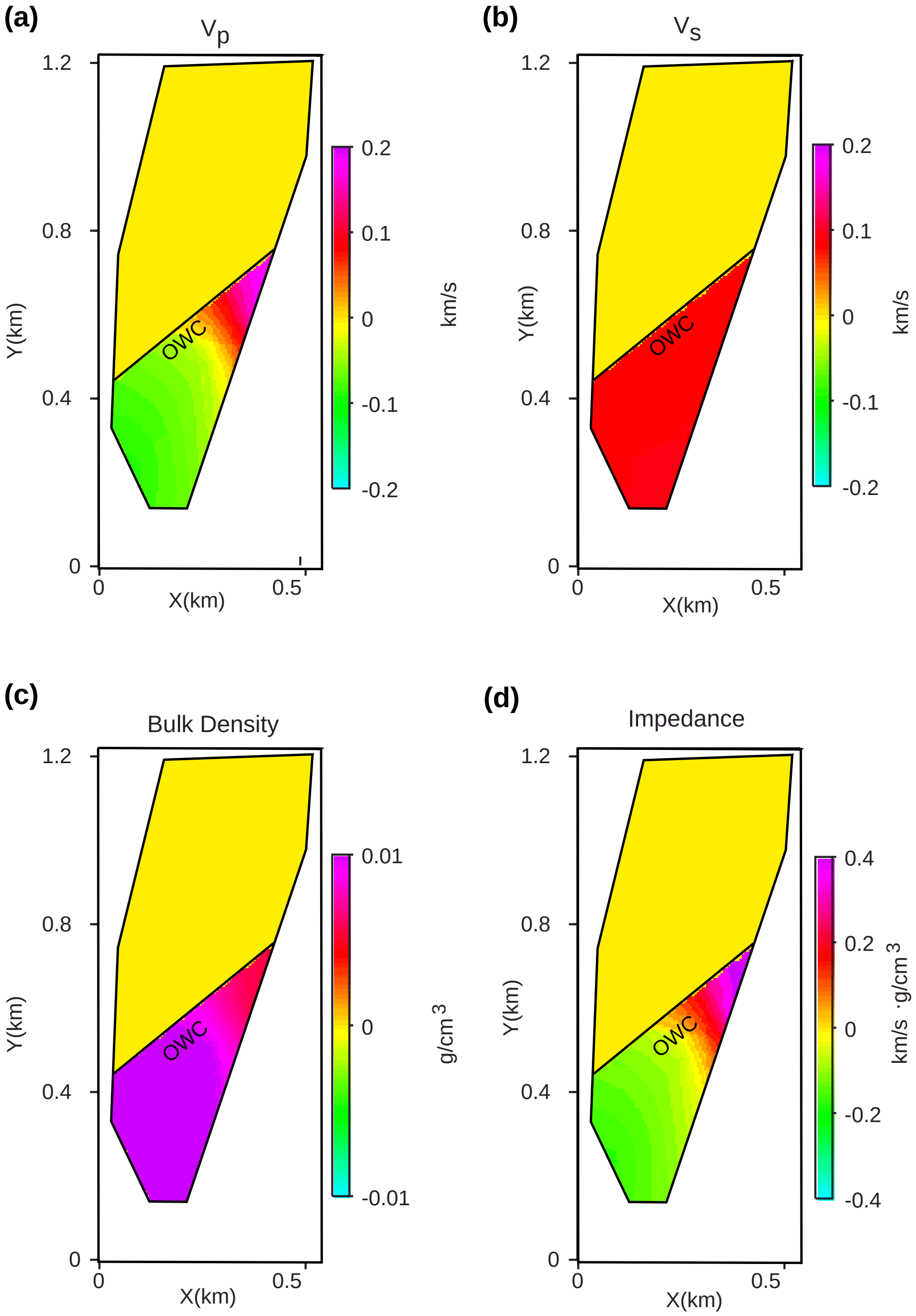

Fig. 6.7. Changes in (a) P-wave velocity, (b) S-wave velocity, (c) bulk density, and (d) acoustic impedance of the reservoir model during production.

2D seismic profiles across the reservoir in the north-south direction are plotted in Figure 6.8 for both the 1996 and the 1997 models, as are the difference traces. The reservoir horizon is dipping toward the northerly direction (Figure 6.8). The difference traces are computed by subtracting 1996 traces from 1997 traces. Polarity changes along the horizon occur in the difference traces because opposite changes in acoustic impedance occur within the reservoir during production, thereby causing opposite effects on amplitude changes.

Amplitudes for 1996 and 1997 models are plotted in Figure 6.9a. Amplitudes for both models show a bright region below the OWC, which is similar to the field seismic data in Figure 6.9b (Straub et al., 2000). The amplitude changes based on the model and the field data are plotted in Figure 6.10. Negative amplitude changes due to pore-pressure drops, which occur in the northeast region, and positive amplitude changes due to gas cap generation occurred in the southwest region (Figure 6.10a). These amplitude changes are also similar to those in field data (Figure 6.10b). There is a difference between the modeled and actual seismic differences in Figure 6.10a, which is partially caused by the heterogeneities in actual reservoir properties that we did not consider in our model due to lack of well logs.

However, it is important to recall that this is an unconsolidated reservoir. The sensitivity analysis in chapter III(Figure 3.2) showed that for unconsolidated sands, bulk modulus change due to fluid substitution is not sensitive to porosity. Assuming that porosity changes in the reservoir are not too significant, the lack of horizontal variability of bulk modulus in our models should not cause very large errors.

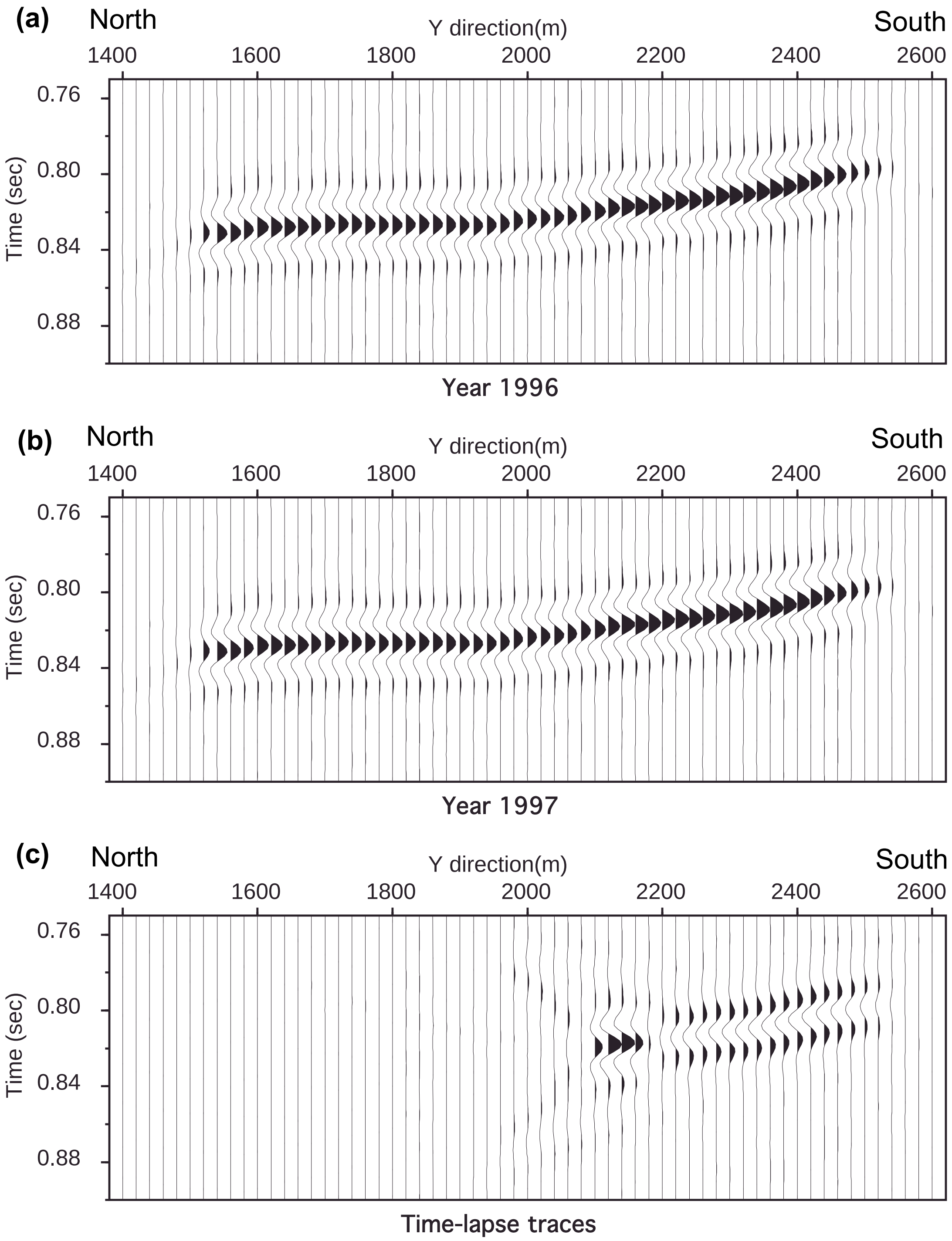

Fig. 6.8. Synthetic seismograms for (a) 1996 reservoir model (b) 1997 reservoir model, and (c) difference traces.

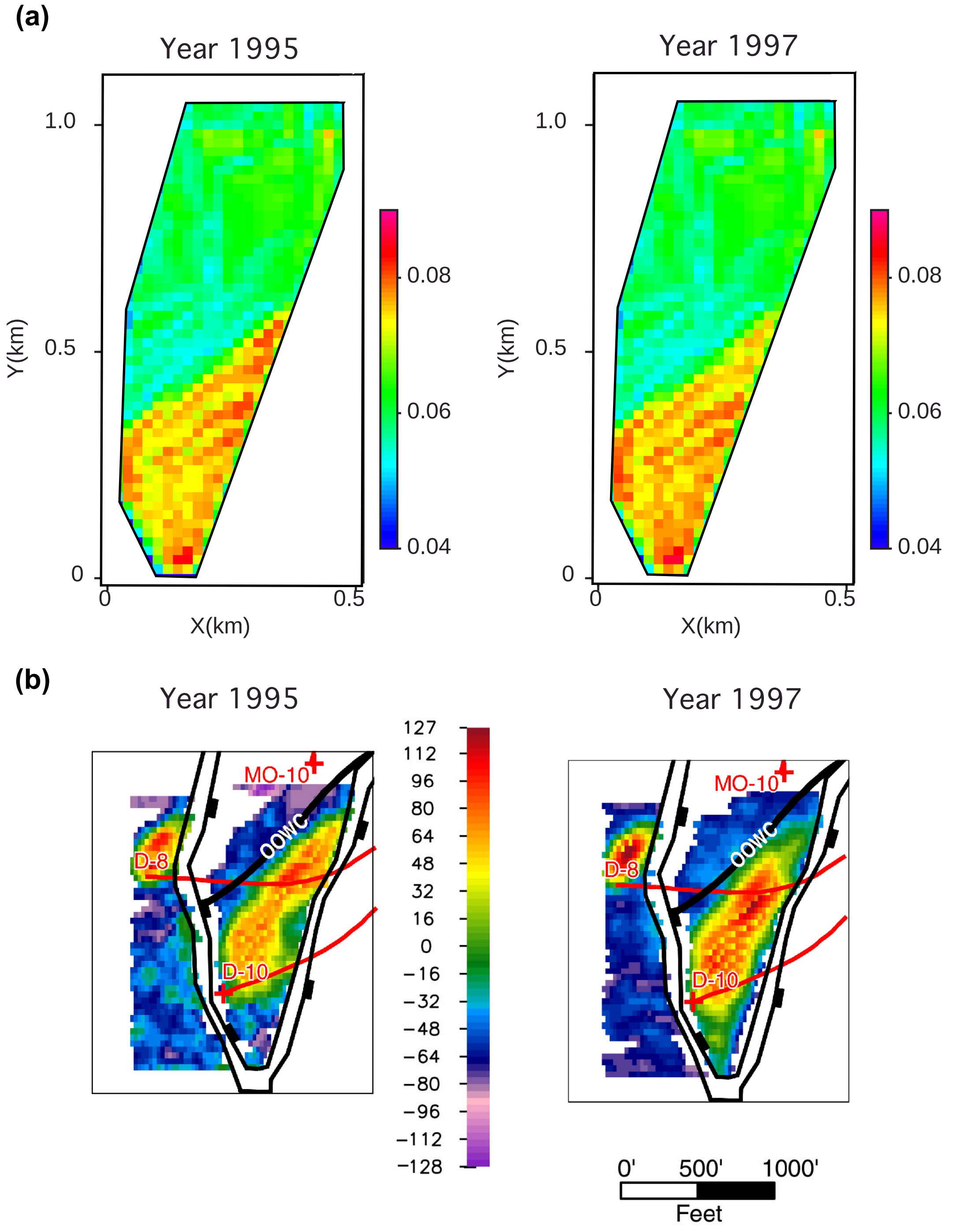

Fig. 6.9. (a) Amplitudes computed from the reservoir model. (b) Amplitudes from field seismic data (Straub et al., 2000).

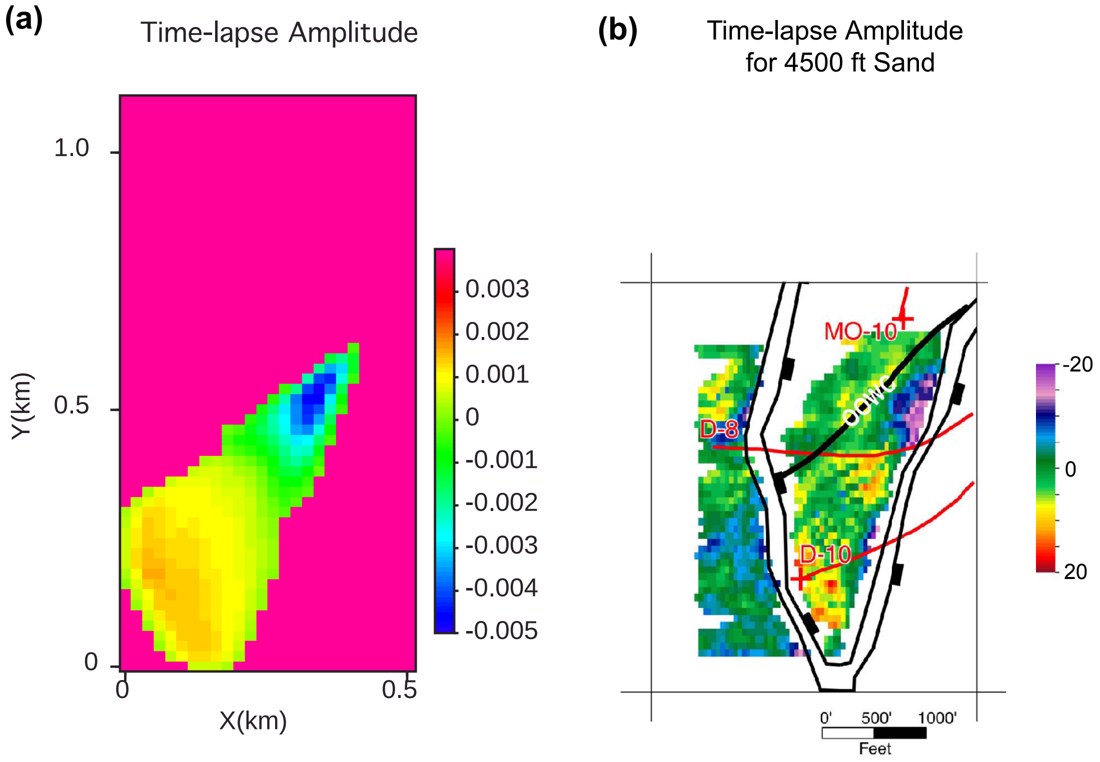
(a)
Time-lapse Amplitude
1.0
0.5
0
Y(km)
0
0.5
X(km)
0.003
0.002
0.001
0
-0.001
-0.002
-0.003
-0.004
-0.005
(b)
Time-lapse Amplitude
for 4500 ft Sand
MO-10
D-8
OOWC
D-10
-20
0
20
0'
500'
1000'
Feet

Fig. 6.10. (a) Amplitude changes computed from reservoir model. (b) Amplitude changes computed from actual field data (Straub et al., 2000).

6.4 Conclusions

3D seismic data acquired at different times over Teal South field (Eugene Island block 354) in the Gulf of Mexico have been interpreted and modeled to map reservoir property changes linked to production. A production history match shows 2% gas invasion occurs on the top of the horizon, oil saturation decreased to 67% from 78%, and pore pressure drops from 19 MPa to 13 Mpa. We constructed the seismic model based on a production history match and a petrophysical model to compute the amplitude differences associated with production. The modeled time-lapse seismic difference shows amplitude changes similar to actual amplitude changes: positive amplitude changes in the northeast of the reservoir and negative amplitude changes in the southwest of the reservoir, which can be interpreted as pore-pressure drops causing amplitude dimming in the northeast and gas invasion causing amplitude brightening in the southwest.

CHAPTER VII

CONCLUSIONS

In this work we developed a fast, forward-modeling procedure that combines fluid flow, rock physics, and seismic-wave propagation. It includes streamline fluid-flow simulation, which is a fast method analogous to seismic ray theory; rock-physics modeling, which is critical to determining the sensitivity of seismic velocity to fluid contents; and ray-Born seismic modeling, which is a hybrid method combining ray theory and the Born approximation. Using our techniques, we tested many reservoir models to understand time-lapse seismic experiments conducted in a variety reservoir conditions.

The primary contributions of this dissertation are as follows:

- We developed a new modeling procedure for time-lapse seismic monitoring, which includes streamline fluid-flow simulation, rock physics, and 3D ray-Born seismic modeling. This high-speed modeling techniques can consider the heterogeneous nature of porosity, permeability, and elastic moduli of a reservoir. It can also consider different rock-physics models such as consolidated and unconsolidated sandstone.

- We quantified the sensitivity of amplitude changes to fluid contents for different rock-physics models. For rock-physics models of consolidated sandstone, the high-porosity region shows larger amplitude changes than low-porosity regions during fluid substitution, but an unconsolidated sandstone model shows that there are no uniform relationships between porosity and amplitude changes.

- We estimated the uncertainties in time-lapse seismic modeling caused by uncertainties in permeability and dry bulk modulus values of a reservoir using stochastic methods. In the stochastic modeling of permeability, the maximum uncertainties in amplitude change occur around the water front, since this region has maximum uncertainties in water saturation. We applied the same test to stochastic modeling of dry bulk modulus. The maximum uncertainties in amplitude change occur at the injection well where the maximum saturation changes occur, because in the Gassmann equation, the sensitivity of saturated bulk modulus to dry bulk modulus is maximum where changes in fluid saturation are maximum.

- We applied our modeling technique to model CO_2 injection in a depleted reservoir. Different phases of CO_2 , supercritical fluid and liquid, have different acoustic properties. We computed the time-lapse seismic images for the supercritical fluid CO_2 and liquid CO_2 injection cases. The amplitude changes after supercritical fluid CO_2 injection are larger than those in the liquid CO_2 model because contrasts in acoustic properties between water and CO_2 are larger for supercritical fluid CO_2 than liquid CO_2 .

- Two seismic surveys over the Eugene Island block 354 (Teal South) in the Gulf of Mexico, were acquired in 1995 and 1997. We developed a forward model for a 4500-ft sand reservoir to understand which changes in reservoir properties are responsible for observed 4D images. The results of our forward modeling suggest that the amplitude dimming in the northeast region of the reservoir is caused by pore-pressure decreases and that amplitude brightening in the southeast is caused by gas exsolution.

7.1 Future work

- The ray-Born seismic modeling method computes seismic-wave propagation caused by the perturbation of elastic moduli and density relative to background properties. This algorithm is quite a fast method compared to finite difference schemes. However, we still need to repeat 3D seismic modeling over a period of time, which is computationally expensive. A possible solution for this problem is that we compute the changes in perturbations of elastic moduli and density caused by the changes in reservoir properties during fluid substitution, and then compute seismic-wave propagation only for changes in perturbations during production. If we can verify this idea theoretically, it can dramatically reduce the computation times. This idea is originally based on the work of Kirchner and Shapiro (2001).

- The reservoir model in our study is a quite thin layer with 10-m thickness, since the ray-Born algorithm assumes homogeneous background. Thus, to model a relatively thick reservoir, a hybrid method combining ray-tracing and a finite difference scheme might be a more accurate method to model a thick reservoir, even though it is more computationally expensive.

- Time-lapse seismic image is caused not only by changes in fluid saturation but also by pressure changes under an assumpiton of a perfect repeatability condition. To separate these combined effects of reservoir property changes on a 4D image, seismic inversion of elastic moduli and density using multicomponent seismic data can provide important information to delineate the changes in reservoir properties during production.

- In our rock-physics, fluid-flow, and seismic modeling, we applied uniform grid block size with 10 x 10 x 10 m. However, upscaling or downscaling of the block size depending on each modeling step may be more efficient to reduce computational time. For example, seismic wavelength used in our modeling is about 150 m, and it can't resolve the geologic feature with 10 m size. Thus, if we upscale the rock physics model to larger block size, we can optimize the computational cost.

- Our forward modeling of Teal South field is based on a 4D image computed from 1995 streamer data and 1997 OBC data. However, due to different seismic acquisition methods and the geometry of two seismic data sets, there might be a large uncertainty in cross-equalizations of two different data sets. If we can analyze OBC data acquired in 1997 and 1998, which have the same acquisition geometry and processing, we can reduce the uncertainties in 4D images caused by acquisition foot print. Also, fluid saturation and pressure information based on fluid simulation using production history might improve the reservoir forward model.

REFERENCES

Aly, A., Lee, W. J., Datta-Gupta, A., Mowafi, K., Prida, M., and Latif, M., 1999, Application of geostatistical modeling in an integrated reservoir simulation study of the lower Bahariya reservoir, Egypt: SPE Middle East Oil Show and Conf., Soc. Petr. Eng., SPE 53118.

Andre, R., and Rinehart, K. R., 1997, Teal South prospect, offshore Louisiana: Successful redevelopment of abandoned oil field using new technologies: AAPG Ann. Mtg., AAPG, A4.

Ashbaugh, J., Flemings, P. B., and Altemus, B., 2000, Implications of production history for reservoir drive and geophysical imaging: ERCH 4D-4C forum, Houston Advanced Research Center.

Batzle, M., and Wang, Z., 1992, Seismic properties of pore fluids: Geophysics, **57**, 1396–1408.

Beecy, D. J., and Kuuskraa, V. A., 2001, Status of U.S. geologic carbon sequestration research and technology: Environ. Geosci., **8**, 152–159.

Berg, R. R., 1970, Method for determining permeability from reservoir rock properties: Transactions, **20**, 303–307.

Beydoun, W. B., and Tarantola, A., 1988, First Born and Raytov approximations: Modeling and inversion conditions in a canonical example: J. Acoust. Soc., **83**, 1045–1055.

Beydoun, W. B., and Mendes, M., 1989, Elastic ray-Born l_2-migration/inversion: Geophys. J., **97**, 151–160.

Biondo, B., Mavko, G., Mukerji, T., Rickett, J., Lumley, D., Deutsch, C., Gundeso, R., and Thiele, M., 1998, Reservoir monitoring: a multidisciplinary feasibility study: The Leading Edge, **17**, 1404–1414.

Biot, M. A., 1956, Theory of propagation of elastic waves in a fluid-saturated porous solid: I. low frequency range: J. Acoust. Soc. Am., **28**, 168–178.

Blangy, J. P., Strandenes, S., Moos, D., and Nur, A., 1993, Ultrasonic velocities in sands-revisited: Geophysics, **58**, 344–356.

Budiansky, B., 1965, On the elastic moduli of some heterogeneous materials.: J. Mech. Phys. Solids, **13**, 223–227.

Castagna, J. P., Batzle, M. L., and Kan, T. K., 1993, Rock physics - the link between rock properties and AVO response, *in* Castagna, J. P., and Backus, M. M., Eds., Offset-dependent reflectivity - theory and practice of AVO analysis: Soc. Expl. Geophys.

Červený, V., 2001, Seismic ray theory: Cambridge University Press.

Cheng, C. H., and Toksöz, M. N., 1979, Inversion of seismic velocities for the pore aspect ratio spectrum of a rock: J. Geophys. Res., **84**, 7533–7543.

Cheng, C. H. A., 1978, Seismic velocities in porous rocks: Direct and inverse problems: Ph.D. thesis, MIT.

Crane, M. J., and Blunt, M. J., 1999, Streamline-based simulation of solute transport: Water Resour. Res., **35**, 3061–3078.

Deutsch, C. V., and Journel, A. G., 1994, Integrating well test-derived effective absolute permeabilities, *in* Yarus, J. M., and Chambers, R. L., Eds., Stochastic modeling and geostatistics: Principles, methods, and case studies: AAPG, 131–142.

——— 1998, GSLIB geostatistical software library and user's guide: Oxford University Press.

DOE, 1999, Carbon sequestration research and development, *in* Reichle, D., Ed., Report DOE/SC/FE-1: U. S. Department of Energy.

Dvorkin, J., and Nur, A., 1996, Elasticity of high-porosity sandstones:Theory for two North Sea data sets: Geophysics, **61**, 1363–1370.

Eastwood, J. E., Johnston, D. H., Shyeh, J., Huang, X., Craft, K., Vauthrin, R., and Workman, R., 1999, Time-lapse seismic processing and analysis: Gulf of Mexico example, Lena field: 31st Ann. Offshore Tech. Conf., Offshore Tech. Conf., Proceedings, 135–144.

Eberhart-Phillips, D., Han, D.-H., and Zobak, M. D., 1989, Empirical relationships among seismic velocity, effective pressure, porosity and clay content in sandstone: Geophysics, **54**, 82–89.

Ebrom, D., Krail, P., Ridyard, D., and Scott, L., 1998, 4-C/4-D at Teal South: The Leading Edge, **17**, 1450–1453.

Eiken, O., Brevik, I., Arts, R., E., L., and Fagervik, K., 2000, Seismic monitoring of CO_2 injected into a marine aquifer: 70th Ann. Internat. Mtg., Soc. Expl. Geophys., Expanded Abstract, 1623–1626.

Foster, D. J., and Keys, R. G., 1999, Interpreting AVO responses: 69th Ann. Internat. Mtg., Soc. Expl. Geophys., Expanded Abstract, 748–751.

Gale, J., Christensen, N. P., Cutler, A., and Torp, T., 2001, Demonstrating the potential for geological storage of CO_2: The Sleipner and GESTCO projects: Environ. Geosci., **8**, 160–165.

Gardner, G. H. F., and Harris, M. H., 1968, Velocity and attenuation of elastic waves in sands: SPWLA Logging Symposium, 9th Ann., Trans., M1–M19.

Gassmann, F., 1951, Über die elastizität poröser medien: Vier. der Natur. Gesellschaft in Zürich, **96**, 1–23.

Gentzis, T., 2000, Subsurface sequestration of carbon dioxide - an overview from an Alberta (Canada) perspective: Int. J. Coal Geol., **43**, 287–305.

Gibson, Jr., R. L., and Ben-Menahem, A., 1991, Elastic wave scattering by anisotropic obstacles: Application to fractured volumes: Geophysics, **96**, 19905–19924.

Gibson, Jr., R. L., Toksöz, M. N., and Batini, F., 1993, Ray-Born modeling of fracture-zone reflections in the Larderello geothermal field: Geophys. J. Int., **114**, 81–90.

Gibson, Jr., R. L., Theophanis, S., and Toksöz, M. N., 2000, Physical and numerical modeling of tuning and diffraction in azimuthally anisotropic media: Geophysics, **65**, 1613–1621.

Hadlow, R. E., 1992, Update of industry experience with CO_2 injection: 67th Ann. Tech. Conf., Soc. Petr. Eng., 743–752.

Han, D., Nur, A., and Morgan, D., 1986, Effects of porosity and clay content on wave velocities in sandstones: Geophysics, **51**, 2093–2107.

Hashin, Z., and Shtrikman, S., 1963, A variational approach to the elastic behavior of multiphase materials: J. Mech. Phys. Solids, **11**, 127–140.

Haugan, P. M., and Drange, H., 1992, Sequestration of CO_2 in the deep ocean by shallow injection: Nature, **357**, 318–320.

Holtz, M. H., K., N. P., and Finley, R. J., 2001, Reduction of greenhouse gas emissions through CO_2 EOR in Texas: Environ. Geosci., **8**, 187–199.

Hudson, J. A., and Heritage, J. R., 1981, The use of the Born approximation in seismic scattering problems: Geophys. J. R. Astr. Soc., **66**, 221–240.

Jack, I., 1998, Time-lapse seismic in reservoir management: Soc. Expl. Geophys.

Jenkins, S. D., Waite, M. W., and Bee, M. F., 1997, Time-lapse monitoring of the Duri steamflood: A pilot and case study: The Leading Edge, **16**, 1267–1273.

Johnston, D. H., McKenny, R. S., Verbeek, J., and Almond, J., 1998, Time-lapse seismic analysis of Fulmar field: The Leading Edge, **17**, 1420–1426.

Johnston, D. H., Sun, M., Gouveia, W. P., Lu, C. P., Walley, D. S., and Lye, Y. C., 2002, Time-lapse seismic analysis at Irong Barat: Malay basin: 72th Ann. Internat. Mtg., Soc. Expl. Geophys., Expanded Abstract, 1681–1683.

Kennedy, G. C., 1954, Pressure-volume-temperature relations in CO_2 at elevated temperatures and pressures: Am. J. Sci., pages 225–241.

King, M., and Datta-Gupta, A., 1998, Streamline simulations: A current perspective: In Situ, **22**, 91–140.

Kirchner, A., and Shapiro, S. A., 2001, Fast repeat-modelling of time-lapse seismograms: Geophys. Prospect., **49**, 557–569.

Kuster, G. T., and Toksöz, M. N., 1974, Velocity and attenuation of seismic waves in tow-phase media: Part I. theoretical formulations: Geophysics, **39**, 587–606.

Landrø, M., 2001, Discrimination between pressure and fluid saturation changes from time-lapse seismic data: Geophysics, **66**, 836–844.

——— 2002, Uncertainties in quantitative time-lapse seismic analysis: Geophys. Prospect., **50**, 527–538.

Lankston, R. W., 1998, Propagating uncertainty in fluid replacement modeling: A tool for time lapse seismic survey planning and amplitude variation with angle(AVA) analysis: 68th Ann. Internat. Mtg., Soc. Expl. Geophys., Expanded Abstract, 48–51.

Lumley, D., 1995, Seismic time lapse monitoring of subsurface fluid flow: Ph.D. thesis, Stanford Univ.

Lumley, D. E., Behrens, R. A., and Wang, Z., 1997, Assessing the technical risk of a 4-D seismic project: The Leading Edge, **16**, 1287–1291.

Lumley, D. E., and Behrens, R. A., 1998, Piratical issues of 4D seismic reservoir monitoring: What an engineer needs to know: SPE Reservoir Evaluation and Engineering, **1**, 528–538.

Lumley, D., Nunns, A., Delorme, G., Adeogba, A., and Bee, M., 1999, Meren field, Nigeria: A 4D seismic case study: 69th Ann. Internat. Mtg., Soc. Expl. Geophys., Expanded Abstract, 1628–1631.

Mavko, G., and Mukerji, T., 1995, Seismic pore space compressibility and Gassmann's relation: Geophysics, **60**, 1743–1749.

Mavko, G., Mukerji, T., and Dvorkin, J., 1998, The rock physics handbook: Cambridge University Press.

Miles, J. W., 1960, Scattering of elastic waves by small inhomogeneities: Geophysics, **25**, 642–648.

Mindlin, R. D., 1949, Compliance of elastic bodies in contact: J. Appl. Mech., **16**, 259–268.

Nelson, P., 1994, Permeability-porosity relationship in sedimentary rocks: The Log Analyst, **35**, 38–62.

Nur, A., and Simmons, G., 1969, The effect of saturation on velocity in low porosity rocks: Earth Plan. Sci. Letters, **7**, 183–193.

Nur, A., 1989, Four dimensional seismology and (true) direct detection of hydrocarbons: The petrophysical basis, g: The Leading Edge, **8**, 30–36.

Nur, A., Mavko, G., Dvorkin, J., and Gal, D., 1995, Critical porosity: The key to relating physical properties to porosity in rocks.: 65th Ann. Internat. Mtg., Soc. Expl. Geophys., Expanded Abstract, 878–881.

Reuss, A., 1929, Berechnung der fliessgrenzen von mischkristallen auf grund der plastizitätsbedingung für einkristalle: Zeitschrift für Angewandte Mathematik und Mechanik, **9**, 49–58.

Rickett, J. E., and Lumley, D., 2001, Cross-equalization data processing for time-lapse seismic reservoir monitoring: A case study from the Gulf of Mexico: Geophysics, **66**, 1015–1025.

Ross, C. P., 2000, Effective AVO crossplot modeling: A tutorial: Geophysics, **65**, 700–711.

Sengupta, M., and Mavko, G., 1999, Sensitivity analysis of seismic fluid detection: 69th Ann. Internat. Mtg., Soc. Expl. Geophys., Expanded Abstract, 180–183.

Shuey, R. T., 1985, A simplification of the Zoeppritz equations: Geophysics, **50**, 609–614.

Shyeh, J. J., Johnston, D. H., Eastwood, J. E., Khan, M., and Stanley, L. R., 1999, Interpretation and modeling of time-lapse seismic data:Lena field, Gulf of Mexico: SPE Annual Tech. Conf. and Exhibition, Soc. Petr. Eng., SPE 56731.

Smith, G. C., and Gidlow, P. M., 1987, Weighted stacking for rock property estimation and detection of gas: Geophys. Prospect., **35**, 993–1014.

Srivastava, R. M., 1992, Reservoir characterization with probability field simulation: SPE 67th Annual Technical Conf. and Exhibition, 927–938, SPE 24753.

——— 1994, An overview of stochastic methods for reservoir characterization, *in* Yarus, J. M., and Chambers, R. L., Eds., Stochastic modeling and geostatistics: Principles, methods, and case studies: AAPG, 3–16.

Straub, K. M., Flemings, P. B., Ashbaugh, J., Kaleta, N., and VanWie, M., 2000, Geology and drainage of the Teal South 4500' sand: ERCH 4D-4C forum, Houston Advanced Research Center.

Timur, A., 1968, An investigation of permeability, porosity, and residual water saturation relationship for sandstone reservoirs: The Log Analyst, **9**, 8–17.

Toksöz, M. N., Cheng, C. H., and Timur, A., 1976, Velocities of seismic waves in porous rocks: Geophysics, **41**, 621–645.

Tura, A., and Lumley, D. E., 1999, Estimating pressure and saturation changes from time-lapse AVO data: 69th Ann. Internat. Mtg., Soc. Expl. Geophys., Expanded Abstract, 1655–1658.

Vargaftik, N. B., 1975, Tables on the thermodynamic properties of liquids and gases: Hemisphere Pub. Co.

Vasco, D. W., Yoon, S., and Datt-Gupta, A., 1999, Integrating dynamic data into high-resolution reservoir models using streamline-based analytic sensitivity coefficients: SPE J., **4**, 389–399.

Walsh, J., 1965, The effect of cracks on the compressibility of rock: J. Geophys. Res., **70**, 381–389.

Wang, Z., Nur, A., and Batzle, M., 1986, The effect of temperature on the seismic wave velocities in rocks saturated with hydrocarbons: SPE Annual Tech. Conf. and Exhibition, Soc. Petr. Eng., SPE 15646.

Wang, Z., Hirsche, W. K., and Sedgwick, G., 1991, Seismic monitoring of water floods - a petrophysical study: Geophysics, **56**, 1614–1623.

Wang, Z., 1997, Feasibility of time-lapse seismic reservoir monitoring: The physical basis: The Leading Edge, **16**, 1327–1329.

Wang, Z., Cates, M., and Langan, R., 1998, Seismic monitoring of CO_2 flood in a carbonate reservoir: A rock physics study: Geophysics, **63**, 1604–1617.

Wood, A. W., 1955, A textbook of sound: The MacMillan Co.

Wu, R. S., and Aki, K., 1985, Scattering characteristics of elastic waves by an elastic heterogeneity: Geophysics, **50**, 585–595.

Yoon, S., 2000, Dynamic data integration into high resolution reservoir models using streamline-based inversion: Ph.D. thesis, Texas A&M Univ.

Yuh, S. H., and Gibson, Jr., R. L., 2002, Uncertainty analysis in time-lapse seismic modeling: 72nd Ann. Internat. Mtg., Soc. Expl. Geophys., Expanded Abstract, 1723–1726.

Yuh, S. H., Yoon, S., Gibson, Jr., R. L., and Datta-Gupta, A., 2000, 4D seismic feasibility study based on an integrated reservoir model: 32nd Ann. Offshore Tech. Conf., Offshore Tech. Conf., Proceedings, 673–678.

Zimmerman, R. W., 1991, Compressibility of sandstones: Elsevier Science Publ.

VITA

Sung H. Yuh received a B.S. degree in Geology, Korea University, Korea, in 1992, and an M.S. degree in Geophysics, Texas A&M University, in 1997. His permanant address is TotalFinaElf E&P USA, Inc. 800 Gessner, suite 700, Houston, TX 77024.